Jets, Vortices and Turbulence in Quasi-Geostrophic Magnetohydrodynamics

by

Jonathan Tessier

A thesis
presented to the University of Waterloo
in fulfillment of the
thesis requirement for the degree of
Master of Mathematics
in
Applied Mathematics

Waterloo, Ontario, Canada, 2022

Author's Declaration

I hereby declare that I am the sole author of this thesis. This is a true copy of the thesis, including any required final revisions, as accepted by my examiners.

I understand that my thesis may be made electronically available to the public.

Abstract

In this thesis, we model the dynamics of the solar tachocline and the Earth's molten core using a shallow, rapidly rotating, and electrically conducting fluid on an f-plane. We explore the effects of a strong uniform magnetic field with and without a weak free-surface in three different physical problems. We start with large coherent vortices to build an understanding of the local interactions between the field and vortical structures. Magnetic field lines are expelled from the vortex cores for weaker fields and vortices are disrupted for stronger ones, along with a generation of small scale features in the potential vorticity. Including a weak free-surface makes the flow more compact and inhibits the field-induced anisotropy. We then study freely-decaying turbulence using the shape of the energy spectra and the spectral energy fluxes. Kinetic energy is sent to smaller length scales while magnetic energy moves to larger scales for increasing field strength. In the mid to large wavenumbers, the downscale transfer of energy is due to the Lorentz force. Including a free-surface adds an additional downscale transfer at smaller wavenumbers, provided the field is weak enough. Finally, we study the linear stability and nonlinear evolution of an unstable Bickley jet. The field and free-surface are confirmed to be individually stabilizing to the jet and the combined effects show increased stability.

Acknowledgements

I would like to thank everyone who made this thesis possible. In particular, I would like to thank Prof. Francis Poulin along with Prof. Marek Stastna and Prof. Michael Waite for their outstanding guidance and mentorship throughout my academic career here at the University of Waterloo. I would further like to thank Prof. David Hughes from the University of Leeds (UK) for sharing his expertise with us and consolidating results and ideas with the established literature of MHD. A special thanks also goes to Dr. Jemma Shipton from the University of Exeter (UK) for her help and proficiency in numerical methods early on in this endeavour. Finally, I would like to thank my friends and family for their respective support and encouragement.

Dedication

This thesis is dedicated to my niece and goddaughter, Emilia. I hope that she grows up in this world knowing that we strived to better understand it, from the sun that lights up the sky to the Earth's molten core beneath our feet. We have in this thesis put a small dent in the vast complexity of magnetohydrodynamics and there are countless phenomena we have yet to explore. There is no doubt in my mind that future generations will keep this topic alive, as there is much left to do.

Table of Contents

List of Figures

List of Tables

Chapter 1

Introduction

The sun provides the main source of energy to our planet [18] and it is therefore essential to understand its dynamics to better forecast the Earth's climate. The enclosed research is first applicable to the study of the solar tachocline, a relatively thin region between the sun's radiative interior and outer convection zone [16]. This region contains very strong shear and is of interest to many astrophysicists for having a significant role in the study of the solar dynamo, where the dynamics of plasma acts to generate and maintain the sun's magnetic field [42]. The accurate modelling of the solar tachocline is thus essential to provide the lower boundary condition for the turbulence in the sun's outer shell, which drives the radiative wind we receive everyday.

The second application of the following analysis concerns the Earth's molten core. Our planet's magnetic field is owed to dynamo action in its (high-temperature) liquid-metal center [27, 28, 70]. A model similar to that of the tachocline can be made for the molten core to consist of deep heavy fluid beneath a shell of lighter fluid at the core–mantle boundary, referred to as "the ocean of the core" [10, 11]. The Earth's magnetic field is our only line of defense against the incoming solar wind and understanding its dynamics is equally important. Further, changes in the geomagnetic field can have significant repercussions on the world's economy and safety, for example to impede geophysical exploration and navigation, to influence modern communication systems, and disrupt electric power [45].

Using common models from Fluid Mechanics (such as those used in oceanography) and including a magnetic force in the equations, we can investigate and predict the motion of electrically conducting fluids such as plasmas (ionized fluids) and liquid metals. We call magnetohydrodynamics (MHD) the study of fluid motion interacting with a magnetic field, such as the two fluid systems mentioned above. In addition to astrophysical plasmas

[42] and geomagnetism [4], MHD applies to smaller length scales as well, such as confined plasmas in the study of thermonuclear fusion [85]. Restricting ourselves to large-scale nearly two-dimensional flows, the results of this thesis concern a planar geometry as a local approximation to the surface of a spherical shell modelling the solar tachocline and the ocean of the core.

In addition to an investigation of the two-dimensional magnetohydrodynamic equations (2D-MHD), we further add the effects of a slightly moving free-surface in parallel with magnetism. The Quasi-Geostrophic (QG) model, in which the effects of rotation and the horizontal change in pressure dominate the momentum equation, has been very useful in understanding large-scale oceanic and atmospheric flows [17, 78, 71, 95]. In particular, we consider a barotropic QG model for which the physical quantities are independent of depth. Its extension to include MHD, namely quasi-geostrophic magnetohydrodynamics (QG-MHD), allows the study of linear waves, various types of instabilities, and nearly two dimensional MHD turbulence with slight deviations in the free-surface. In practice, a purely two-dimensional flow and one described by barotropic QG can be described by the same evolution equation, provided we adjust the definition of the evolved quantity. The potential vorticity (PV) in QG contains the sum of contributions from the ambient and relative vorticity as well as the influence of a weak free-surface. Since our model considers a constant value for the Coriolis frequency (an f-plane), the ambient contribution vanishes and we are left with the relative vorticity along with the effects of small surface deformation.

In this thesis, we aim to answer two questions in the context of a QG-MHD model on an f-plane. First, how does the evolution of a shallow conducting fluid differ, for increasingly strong magnetic fields, with a free-surface compared to with a rigid lid? To answer this, we revisit Weiss' [99] classical vortex problems to build an understanding on how vortices interact with magnetic fields and the free-surface. We then extend this wisdom to a global picture of decaying MHD turbulence and study the distribution of energy to provide a comprehensive comparison. Second, we wish to understand how the stability of a Bickley jet [6] is affected by increasingly strong magnetic fields with and without a free-surface. This discussion includes linear stability theory, as well as various numerical simulations. These questions describe the transition from a hydrodynamic flow to one dominated by magnetic effects with the absence and inclusion of a weak free-surface under the QG approximation. In a simple model of electrically conducting flows, this research therefore promises a novel perspective in the study of the solar tachocline and the geomagnetic core and a consequent leap in our understanding of the resulting dynamics.

1.1 Literature Review

The first theory of dynamo action was proposed by Larmor and later elaborated by Cowling in the first third of the twentieth century [53, 19]. The combination of Maxwell's equations with the evolution of a fluid velocity and the consequent discovery of MHD waves (today called Alfvén waves) came later in 1942 with the work of Hannes Alfvén [1]. A subsequent paper suggested applications to solar physics in the study of sunspots in 1946 [2]. However, the nonlinear and coupled evolution of the magnetic field and velocity appeared in 1950 with the works of Elsasser [28, 29]. Since then, multiple limits and configurations of these equations have been considered, for example in the two-dimensional limit [48, 102], a shallow-water model [35, 20, 21] and in a rotating frame [92, 103]. The QG version of these equations [103] reduces the shallow system to two equations for the PV and the magnetic potential, while encoding the effects of rotation and of the free-surface in the definition of the PV. This is the version we consider in the following chapters. We now review relevant works in the field of MHD turbulence and instabilities to prepare ourselves for the results to come.

1.1.1 Vortices

Before diving in to the study of fully established turbulence, we shall begin by reviewing the dynamics of coherent structures that lead to turbulent flows, such as vortices. In two-dimensional hydrodynamics, the generation of larger scale flows is due to vortex merging, a process that is impeded by rotation. Smaller vortices combine to generate larger ones and the typical length scale of the flow, or the scale containing the most kinetic energy, increases with time. In the presence of rotation (in a β-plane for example) these collections of vortices can be described as nonlinear Rossby waves forming large scale zonal flows [77, 22].

The inclusion of magnetic effects can have drastic consequences on the dynamics. A flow in a weak uniform field can essentially be hydrodynamic until the perturbation field becomes significant. The resulting evolution displays dramatically different behaviours compared to a hydrodynamic one. These include for example the suppression of the zonal alignment in β-plane flows mentioned above [92], the suppression of large-scale eddy generation [39] and the inhibition of turbulent transport [14, 51, 38, 46, 47]. The interaction of vortices with large scale fields is not a new topic in the literature and we will discuss in this thesis two particular behaviours. The first is the expulsion of magnetic flux, where vortices expel magnetic field lines from their core which reconnect and push the remaining field lines from the core to the outside of the vortex [99]. The stretching of initially-uniform

magnetic field lines amplifies the field until the generated small scale field has a significant role in the evolution. The consequent dynamical regime is one where we can observe a second phenomenon for MHD vortices, namely the disruption of vortex structures, either in their strength or shape. [57].

1.1.2 Turbulence

While we can think of vortices as a local generation mechanism, a fully developed turbulent flow is often characterized by an inertial range spectrum, being the shape of the spectral energy as a function of the wavenumber in the range of scales over which dissipation is negligible. The literature on isotropic 2D-MHD turbulence argues that it behaves more closely to 3D hydrodynamic turbulence, where the energy is transferred from larger to smaller length scales (a forward energy cascade) [33, 74, 68, 9]. The anticipated shape of the total energy spectrum follows a power law, $\hat{E}(k) \sim k^{-3/2}$ in the inertial range, following a modification of Komolgorov's argument by Iroshnikov (1963) [44] and Kraichnan (1965) [48]. This behaviour differs quite strongly from that of 2D hydrodynamics which results in a forward enstrophy (total squared vorticity) cascade, where the associated energy spectrum has shape $\hat{E}(k) \sim k^{-3}$ [5, 49]. However, 3D-MHD isotropic turbulence does not follow the Iroshnikov-Kraichnan phenomenology and the energy spectrum follows a $k^{-5/3}$ law, clearly steeper than $k^{-3/2}$ in 2D-MHD [7, 66].

The inclusion of a uniform background magnetic field in 2D-MHD (in the same plane as the fluid) induces anisotropy in an initially isotropic spectrum [83]. The dynamics transfer energy to the wavenumbers perpendicular to the field which results in a flow tending to align with it. It was confirmed that the same anisotropy develops in 3D-MHD [69, 60]. Matthaeus et al. (2008) [58] also found in the same regime that the magnetic field and gradients of kinetic energy tend to align (reminiscent of a similar alignment in hydrodynamic turbulence for velocity and vorticity).

Hydrodynamic turbulence on an f-plane with a free-surface has been discussed in detail [72, 52, 98, 50, 75] along with a 2-layer extension [79, 80]. It was shown that the presence of a free-surface inhibits energy from moving to scales larger than the Rossby deformation radius, R_d. The interaction between vortices at large scales is inhibited, and the dynamics become more compact in space. At scales smaller than R_d, the dynamics are those of 2D turbulence where vortices combine and grow to reach R_d in scale. The consequent inclusion of magnetism has been applied to the study the ocean of the core on a β-plane [4]. The energy was found to cascade to smaller length scales with significant anisotropy in the energy spectrum. More intricate models, compared to the one we investigate in

4

this thesis, have been used to model flow in the Earth's core [13, 12, 100]. Recent results however suggest that the core is dominated by QG motion, followed by a balance between the ageostrophic Lorentz, buoyancy and Coriolis forces [3, 82].

1.1.3   Instabilities

Much can be said about turbulence and its respective limits, but it is often difficult to analytically quantify the dynamics of such regimes. Hydrodynamic and MHD instabilities allow us to study simple flows in detail without the chaos and randomness intrinsic to turbulence. They present a different perspective to study physical mechanisms present in turbulence, such as the anisotropy generated by a uniform magnetic field in Faraday instabilities [89]. It is worth noting that magnetic fields are known to invalidate or change many significant hydrodynamic results on the stability of shear flows. For example, the Miles-Howard theorem [62, 40] does not apply in MHD, where stratified shear flows can be unstable with a Richardson number larger than $1/4$ [54]. Further, shear instabilities can still exist in the absence of an inflection point in the background flow [88], as opposed to the hydrodynamic case where it is necessary [76]. Squire's Theorem [84] doesn't always hold in non-ideal MHD shear flows, where the 3D perturbation can be more unstable than the 2D analogue [43, 41]. Finally, Howards' semicircle theorem [40] is modified in the presence of a magnetic field. The eigenvalues (and so the growth rates and phase speeds of the modes) of the relevant linear stability problem are bounded in the complex plane by a region dependent on the strength and profile of the flow and magnetic field [41].

The instabilities discussed in this thesis concern barotropic parallel shear flows and we focus on a Bickley jet to better understand the influence of magnetism and weak free-surface on its evolution. For a more complete reference on hydrodynamic stability, see Drazin and Reid 2004 [24] and for hydromagnetic stability, see Chandrasekhar 1961 [15]. Barotropic jets have already been studied in the hydrodynamic regime extensively. For example, Poulin & Flierl 2003 [73] studied a shallow-water Bickley jet in both QG and non-QG parameter regimes and showed that the flow was stabilized by increasing a rotational Froude number (what we call F in this thesis) and Rossby number. Jets are also well-known structures in the magnetic context. Magnetic fields are found to have a stabilizing effect on jets and shear flows [41, 56, 31]. Even non-uniform magnetic fields such as hyperbolic tangent profiles have stabilising effects [8]. Stratification, as measured by the Froude number (not equal to the rotational Froude number mentioned above), also stabilises the flow in magnetic regimes but weak instabilities can be found at arbitrarily large Froude number [56]. In a recent submission, Fraser et al. 2022 [31] investigated the linear stability of a shear flow with a sinusoidal velocity profile in a parallel uniform magnetic field with

finite kinetic and magnetic Reynolds numbers. While this flow is known to be unstable to the Kelvin-Helmholtz instability in the hydrodynamic regime, it is also the case in ideal MHD, where dissipation is neglected, provided that the magnetic field strength is small enough. The authors found however that including viscosity and resistivity introduces two new modes of instability, one of which is reminiscent of Alfvén waves and exists for any magnetic regime provided the Prandtl number $Pm < 1$.

1.2   Overview

The following chapters are separated as follows. In Chapter 2, we present the physical parameters and dimensional equations of QG-MHD [103] along with their nondimensionalization. Conserved quantities for these equations are derived along with their respective decay laws in the case of finite viscosity and magnetic diffusion. Then, we present a novel contribution to the literature by deriving the spectral energy budgets of these equations which are numerically investigated in later chapters. We then include the derivation of the linear stability problem for a shear flow in a parallel magnetic field both only dependent on the cross-stream variable. Finally, the second chapter is closed by an overview of the code. The next three chapters concern the numerical study of three physical scenarios, namely MHD vortices, decaying turbulence and unstable Bickley jets. We use three different configurations of the code, one for each chapter, to focus on the relevant dynamics. Chapter 3 shows the evolution of various collections of MHD vortices in a rigid lid, and then with the addition of the free-surface. Hydrodynamic limits are also discussed. The purpose of this chapter lies in establishing a foundation for the physical mechanisms at play and expanding on the work of Weiss on flux expulsion. Chapter 4 moves to a global description of freely decaying MHD turbulence (in the sense that it is unforced in time at any scale and the initial random fields are let to evolve on their own). The rigid lid and free-surface cases are compared for various strengths of the magnetic field and the numerical investigation of the spectral energy budget is presented. Chapter 5 marks the final chapter of results by focusing on the instability of the Bickley jet. The linear stability problem is solved for various sets of parameters and the nonlinear evolution of the jet is presented to confirm the combined influence of magnetism and a free-surface on its stability. Finally, we conclude in Chapter 6 with a summary of the results and future research directions.

Chapter 2

Methods

In this chapter we include a discussion of the physical parameters, the nondimensional-ization of the QG-MHD equations and the computation of the model invariants, namely the energy, the cross-helicity and the mean-square magnetic potential. We also include the derivation of the spectral energy budgets (hydrodynamic and magnetic) which we have not found in the literature for these equations. This computation leads to a local form of the the spectral energy fluxes which allows us to isolate and quantify the physical mechanisms pushing energy to smaller or larger scales. Further, we include the linear stability analysis of a shear flow aligned with a magnetic field. Finally, we outline the inner workings of the code authored by Prof. Francis Poulin and myself.

2.1 Physical Parameters

Before diving into the model equations, we present a summary of the physical parame-ters and their respective investigated regimes. Our model allows the variability of four dimensionless parameters. They read,

$$M = \frac{V_A}{U}, \quad F = \frac{L}{R_d} = \frac{Lf}{C_g}, \quad R_e = \frac{UL}{\nu} \quad R_m = \frac{UL}{\kappa} \tag{2.1}$$

and correspond to the ratio of the Alfvén wave speed to the typical system velocity (effective magnetic field strength), a rotational Froude number (or an inverse Burger number) and the kinetic and magnetic Reynolds numbers. See Table 2.1 for the definitions of all dimensional parameters including the relevant velocities. There are two other nondimensional quantities

that are relevant but do not appear in our equations. The aspect ratio $H/L \ll 1$ is assumed to very small in our use of the barotropic approximation on the flow, where nothing depends on depth. The QG approximation further requires a small Rossby number $Ro = U/fL \ll 1$ and small surface perturbations compared to the layer depth, H.

Parameter	Definition
L	Horizontal length scale of motion (m)
H	Vertical length scale of motion (m)
U	Horizontal system velocity scale ($\mathrm{m\,s^{-1}}$)
B	Horizontal magnetic field scale ($\mathrm{G} = 10^{-4}\,\mathrm{kg\,A^{-1}\,s^{-2}}$)
f	Coriolis frequency ($\mathrm{s^{-1}}$)
g	gravity ($\mathrm{m\,s^{-2}}$)
ρ	density ($\mathrm{kg\,m^{-3}}$)
μ	magnetic permeability ($\mathrm{m\,kg\,s^{-2}\,A^{-2}}$)
ν	kinematic viscosity ($\mathrm{m^2\,s^{-1}}$)
κ	magnetic diffusivity ($\mathrm{m^2\,s^{-1}}$)
$V_A = B/\sqrt{\mu\rho}$	Alfvén wave speed ($\mathrm{m\,s^{-1}}$)
$C_g = \sqrt{gH}$	gravity wave speed ($\mathrm{m\,s^{-1}}$)
$R_d = C_g/f$	External Rossby radius of deformation (m)

Table 2.1: List of physical parameters and their definition

In the Earth's liquid core, estimates of the relevant parameters are discussed for example in Balk 2014 [4]. The approximate layer depth is taken as $H \approx 50$ km, with a reduced gravity of $g \approx 10^{-3}$ $\mathrm{ms^{-2}}$ providing a gravity wave speed of $C_g \approx 7$ $\mathrm{ms^{-1}}$. At 30° latitude, $f \approx 7 \times 10^{-5}$ $\mathrm{s^{-1}}$ and the Alfvén wave speed is given by $V_A \approx 0.3$ $\mathrm{ms^{-1}}$. On horizontal length scales of 400 km and flows of $U = 1$ $\mathrm{ms^{-1}}$ then, we find $M \approx 0.3$, $F \approx 4$, $Ro \approx 0.03$. Thus, small Rossby numbers are achievable and the dominance of geostrophic balance for the liquid core is further discussed in Braginsky 1998 [10]. These scales also give a small aspect ratio of $H/L \approx 0.125$ justifying our use of the shallow approximation. A kinematic viscosity of $\nu = 5 \times 10^{-7}$ $\mathrm{m^2s^{-1}}$ and a magnetic diffusivity of $\kappa = 2$ $\mathrm{m^2s^{-1}}$ [11] both provide large Reynolds numbers on the considered scales, $R_e \approx 8 \times 10^{11}$, $R_m \approx 6 \times 10^4$.

The dynamics of the tachocline are those of a stably-stratified shear flow where large scale motions are nearly two-dimensional and slow enough that the Coriolis force has a significant role in the evolution [42]. Tobias et al. [92] estimated a broad range of Rossby numbers at the base of the tachocline to span between 0.1 and 1, though geostrophic balance has been mentioned to be marginal on the sun [34]. Reynolds numbers are very large in the tachocline, where $R_m \approx 10^5 - 10^6$ while R_e is even larger, providing a small

Prandtl number $Pr = R_m/R_e < 1$ [37, 92]. Mak et al. 2016 [56] estimated some relevant parameters for the tachocline based on data from Gough 2007 [37]. They consider a likely range for the Alfvén wave speed of 6 to 600 ms^{-1}. They further take a typical global scale velocity U of 200 ms^{-1} while mentioning a reasonable local scale velocity of 20 ms^{-1}. This range translates to M values between 0.03 and 3 for the global velocity scale and between 0.3 and 30 locally. The global and local scales of the velocity together confirm the range of Rossby numbers mentioned above on horizontal length scales of 50,000 km (approximately 10% of the tachocline radius).

The tachocline is separated into two regions, including a lower radiative and upper overshoot layer. Though the field strength is generally taken as being the same, the gravity wave speed differs in each region. Following the estimates of [81] the radiative layer has a depth of 5000 km and an associated gravity wave speed ranging from $7 \times 10^3 - 4 \times 10^4$ ms^{-1}, much larger than the Alfvén wave speed. The Coriolis frequency at 30° latitude in the tachocline is $f \approx 3 \times 10^{-6}$ s^{-1}. At horizontal length scales of 50,000 km, the corresponding value of F ranges from 3×10^{-3} to 2×10^{-2}. The overshoot layer however is half as thick as the radiative layer, with gravity wave speed of 50 to 500 ms^{-1}. There, F ranges from about 0.3 to 3. In the lower tachocline, we have a small aspect ratio of $H/L \approx 0.1$ and an even smaller one in the overshoot layer with $H/L \approx 0.05$, justifying the shallow approximation again in either case.

Physical Region	M	F	Ro	H/L
Solar Tachocline (combined)	0.03 - 30	0.003 - 3	0.1 - 1	0.05 - 0.1
Earth's Ocean of the Core	0.3	4	0.03	0.125

Table 2.2: Estimation of the nondimensional parameters for the Solar Tachocline (combining the ranges from both the upper and lower regions) and for the Earth's ocean of the core.

Table 2.2 summarizes the estimates of the nondimensional parameters mentioned above. In our simulations, we keep a constant Prandtl number $Pr = R_m/R_e = 1$, with $R_e = R_m = 10^4$, since considering $Pr \neq 1$ already introduces a large disparity between the kinetic/magnetic dissipated scales [91, 26]. In our computation of the viscous and diffusive energy fluxes, we want to compare the dissipated scales associated with the velocity and magnetic field, purely differing in their intrinsic dynamics and not on the weight of their respective Laplacians. We further consider slightly smaller Reynolds numbers in order to keep a large enough amplitude of physical dissipation in the same analysis. We consider four points in the relative strength of the magnetic field compared to the typical velocity of the flow, $M \in \{0, 10^{-3}, 10^{-2}, 10^{-1}\}$. These correspond to a hydrodynamic evolution,

a very weak magnetic field displaying the onset of magnetic effects, a moderate magnetic field where significant vortex disruption occurs and finally a strong field well within the range applicable to the the tachocline and similar to the Earth's core. These values are chosen to explore the impact of the magnetic field with various strengths on the dynamics. Along with above values of M, we consider the rotational Froude number F to be between 0 and 1, where $F = 0$ considers an infinite external Rossby radius of deformation $R_d \to \infty$ (equivalently, 2D-MHD applicable to the lower tachocline) and where $F = 1$ corresponds to a flow with typical length scale equal to R_d (a free-surface with small deformations and rotational influence) better applicable to the upper tachocline and the Earth's ocean of the core.

2.2 Governing Equations

The model equations in dimensional form, as derived in Zeitlin (2013) [103], are those of barotropic QG-MHD. They describe the evolution of the PV, q and the evolution of a magnetic streamfunction, A. To derive the model equations, one can start with the Navier Stokes equations (with a Lorentz force and a Coriolis force) and the continuity equation. For a dynamic magnetic field, there are two additional equations, one to evolve the magnetic field (induction equation) and one to ensure that it is divergence-free (Gauss' law for magnetism). To obtain the shallow version of the model, as seen in Gilman 2000 [35], assume a constant density, a small aspect ratio, and vertically integrate the equations such that nothing depends on depth. From these to QG-MHD, assume that the Coriolis force and the horizontal pressure gradient dominate the momentum equation (small Rossby number) and that surface deformations are very small. The velocity and magnetic field are both two-dimensional and divergence-free such that we can define a stream-function in each case. The PV equation comes readily from the curl of the momentum equation and the evolution of the field to be rewritten as an advection-diffusion problem for A. Neglecting diffusion of the background quantities (similar to [31]), the equations in dimensional form

read,

$$\partial_t q + \mathbf{u} \cdot \nabla q = \frac{1}{\mu\rho} \mathbf{b} \cdot \nabla j + \nu\nabla^2(q - \bar{q})$$

$$\partial_t A + \mathbf{u} \cdot \nabla A = \kappa\nabla^2(A - \bar{A}),$$

$$q = \nabla^2\psi - \frac{1}{R_d^2}\psi, \qquad\qquad (2.2)$$

$$j = \nabla^2 A,$$

$$\mathbf{u} = \nabla^{\perp}\psi = \hat{z} \times \nabla\psi,$$

$$\mathbf{b} = \nabla^{\perp}A = \hat{z} \times \nabla A.$$

Then, $\psi, A, q, j, \mathbf{u}$, and $\mathbf{b}$ are the kinetic and magnetic streamfunctions, potential vorticty (PV), current, 2D velocity and 2D magnetic field, respectively. Recall Table 2.1 for a summary of the dimensional parameters. The geostrophic streamfunction ψ is proportional to the (small amplitude) free-surface deformation η, where $\psi = \frac{g}{f}\eta$ [61]. In the limit of infinite R_d, the system (2.2) reduces to standard 2D-MHD [103].

2.3 Nondimensionalizing the Equations

To reduce the number of variables we can change to alter the flow, we nondimensionalize system (2.2) and pick the following scales to do so:

$$\mathbf{u}^* = U\,\mathbf{u},$$

$$\mathbf{x}^* = L\,\mathbf{x},$$

$$t^* = \frac{L}{U}t \qquad\qquad (2.3)$$

$$\psi^* = LU\,\psi$$

$$A^* = LV_A\,A$$

$$\mathbf{b}^* = V_A\,\mathbf{b}.$$

We absorb the factor of $1/\sqrt{\mu\rho}$ into the magnetic field $\mathbf{b}$, such that it has units of velocity and the free-surface η is scaled by the mean depth H. We pick an advective time scale, as is typically done in QG models. Then, U, L and V_A are the scales of velocity, horizontal

11

length scale and magnetic field. Applying the above to system (2.2), we get the following:

$$\partial_t q + \mathbf{u} \cdot \nabla q = M^2 \mathbf{b} \cdot \nabla j + \frac{1}{R_e} \nabla^2 (q - \bar{q}),$$

$$\partial_t A + \mathbf{u} \cdot \nabla A = \frac{1}{R_m} \nabla^2 (A - \bar{A}),$$

$$\mathbf{u} = \hat{z} \times \nabla \psi, \tag{2.4}$$

$$\mathbf{b} = \hat{z} \times \nabla A,$$

$$q = \nabla^2 \psi - F^2 \psi,$$

$$j = \nabla^2 A,$$

where we have the dimensionless parameters F (a rotational Froude number or an inverse Burger number) and M (the ratio of the Alfvén wave speed to the typical system velocity), and the kinetic and magnetic Reynolds numbers defined in (2.1). Flows with finite R_m are also referred to as magnetically resistive flows (e.g. [31]). When the induction equation is allowed to diffuse as it is in this thesis, the magnetic field is allowed to partially decouple from the fluid particles compared to its frozen-in property in ideal MHD. The above system (2.4) is the one we investigate in various limits such as the hydrodynamic case, where $M = 0$, and the case of a rigid lid, when $F = 0$. Of course, exploration is done on non-zero values for these system parameters. The nondimensional relationship between the geostrophic streamfunction ψ and the free-surface deformation η now reads $\eta = \frac{U}{C_g} F \psi$. It clearly follows that when $F = 0$, the free-surface deformation is zero regardless of ψ.

2.4   Conserved quantities

After stating the model, we investigate its conserved quantities to better understand the dynamics. In order to discuss and compute these quantities, the system (2.4) can be written more conveniently as,

$$\partial_t q + J(\psi, q) - M^2 J(A, j) = \frac{1}{R_e} \nabla^2 (q - \bar{q}), \tag{2.5}$$

$$\partial_t A + J(\psi, A) = \frac{1}{R_m} \nabla^2 (A - \bar{A}), \tag{2.6}$$

where we denote the Jacobian $J(A, B)$, for two quantities A and B, as

$$J(A, B) = \partial_x A \, \partial_y B - \partial_y A \, \partial_x B. \tag{2.7}$$

We will ignore diffusion of the background fields in the present analysis of conserved quantities. For all cases considered in this thesis, the background magnetic streamfunction is a linear function of the y-coordinate (for a constant uniform field) and so its Laplacian is identically zero. The background PV is also zero, with the exception of our investigation on the Bickley jet. In a β-plane geometry, the PV in the Jacobian term of (2.5) would replaced by $q + \beta y$. In the conservative limit, $(R_e, R_m \to \infty)$ the above system has three conserved quantities,

$$E = \frac{1}{2} \iint_D (|\mathbf{u}|^2 + |M\mathbf{b}|^2 + F^2\psi^2)\, dxdy, \tag{2.8}$$

$$H = \iint_D M(\mathbf{u} \cdot \mathbf{b} + F^2 A\psi)\, dxdy, \tag{2.9}$$

$$\Phi = \iint_D \frac{1}{2}(MA)^2\, dxdy, \tag{2.10}$$

namely the total energy, the cross-helicity (adjusted for non-zero F) and the mean-square magnetic potential for a domain, D. Conversely, in the presence of viscosity and magnetic diffusion, we would like to know how these quantities decay in time. Theory predicts that in the limit of $F = 0$ and $M = 1$ the energy and cross-helicity show a direct cascade, while $\hat{\Phi}(k)$ shows an inverse cascade [33, 74, 68]. Note that enstrophy is not conserved in the magnetic regime $M \neq 0$.

2.4.1 Energy

To find an evolution equation for the energy of the system, multiply (2.5) by $-\psi$, add it to (2.6) multiplied by $-M^2\nabla^2 A = -M^2 j$ and integrate over the entire domain. The result reads

$$\iint_D -\psi\partial_t(\nabla^2\psi - F^2\psi) - \psi J(\psi, q) + M^2\psi J(A, \nabla^2 A)\, dxdy$$
$$+ \iint_D -M^2\nabla^2 A\partial_t A - M^2\nabla^2 A J(\psi, A)\, dxdy = \iint_D -\frac{\psi}{R_e}\nabla^2 q - \frac{M^2}{R_m}j^2\, dxdy. \tag{2.11}$$

13

We can integrate by parts[1] on the first terms of each integral on the LHS of (2.11) and commute the time derivatives with the Laplacians to find

$$\iint_D \left(\psi\,\nabla^2\partial_t\psi + \nabla\psi\cdot\partial_t\nabla\psi\right)dxdy = \oint_{\partial D}\psi\left(\partial_t\nabla\psi\cdot\mathbf{n}\right)dS, \qquad (2.12)$$

$$\iint_D \left(\partial_t A\,\nabla^2 A + \nabla A\cdot\partial_t\nabla A\right)dxdy = \oint_{\partial D}\partial_t A\left(\nabla A\cdot\mathbf{n}\right)dS. \qquad (2.13)$$

The boundary terms above read (in general, for $\psi = \overline{\psi} + \psi'$, $A = \overline{A} + A'$, where barred quantities are stationary and primed quantities are perturbations)

$$\oint_{\partial D}\psi\left(\partial_t\nabla\psi\cdot\mathbf{n}\right)dS = \oint_{\partial D}\overline{\psi}\left(\partial_t\nabla\psi'\cdot\mathbf{n}\right)dS + \oint_{\partial D}\psi'\left(\partial_t\nabla\psi'\cdot\mathbf{n}\right)dS = 0, \qquad (2.14)$$

$$\oint_{\partial D}\partial_t A\left(\nabla A\cdot\mathbf{n}\right)dS = \oint_{\partial D}\partial_t A'\left(\nabla\overline{A}\cdot\mathbf{n}\right)dS + \oint_{\partial D}\partial_t A'\left(\nabla A'\cdot\mathbf{n}\right)dS = 0. \qquad (2.15)$$

The perturbations in the streamfunctions are assumed to be doubly periodic and so the last contour integrals of (2.14) and (2.15) vanish. In our analysis, $\overline{\psi} = 0$ and $\nabla\overline{A} = (0,-1)$ are constant such that the other two contour integrals vanish. Then, using (2.12) to (2.15), and a the chain rule on the time-derivatives, we can rewrite (2.11) as

$$\iint_D \frac{1}{2}\partial_t(\nabla\psi\cdot\nabla\psi + F^2\psi^2 + M^2\nabla A\cdot\nabla A)\,dxdy - \frac{1}{2}\iint_D J(\psi^2,q)\,dxdy$$
$$+ \iint_D M^2\psi J(A,j) - M^2 j J(\psi,A)\,dxdy = -\iint_D \frac{\psi}{R_e}\nabla^2 q + \frac{M^2}{R_m}j^2\,dxdy. \qquad (2.16)$$

Given our considered periodicity, it can also be shown that (see Swaters 1999 [87])

$$\iint_D J(\psi^2,q)\,dxdy = \iint_D \nabla\cdot\left(q\hat{z}\times\nabla(\psi^2)\right)dxdy = \oint_{\partial D}q\hat{z}\times\nabla(\psi^2)\cdot\hat{n}\,dS = 0. \qquad (2.17)$$

Further, the following holds for three quantities A,B,C (see Swaters 1999 [87]),

$$\iint_D A J(B,C) - C J(A,B)\,dxdy = 0, \qquad (2.18)$$

and so the Jacobian terms in (2.16) involving the magnetic streamfunction vanish,

$$\iint_D \psi J(A,\nabla^2 A) - \nabla^2 A J(\psi,A)\,dxdy = 0. \qquad (2.19)$$

---

[1]Equivalently, use Green's first identity.

Physically, the cancellation of these terms shows that the change in the total energy from the Lorentz force is compensated by the advection of the magnetic potential. Finally, to find a positive definite form of the integrand in the viscous term of (2.16), notice that we can integrate by parts to transfer the Laplacian from q onto the streamfunction, where q and ψ are periodic in the x-direction and have zero Neumman boundary conditions at the top and bottom,

$$-\frac{1}{R_e}\iint_D \psi\nabla^2 q\,dxdy = -\frac{1}{R_e}\iint_D q\nabla^2\psi\,dxdy = -\frac{1}{R_e}\iint_D (\nabla^2\psi)^2 - F^2\psi\nabla^2\psi\,dxdy. \tag{2.20}$$

Similarly, integrate by parts on the last RHS term of (2.20) to make the integrand positive

$$-\frac{1}{R_e}\iint_D \psi\nabla^2 q\,dxdy = -\frac{1}{R_e}\iint_D (\nabla^2\psi)^2 + F^2(\nabla\psi)^2\,dxdy. \tag{2.21}$$

Therefore, in the absence of magnetic diffusion and viscosity, energy is conserved

$$\frac{d}{dt}E = \frac{d}{dt}\frac{1}{2}\iint_D \nabla\psi\cdot\nabla\psi + F^2\psi^2 + M^2\nabla A\cdot\nabla A\,dxdy = 0, \tag{2.22}$$

and its density is the integrand, consisting of a kinetic, a potential, and a magnetic part. This density can be rewritten in a few ways,

$$dE = \frac{1}{2}\left(\nabla\psi\cdot\nabla\psi + F^2\psi^2 + M^2\nabla A\cdot\nabla A\right) \tag{2.23}$$

$$= \frac{1}{2}\left(|\mathbf{u}|^2 + F^2\psi^2 + |M\mathbf{b}|^2\right) \tag{2.24}$$

$$= \frac{1}{2}\left(\psi q + M^2 Aj\right), \tag{2.25}$$

consistent with the definition of the associated Hamiltonian from Zeitlin (1992) [102] or Zeitlin and Kambe (1993) [104]. Conversely, for finite Reynolds numbers, we have found the decay law

$$\frac{d}{dt}E = -\iint_D \frac{1}{R_e}\left((\nabla^2\psi)^2 + F^2(\nabla\psi)^2\right) + \frac{M^2}{R_m}j^2 dxdy, \tag{2.26}$$

which is consistent with the energy decay noted in [9] when $F = 0$ and $M = 1$. This statement concerns the total system energy with magnetism and a weak free-surface. In the purely hydrodynamic case, $M = 0$ and so the last term in the integral of (2.26)

vanishes. If F is also zero, the total energy is the kinetic energy which decays with $-\iint_D \frac{1}{R_e}(\nabla^2\psi)^2\,dxdy$. Inspired by the work of Weiss, we discuss the case of pure induction, where the velocity is fixed and where the induced changes in the magnetic field have no effect back onto the motion. This amounts to only evolving the equation for the magnetic streamfunction A (2.6), and setting the evolution of q (2.5) to zero. Much of our previous computations hold, except for the inclusion of the Lorentz force term which now has to vanish if the velocity is held fixed in time and the field is not. This prevents us from using (2.19) and so we have an extra term on the RHS of the energy equation, $+M^2 \iint_D jJ(\psi, A)\,dxdy$. This term can add energy to the system when $jJ(\psi, A) > 0$ and can be rewritten as $+M^2 \iint_D j\mathbf{u} \times \mathbf{b}\,dxdy$. Of course, there is still magnetic diffusion in the induction case but the kinetic energy is held constant. Evolving A alone in an inviscid advection equation clearly conserves A, but we are concerned with the total system energy. The decay law of energy in the case of pure induction then reads

$$\frac{d}{dt}E = \iint_D M^2 jJ(\psi, A) - \frac{M^2}{R_m}j^2\,dxdy = M^2 \iint_D j\mathbf{u} \times \mathbf{b} - \frac{1}{R_m}j^2\,dxdy, \qquad (2.27)$$

where we have re-written the first term as a function of the velocity and magnetic field to showcase that this term vanishes if $\mathbf{u}$ and $\mathbf{b}$ are parallel (or anti-parallel). Thus, energy can be conserved in pure induction if the field and the velocity are aligned.

2.4.2 Cross-helicity

We now move on to the second conserved quantity, the cross-helicity, H. This quantity measures the correlation or alignment between the velocity and the magnetic field. Cross-helicity is also found to contribute to the Lorentz force, where the resulting field-generation is referred to as the cross-helicity dynamo [101]. The characteristic features of this dynamo include the alignment of the mean current density with the mean vorticity. Recall equations (2.5) and (2.6). Multiply the first equation by $-MA$ and the second by $-Mq$. Add and integrate over the entire domain to find,

$$\iint_D - MA\partial_t q - MAJ(\psi, q) + M^3 AJ(A, \nabla^2 A)\,dxdy$$
$$+ \iint_D -Mq\partial_t A - MqJ(\psi, A)\,dxdy = \iint_D -\frac{MA}{R_e}\nabla^2 q - \frac{M}{R_m}jq\,dxdy. \qquad (2.28)$$

Using the same approach we used for the energy, it is straight-forward to notice that the $-MqJ(\psi, A)$ and $-MAJ(\psi, q)$ terms cancel via (2.18). Similarly, the $M^3 AJ(A, \nabla^2 A)$ term

integrates to zero as did (2.17). Then, we are left with,

$$- \iint_D MA\partial_t q + q\partial_t MA \, dxdy = - \iint_D \frac{MA}{R_e}\nabla^2 q + \frac{M}{R_m}jq \, dxdy. \qquad (2.29)$$

Using $q = \nabla^2\psi - F^2\psi$, integrate by parts on the terms of (2.29) with time derivatives and the viscous/diffusive terms[2]. This yields

$$\iint_D \partial_t(M\nabla A \cdot \nabla\psi) + F^2 M\partial_t(A\psi) \, dxdy = -(\frac{1}{R_e} + \frac{1}{R_m}) \iint_D Mjq \, dxdy. \qquad (2.30)$$

Re-writting for the velocity and magnetic field, and including our definition of cross-helicity,

$$\frac{d}{dt}H = \frac{d}{dt} \iint_D M(\mathbf{u} \cdot \mathbf{b} + F^2 A\psi) \, dxdy = -(\frac{1}{R_e} + \frac{1}{R_m}) \iint_D Mjq \, dxdy. \qquad (2.31)$$

When $F = 0$, this is equivalent to what arises in the 2D-MHD model [9]. However, our more general model includes an extra term due to the free-surface $F^2\frac{d}{dt}\iint_D MA\psi \, dxdy$. This suggests an adjusted definition of H in barotropic QG-MHD compared to 2D-MHD. This form is rather unsurprising because the QG-MHD equations conserve integrated functions of the magnetic potential ($f(A)$), and integrated functions of magnetic potential multiplied by the QG PV ($qf(A)$) [103]. Returning to our equation (2.29), where the integrand in the RHS is simply the time derivative of the product $-MAq$, we can show that [3]

$$\frac{d}{dt} \iint_D -MAq \, dxdy = \frac{d}{dt} \iint_D M(\mathbf{u} \cdot \mathbf{b} + F^2 A\psi) \, dxdy = \frac{d}{dt}H. \qquad (2.32)$$

2.4.3 Mean square magnetic potential

The last invariant is rather simple and concerns the integrated square of the magnetic potential. This quantity in a sense replaces the conservation of PV from hydrodynamics which is prevented in this context due to the Lorentz force. Multiply (2.6) by $M^2 A$ and integrate over the entire domain to find,

$$\iint_D M^2 A\partial_t A + M^2 AJ(\psi, A) \, dxdy = \iint_D \frac{1}{R_m}M^2 Aj \, dxdy, \qquad (2.33)$$

---

[2]Again, equivalently use Green's first and second identities

[3]Similarly, the form of cross-helicity in the shallow MHD equations [35] as investigated in [21], reads $H_{SMHD} = - \iint_D hqA \, dxdy = \iint_D h\mathbf{u} \cdot \mathbf{b} \, dxdy$ which is dependent on the layer depth, h.

which we can rewrite as,

$$\iint_D \frac{1}{2}\partial_t(MA)^2 + M^2 J(\psi, \frac{1}{2}A^2) \, dxdy = -\frac{1}{R_m}\iint_D (M\nabla A)^2 \, dxdy. \qquad (2.34)$$

Our velocity is divergence free to leading order and so (with the divergence theorem and zero net flux)

$$\iint_D J(\psi, \frac{1}{2}A^2 \, dxdy = \iint_D \mathbf{u}\cdot\nabla(\frac{1}{2}A^2) \, dxdy = \iint_D \nabla\cdot\frac{1}{2}(\mathbf{u}A^2) \, dxdy = 0. \qquad (2.35)$$

Thus,

$$\frac{d}{dt}\Phi = \frac{d}{dt}\iint_D \frac{1}{2}(MA)^2 \, dxdy = -\frac{1}{R_m}\iint_D (M\nabla A)^2 \, dxdy \qquad (2.36)$$

which is again consistent with 2D-MHD [9] and independent of the free-surface.

2.5   Spectral Energy Fluxes

From our review of the literature on 2D-MHD turbulence, we have not yet seen the computation of spectral energy fluxes in the global sense. Pouquet et al. 1978 [74] investigated this topic restricted to triad interactions (how three particular waves interact) and Diamond et al. 2007 [23] focused on the spectral transfers of the mean square magnetic potential in β-plane turbulence. We include in this discussion the derivation of the spectral energy budgets along with their respective fluxes in terms of bulk physical quantities. Our goal with this computation is to better understand the physical mechanisms moving energy to different length scales. We frame this discussion in the context of decaying turbulence for a uniform background field (Chapter 4) and so the kinetic (KE), potential (PE) and magnetic energy (ME) can be written as

$$E_V = \frac{1}{2}\iint_D |\mathbf{u}|^2 dxdy, \qquad (2.37)$$

$$E_P = \frac{1}{2}\iint_D F^2\psi^2 dxdy, \qquad (2.38)$$

$$E_M = \frac{1}{2}\iint_D M^2|\bar{\mathbf{B}} + \mathbf{b}'|^2 dxdy, \qquad (2.39)$$

where the field has a background component, $\bar{\mathbf{B}} = (1, 0)$, and a perturbation $\mathbf{b}' = (b_1', b_2')$. For our study of turbulence, the analogous kinetic background quantities are zero, $\bar{\mathbf{U}} =$

18

$(0,0)$ and $\bar{\Psi} = 0$. Thus, the total KE and PE are the same as the perturbation energies, and the ME can be decomposed as the sum of the background ME (which is constant given our uniform field), the perturbation energy and cross terms.

Since we numerically compute the spectral energy transfers using FFTs of the stream-functions and their derivatives, general non-zero background $\bar{\Psi}, \bar{A}$, which are not periodic across the boundaries, would cause computational issues. One could use cosine transforms to deal with this numerically but that is beyond the scope of this thesis. Luckily, the way in which $\bar{A}$ appears along with its chosen form (linear function of y), allows us to bypass this problem for the ME. For the calculations that follow, we have that $\mathbf{\bar{B}} = (1,0) = (-\partial_y A, \partial_x A) \implies \bar{A} = -y$. To derive the energy fluxes, first define the 2D spectral energy densities in the usual fashion (where * denotes complex-conjugation and hatted quantities are in spectral or wavenumber space)

$$\hat{V} = \frac{1}{2}\hat{\mathbf{u}} \cdot \hat{\mathbf{u}}^* \left(\frac{L}{2\pi}\right)^2, \quad \hat{P} = \frac{F^2}{2}\hat{\psi} \cdot \hat{\psi}^* \left(\frac{L}{2\pi}\right)^2, \quad \hat{M} = \frac{M^2}{2}\hat{\mathbf{b}} \cdot \hat{\mathbf{b}}^* \left(\frac{L}{2\pi}\right)^2, \qquad (2.40)$$

such that we can relate them to the physical energies via the discrete version of Parseval's Theorem,

$$E_V(t) = \sum_{k_x}\sum_{k_y} \hat{V}(k_x, k_y, t)\Delta k_x \Delta k_y,$$

$$E_P(t) = \sum_{k_x}\sum_{k_y} \hat{P}(k_x, k_y, t)\Delta k_x \Delta k_y, \qquad (2.41)$$

$$E_M(t) = \sum_{k_x}\sum_{k_y} \hat{M}(k_x, k_y, t)\Delta k_x \Delta k_y,$$

as the sum of the spectral energy density at every wavenumber $\mathbf{k} = (k_x, k_y)$ in the system, and where $\Delta k_x = \Delta k_y = 2\pi/L$. Then, with $L \to \infty$, we get the integral forms[4],

$$E_V(t) = \int_{k_x}\int_{k_y} \hat{V}(k_x, k_y, t)dk_x dk_y,$$

$$E_P(t) = \int_{k_x}\int_{k_y} \hat{P}(k_x, k_y, t)dk_x dk_y, \qquad (2.42)$$

$$E_M(t) = \int_{k_x}\int_{k_y} \hat{M}(k_x, k_y, t)dk_x dk_y,$$

---

[4]The common statement of Parseval's Theorem, where the pre-factors are already absorbed into the spectral densities

which are easier to deal with analytically. Now, let us make the typical assumption that the flow is isotropic such that $\hat{V} = \hat{V}(k,t)$, $\hat{P} = \hat{P}(k,t)$ and $\hat{M} = \hat{M}(k,t)$, where $k = |\mathbf{k}|$. Of course, when the magnetic field is strong enough, anisotropy will occur and we expect that the flow will tend to align in the direction of the field. In such a case, the isotropic assumption is not appropriate and one should resort to looking at the two-dimensional spectra. We leave this avenue of research as future work. Then, transform the integrals to polar coordinates and find

$$E_V(t) = \int_0^{2\pi} d\theta \int_0^\infty \hat{V}(k,t)k\,dk = \int_0^\infty \hat{E}_V(k,t)dk, \tag{2.43}$$

$$E_P(t) = \int_0^{2\pi} d\theta \int_0^\infty \hat{P}(k,t)k\,dk = \int_0^\infty \hat{E}_P(k,t)dk, \tag{2.44}$$

$$E_M(t) = \int_0^{2\pi} d\theta \int_0^\infty \hat{M}(k,t)k\,dk = \int_0^\infty \hat{E}_M(k,t)dk, \tag{2.45}$$

where the azimuthally integrated energy spectra are defined as

$$\hat{E}_V(k,t) = 2\pi k\hat{V}(k,t), \quad \hat{E}_P(k,t) = 2\pi k\hat{P}(k,t), \quad \hat{E}_M(k,t) = 2\pi k\hat{M}(k,t). \tag{2.46}$$

We now derive the evolution equations of $\hat{E}_V(k,t) + \hat{E}_P(k,t)$ and $\hat{E}_M(k,t)$. Recall the model equations (2.4) and rewrite them decomposing A into a stationary (barred) and perturbation (primed) part. The result reads

$$\partial_t q + \mathbf{u} \cdot \nabla q = M^2 \mathbf{b} \cdot \nabla j + \frac{1}{R_e}\nabla^2 q, \tag{2.47}$$

$$\partial_t A + \mathbf{u} \cdot \nabla(\bar{A} + A') = \frac{1}{R_m}j. \tag{2.48}$$

Since our considered background field is constant and uniform, $\bar{A} = -y$ is independent of time and has a zero current ($\bar{j} = \nabla^2\bar{A} = 0$). Then, the total current is just the perturbed component $j = \bar{j} + j' = j'$. The background $\bar{A}$ will however remain explicitly in the advective term in the A equation above. If $\mathbf{u} = (u,v)$, then $\mathbf{u} \cdot \nabla\bar{A} = -v$, and we can write[5]

$$\partial_t q + \mathbf{u} \cdot \nabla q = M^2 \mathbf{b} \cdot \nabla j + \frac{1}{R_e}\nabla^2 q, \tag{2.49}$$

$$\partial_t A + \mathbf{u} \cdot \nabla A' = v + \frac{1}{R_m}j. \tag{2.50}$$

---

[5]This effectively solves the issue of having to compute the FFT of $\bar{A}$.

Take the Fourier Transform of the above equations to move from physical to spectral space[6]. Then, multiply them by the complex conjugates of $-\hat{\psi}$ and $-\hat{j}$ respectively, to find

$$-\hat{\psi}^*\partial_t\hat{q} = \hat{\psi}^*\widehat{\mathbf{u}\cdot\nabla q} - M^2\hat{\psi}^*\widehat{\mathbf{b}\cdot\nabla j} + \frac{1}{R_e}k^2\hat{\psi}^*\hat{q}, \tag{2.51}$$

$$-\hat{j}^*\partial_t\hat{A} = \hat{j}^*\widehat{\mathbf{u}\cdot\nabla A'} - \hat{j}^*\hat{v} + \frac{1}{R_m}\hat{j}^*\hat{j}. \tag{2.52}$$

Analogously, find the conjugates of the above equations. Adding the original and conjugate equations together make the resulting equations real and they can be written as (where $\Re$ denotes the real part)

$$\partial_t(k^2+F^2)|\hat{\psi}|^2 = 2\Re\left(\hat{\psi}\widehat{\mathbf{u}\cdot\nabla q}^* - M^2\hat{\psi}\widehat{\mathbf{b}\cdot\nabla j}^*\right) - 2R_e^{-1}k^2(k^2+F^2)|\hat{\psi}|^2 \tag{2.53}$$

$$\partial_t M^2 k^2|\hat{A}|^2 = 2M^2\Re\left(\hat{j}\widehat{\mathbf{u}\cdot\nabla A'}^* - \hat{j}\hat{v}^*\right) - 2M^2 R_m^{-1}|\hat{j}|^2, \tag{2.54}$$

recalling that q, j are related to ψ, A in spectral space via

$$\hat{q} = -(k^2+F^2)\hat{\psi}, \quad \hat{j} = -k^2\hat{A}. \tag{2.55}$$

We multiplied (2.54) by M^2 for the following calculations. In physical space, the velocity, vorticity and streamfunction are related by derivatives (analogously for the magnetic quantities). However, in spectral space, these derivatives become factors of the appropriate wavenumber. This allows us to algebraically relate the spectral fields and energies, where

$$2\hat{V}\left(\frac{2\pi}{L}\right)^2 = |\hat{\mathbf{u}}|^2 = \frac{k^2|\hat{q}|^2}{(k^2+F^2)^2} = k^2|\hat{\psi}|^2 = 2\frac{F^2}{k^2}\hat{P}\left(\frac{2\pi}{L}\right)^2,$$

$$2\hat{M}\left(\frac{2\pi}{L}\right)^2 = M^2|\hat{\mathbf{b}}|^2 = M^2k^2|\hat{A}|^2 = M^2\frac{|\hat{j}|^2}{k^2}.$$

The left hand sides of (2.53) and (2.54) then become time-derivatives of the 2D spectral energy densities, $\hat{V}+\hat{P}, \hat{B}$ and so providing the 2D budgets[7]

$$\partial_t(\hat{V}+\hat{P}) = \left(\frac{L}{2\pi}\right)^2\Re\left(\hat{\psi}\widehat{\mathbf{u}\cdot\nabla q}^* - M^2\hat{\psi}\widehat{\mathbf{b}\cdot\nabla j}^*\right) - \frac{2}{R_e}k^2(\hat{V}+\hat{P}),$$

$$\partial_t\hat{M} = \left(\frac{L}{2\pi}\right)^2 M^2\Re\left(\hat{j}\widehat{\mathbf{u}\cdot\nabla A'}^* - \hat{j}\hat{v}^*\right) - \frac{2}{R_m}k^2\hat{M}.$$

---

[6]The remaining $\hat{A}$ in the time derivative will soon be replaced by the total ME, which is doubly periodic since the background field is constant and uniform.

[7]In the case of forced turbulence, with say forcing f in the evolution equation for q, then the corresponding spectral energy budget would have an additional term of the form $-\left(\frac{L}{2\pi}\right)^2\Re(\hat{\psi}\hat{f}^*)$.

The 1D spectral budgets for the azimuthally integrated spectra only differ from the above by a factor of $2\pi k$ with the isotropic assumption[8]. Multiplying through, find the 1D fluxes to read (where all quantities depend on k and t)

$$\partial_t \hat{E}_H = T_q + T_L + D_H, \tag{2.56}$$

$$\partial_t \hat{E}_M = T_A + D_M, \tag{2.57}$$

where we introduce the hydrodynamic energy (HE), containing both kinetic and potential for convenience, $\hat{E}_H = \hat{E}_V + \hat{E}_P$, and further defining the nonlinear transfers between k along with viscosity and diffusion as

$$T_q(k,t) = 2\pi k \left(\frac{L}{2\pi}\right)^2 \Re\left(\hat{\psi}\widehat{\mathbf{u}\cdot\nabla q}^*\right), \qquad \text{Advection of } q, \tag{2.58}$$

$$T_L(k,t) = -2\pi k M^2 \left(\frac{L}{2\pi}\right)^2 \Re\left(\hat{\psi}\widehat{\mathbf{b}\cdot\nabla j}^*\right), \qquad \text{Lorentz Force}, \tag{2.59}$$

$$T_A(k,t) = 2\pi k M^2 \left(\frac{L}{2\pi}\right)^2 \Re\left(\hat{j}\widehat{\mathbf{u}\cdot\nabla A'}^* - \hat{j}\hat{v}^*\right), \qquad \text{Advection of } A, \tag{2.60}$$

$$D_H(k,t) = -\frac{2}{R_e}k^2\hat{E}_H, \qquad \text{Viscosity}, \tag{2.61}$$

$$D_M(k,t) = -\frac{2}{R_m}k^2\hat{E}_M, \qquad \text{Magnetic Diffusion}. \tag{2.62}$$

We saw in deriving the evolution of the energy that the Lorentz force and the advection of A effectively cancelled in (2.19). This suggests that both terms are describing the same exchange of energy between $\hat{E}_H$ and $\hat{E}_M$. To reinforce this idea, we will find in computing the transfers (Chapter 4) that $T_L + T_A$ conserves energy. One could show this analytically but it is not included here. If we integrate the sum of (2.56) and (2.57) over all wavenumbers, we get that the total energy $E(t) = \int_0^\infty \hat{E}(k,t)dk$ with $\hat{E} = \hat{E}_H + \hat{E}_M$, evolves with

$$\partial_t E(t) = \int_0^\infty T(k,t)dk + \int_0^\infty D(k,t)dk, \tag{2.63}$$

where $T = T_q + T_L + T_A$ is the sum of all transfers due to the dynamics and $D = D_H + D_M$ is the sum of viscous and diffusive effects. In the absence of a uniform background magnetic field, the $-\hat{j}\hat{v}^*$ term in T_A vanishes. Energy must be conserved in the absence of dissipation

---

[8]Otherwise, we can simply replace $2\pi k$ by the azimuthal integral and multiplying by k.

(when $D = 0$) and so $\int_0^\infty T(k)dk$ must be zero. Since $T(k)$ is therefore conservative, it is customary to formulate it as a wavenumber divergence where

$$T(k,t) = -\partial_k \Pi, \quad \Pi(k,t) = -\int_0^k T(k',t)dk', \qquad (2.64)$$

and Π is referred to as the spectral energy flux [97]. The conservative property of $T(k)$ in terms of Π then reads $\Pi(k \to \infty, t) = 0$. We further define the components of the spectral energy flux in the same way for later computations and plotting,

$$\Pi_{q,L,A}(k,t) = -\int_0^k T_{q,L,A}(k',t)dk', \qquad (2.65)$$

corresponding to the respective transfers with the same subscript. In the simulations considered in this thesis, the spectral transfers and associated fluxes are computed to verify the direction of the energy cascade and quantify the contribution of each term and its related physical process.

2.6   Linear Stability Analysis of QG-MHD

When exploring the dynamics of the QG-MHD equations (which contain 2D and QG hydrodynamics along with 2D-MHD in their various limits), one would like to understand how the flow evolves with time. However, the nonlinearity of the model often makes this difficult to answer exactly. Nevertheless, using linear stability analysis (LSA), we can find an underlying theory for particular flows, such as jets. Perturbing this state and linearizing the resulting equations for the disturbances, we can determine what solutions grow in time, and how quickly they do so. This allows for the prediction of the flow evolution for early times, after which nonlinearity may dominate. We derive the linear stability problem for a flow in the x-direction (only dependent on the cross-stream coordinate) under the influence of a uniform parallel magnetic field.

2.6.1   Perturbation

Recall the evolution of the PV and the magnetic streamfunction from (2.5) and (2.6). Assume that we have an exact steady solution to these equations that only depends on the y-coordinate. We define the background fields as

$$\bar{\psi} = \bar{\Psi}(y), \qquad \bar{A} = \bar{A}(y), \qquad \bar{u} = U(y) = -\partial_y \bar{\Psi}, \qquad \bar{b} = B(y) = -\partial_y \bar{A}, \qquad (2.66)$$

along with a background PV, $\bar{q} = \bar{Q}(y) = \partial_{yy}\bar{\Psi} - F^2\bar{\Psi}$, where the flow is in the x-direction. Next, assume that small amplitude perturbations can depend on either spatial coordinate and time, $q'(x, y, t), A'(x, y, t)$. If we substitute a perturbed basic state,

$$q = \bar{Q}(y) + q', \qquad A = \bar{A}(y) + A', \tag{2.67}$$

into the governing nonlinear equations, the smallness of the perturbations allows us to neglect the nonlinear terms. Physically, this means we neglect the advection of the perturbation by the pertubation but still maintain the advection of the pertrubation by the mean state and the advection of the mean state by the perturbation.

2.6.2 Linearized Equations

Using the aforementioned decomposition, the linearized governing equation are then

$$\partial_t q' + J(\bar{\Psi}, q') + J(\psi', \bar{Q}) - M^2 J(\bar{A}, \nabla^2 a') - M^2 J(a', \nabla^2 \bar{A}) - \frac{1}{R_e}\nabla^2 q' = 0,$$
$$\partial_t A' + J(\psi', \bar{A}) + J(\bar{\Psi}, A') - \frac{1}{R_m}\nabla^2 A' = 0, \tag{2.68}$$

which we can rewrite using the form of the basic state (which is independence of x),

$$\partial_t q' - (\partial_y\bar{\Psi})(\partial_x q') + (\partial_x\psi')(\partial_y\bar{Q}) + M^2\left((\partial_y\bar{A})(\partial_x\nabla^2 A') - (\partial_x A')(\partial_y\nabla^2\bar{A})\right) - \frac{1}{R_e}\nabla^2 q' = 0,$$
$$\partial_t A' + \partial_x\psi'\partial_y\bar{A} - \partial_y\bar{\Psi}\partial_x A' - \frac{1}{R_m}\nabla^2 A' = 0. \tag{2.69}$$

Using the definitions for the velocity and magnetic field such that $U = -\partial_y\bar{\Psi}$ and $B = -\partial_y\bar{A}$, our equations finally read

$$\partial_t q' + U\partial_x(\nabla^2\psi') - U_{yy}\partial_x\psi' - M^2 B\partial_x\nabla^2 A' + M^2 B_{yy}\partial_x A' - \frac{1}{R_e}\nabla^2 q' = 0,$$
$$\partial_t A' - B\partial_x\psi' + U\partial_x A' - \frac{1}{R_m}\nabla^2 A' = 0, \tag{2.70}$$

where the terms proportional to F from the PV in the second and third terms cancel via:

$$-\partial_y\bar{\Psi}(\partial_x\nabla^2\psi' - F^2\partial_x\psi') + \partial_x\psi'(\partial_y\nabla^2\bar{\Psi} - F^2\partial_y\bar{\Psi}) = U\partial_x(\nabla^2\psi') - U_{yy}\partial_x\psi'. \tag{2.71}$$

2.6.3   Fourier Decomposition

Since the domain is assumed to be periodic in the x-direction and we are looking for wave-like solutions, we assume that the perturbation can be decomposed as,

$$\psi' = \hat{\psi}(y)\exp[i(kx - \omega t)], \qquad A' = \hat{A}(y)\exp[i(kx - \omega t)], \qquad (2.72)$$

which in turn transforms the 2D Laplacian operator as $\hat{\nabla}^2 = \partial_{yy} - k^2$. Substituting this into our linear equation and dividing through by the exponential, we find (multiplying by i/k and using $\hat{q} = (\hat{\nabla}^2 - F^2)\hat{\psi}$)

$$\left(\frac{\omega}{k}(\hat{\nabla}^2 - F^2) - U\hat{\nabla}^2 + U_{yy} - \frac{i}{kR_e}\hat{\nabla}^2(\hat{\nabla}^2 - F^2)\right)\hat{\psi} + M^2\left(B\hat{\nabla}^2 - B_{yy}\right)\hat{A} = 0,$$
$$\frac{\omega}{k}\hat{A} + B\hat{\psi} - (U + \frac{i}{kR_m}\hat{\nabla}^2)\hat{A} = 0, \qquad (2.73)$$

or in matrix form, (as a generalized eigenvalue problem: $A\mathbf{v} = cB\mathbf{v}$, with $c = \omega/k$)

$$\begin{bmatrix} (U + \frac{i}{kR_e}(\hat{\nabla}^2 - F^2))\hat{\nabla}^2 - U_{yy} & -M^2(B\hat{\nabla}^2 - B_{yy}) \\ -B & U + \frac{i}{kR_m}\hat{\nabla}^2 \end{bmatrix}\begin{bmatrix}\hat{\psi} \\ \hat{A}\end{bmatrix} = c\begin{bmatrix}\hat{\nabla}^2 - F^2 & 0 \\ 0 & 1\end{bmatrix}\begin{bmatrix}\hat{\psi} \\ \hat{A}\end{bmatrix}. \quad (2.74)$$

In the absence of viscosity and diffusion, the matrices are purely real and the system reduces to[9]

$$\begin{bmatrix} U\hat{\nabla}^2 - U_{yy} & -M^2(B\hat{\nabla}^2 - B_{yy}) \\ -B & U \end{bmatrix}\begin{bmatrix}\hat{\psi} \\ \hat{A}\end{bmatrix} = c\begin{bmatrix}\hat{\nabla}^2 - F^2 & 0 \\ 0 & 1\end{bmatrix}\begin{bmatrix}\hat{\psi} \\ \hat{A}\end{bmatrix}. \qquad (2.75)$$

The linear stability problem we concern ourselves with in this thesis is (2.74), restricted to a Bickley jet in a constant magnetic field (Chapter 5). The system is solved numerically in Python using the generalized eigenvalue problem solver in the SciPy library [96] along with Chebyshev differentiation matrices for the derivatives [93]. For specified ranges of the nondimensional parameters F, M, and looping in parallel over a range of wavenumbers, the solver is asked to find the growth rate and spatial structure of any unstable mode.

2.7   Numerical Method for Nonlinear Simulations

The code used in this thesis [90] can solve three types of problems. First, we can evolve purely hydrodynamic flows while using the A variable as an optional passive tracer by

---

[9]In a β-plane geometry, the first entry of the left matrix simply gains an additional term of $+\beta$.

setting $M = 0$ (effectively turning off the Lorentz force). Next, the code can solve the A equation with a constant prescribed velocity (what we refer to as pure induction, e.g. [99]). Finally, the code can solve the coupled evolution of both the PV and A and this is the main focus of the following chapters. The code is equipped to consider general non-uniform background fields $B(x, y)$ but this is not an avenue we explore.

The code for the nonlinear evolution is written in Python and makes use of a spectral Galerkin method through the Shenfun library which runs efficiently in parallel [65, 64]. A spectral Galerkin method solves partial differential equations (PDEs) through a special form of the method of weighted residuals (WRM) using global basis functions. We use the Fourier basis which works most efficiently on a doubly periodic domain. To allow the study of non-periodic solutions, we evolve the perturbation fields in the PV (q) and magnetic streamfunction (A), while the optional background $\bar{Q}$ and $\bar{A}$ remain stationary. This becomes especially useful when studying a balanced state such as the Bickley jet (Chapter 5).

The computational domain is a doubly periodic square of length L with N points along each edge. The solution is evolved in time (with sufficiently small dt) using the third-order Adams-Bashforth (AB3) scheme, where the first step is forward Euler and the second step uses the second-order Adams-Bashforth method. The dissipative terms are solved for explicitly. In all simulations we use an exponential filter proposed initially by Godon and Shaviv (1993) [36] for numerical stability, given our Fourier basis[10]. Specifically, we take the filter $f(k)$, with form (where $k_{max} = 2\pi N/L$, $k_m = 0.9k_{max}$, $k_s = 0.8k_{max}$)

$$f(k) = \exp(-\alpha|k|^\beta), \quad \beta = 1.88/\ln(k_m/k_s), \quad \alpha = 0.69k_s^{-\beta}, \tag{2.76}$$

which is further plotted in Figure 2.1 for convenience. For a computational domain of length L and resolution N, the maximum wavenumber is $k_{max} = Ndk$ with spacing $dk = 2\pi/L$. We tested the use of a sharp, wavenumber-cutoff filter which set all spectral components at wavenumber $|k| \geq \frac{2}{3}k_{max}$ equal to zero [67] and saw no noticeable differences in the evolution for our considered resolution given smaller dt. The code saves snapshots of the physical fields (in HDF5 format) at a user-determined frequency and automatically computes a set of diagnostics using the output fields after the simulation is complete[11]. In the following chapters, we use $L = 8\pi$, $N = 1024$, $dt = 2.5 \times 10^{-4}$.

Having established how the code evolves the nonlinear equations, we now move on to the methods used in post-processing and the most relevant computed diagnostics. First, we will use the Taylor (and the analogous magnetic quantity) microscales to crudely estimate

---

[10]This filter was also investigated in Christopher Subich's PhD thesis (2011) [86].

[11]If the code is ran in serial, this is done on-the-fly.
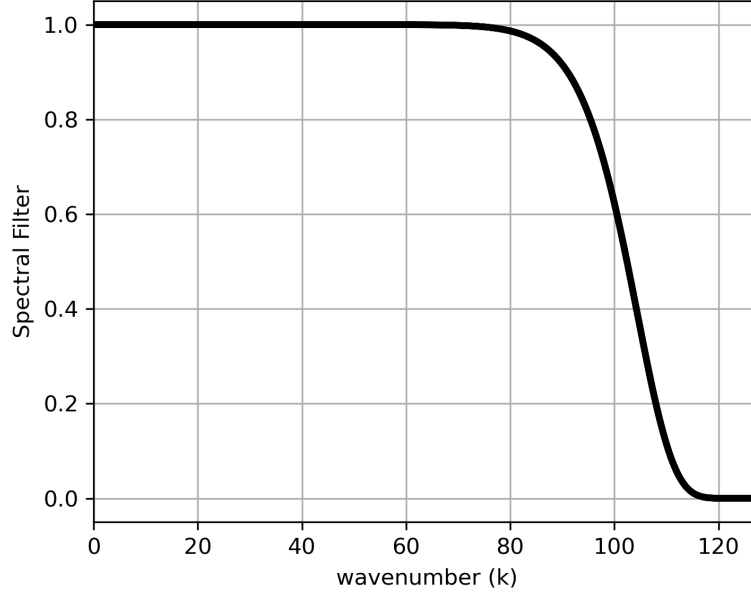
Figure 2.1: Exponential type spectral filter (2.76) used in all simulations herein, with $L = 8\pi$ and $N = 1024$.

the typical length scales of the turbulent flow (as in [26]). An increase or decrease in these scales tell us whether the KE and ME are moving to larger or smaller length scales, allowing us to confirm the direction of the energy cascade. They read

$$L_u = \frac{\langle |\mathbf{u}|^2 \rangle^{1/2}}{\langle (\nabla^2 \psi)^2 \rangle^{1/2}}, \quad L_b = \frac{\langle |\mathbf{b}|^2 \rangle^{1/2}}{\langle (\nabla^2 A)^2 \rangle^{1/2}}, \tag{2.77}$$

where the angled-brackets indicate a domain average. We also consider some bulk measure of the anisotropy of the KE and ME since the considered flows are not always isotropic [83, 89]. Specifically, we shall compute the anisotropy of the velocity ($\mathbf{u} = (u_1, u_2)$) and magnetic field ($\mathbf{b} = (b_1, b_2)$) via

$$\text{Anisotropy}(\mathbf{u}) = \frac{\langle u_1^2 \rangle}{\langle u_1^2 \rangle + \langle u_2^2 \rangle}, \quad \text{Anisotropy}(\mathbf{b}) = \frac{\langle b_1^2 \rangle}{\langle b_1^2 \rangle + \langle b_2^2 \rangle}. \tag{2.78}$$

These determine on a scale of 0 to 1 how much of the kinetic and magnetic energies are concentrated along the x-direction. Apart from quantifying the anisotropy inflicted by the uniform field, this also provides some insight as to how accurate our isotropic

assumption is in the computation of the 1D spectral slopes and fluxes. The code is two-dimensional (physical space has (x, y) and spectral space has (k_x, k_y)) but we wish to analyze the energy spectra in a single dimension (as a function of $k = \sqrt{k_x^2 + k_y^2}$) to compare with the expected slopes from MHD turbulence theory. As we did in computing the 1D spectral fluxes ((2.56) and (2.57)), we take the isotropic assumption on the two-dimensional spectra and use azimuthal integration in wavenumber-space, on the annulus of area $\pi((k + dk)^2 - k^2)$ to convert a function $f(k_x, k_y)$ to an azimuthally integrated $f(k)$. Whenever spatial derivatives are needed in post-processing, we use the Fastest Fourier Transform in the West (FFTW) [32]. Note that the total energy spectrum has three components in general,

$$\hat{E}(k) = \hat{E}_V + \hat{E}_P + \hat{E}_M \tag{2.79}$$

for the KE, PE, and ME, respectively. Spectral slopes ($\alpha_{V,P,M}$) for the azimuthally integrated energies are computed such that $\hat{E}_{V,P,M}(k) \propto k^{\alpha_{V,P,M}}$ by fitting a line to a temporally averaged log plot of the spectrum in a finite range of wavenumbers. We pick this range in a region where $\ln \hat{E}_{V,P,M}(k)$ is approximately linear and in the inertial range. The PE spectrum is only relevant when $F \neq 0$ and is related to the KE via $F^2 \hat{E}_V = k^2 \hat{E}_P$. The energy transfers T_q, T_L, T_A defined in (2.62), in addition to the analogous viscous/diffusive quantities, will also be temporally averaged to provide a clear picture of the dynamics.

Armed with some well-established and some new theory, a vast array of scalar outputs, and of course snapshots of the physical fields, we set off to study our numerical experiments.

Chapter 3

Dynamic Vortices in MHD

Studying vortices allow us to better understand the dynamics of turbulent flows. This chapter aims to showcase the respective influences of magnetism (M) and a weak free-surface (F) in a simple local context where the initial conditions (ICs) consist of balanced or nearly balanced vortices. The three cases described below are heavily inspired by those considered by Weiss in [99]. Weiss assumed a fixed velocity, where the magnetic potential A is a passive tracer. We relax this restriction and let the velocity freely evolve. Our deviation from the profiles used in Weiss' work (especially for the cases of multiple vortices) is motivated by the fact that those velocities were not stationary solutions to the momentum equation. Since our velocity evolves with time, the flow becomes complicated very quickly even in the hydrodynamic limit ($M = 0$). Instead, we keep our formulation purely in terms of trigonometric functions, defined piece-wise where appropriate. The hydrodynamic evolution of these cases is much more stable/coherent, allowing us to focus on the influence of the field and free-surface as opposed to complicated hydrodynamics. Where we have doubly periodic boundary conditions across the results of this thesis, Weiss considered perfectly conducting boundary conditions with fixed magnetic field lines at the relevant boundaries, along with eighth order polynomials in the streamfunction for sufficient decay at these boundaries.

We consider three cases: 1) a single vortex (SV), 2) a row of vortices (RV) aligned with the field and with alternating polarity, and finally 3) a two by two arrangement of vortices,

much like a chess board (TV). Our ICs are set in the kinetic streamfunction and read

$$\psi_{SV}(t=0) = \begin{cases} \frac{L}{4\pi}\cos(4\pi\frac{x}{L})\cos(4\pi\frac{y}{L}), & |x-L/2| < L/8, |y-L/2| < L/8 \\ 0, & \text{otherwise} \end{cases} \tag{3.1}$$

$$\psi_{RV}(t=0) = \begin{cases} -\frac{L}{4\pi}\sin(4\pi\frac{x}{L})\cos(4\pi\frac{y}{L}), & |y-L/2| < L/8 \\ 0, & \text{otherwise} \end{cases} \tag{3.2}$$

$$\psi_{TV}(t=0) = -\frac{L}{2\pi}\cos(2\pi\frac{x}{L})\cos(2\pi\frac{y}{L}), \tag{3.3}$$

where $L = L_x = L_y = 8\pi$. We initialize the perturbation streamfunction $\psi = \psi'$ in the code to create the cases mentioned above. Of course, had one wanted to investigate the linear stability of these vortices, one would initialize the background streamfunction instead. It is straightforward to compute the associated initial velocity and vorticty fields by $\mathbf{u} = (-\partial_y\psi, \partial_x\psi)$ and $q = \nabla^2\psi - F^2\psi$. The velocity scale is $U = 1$ and since the ICs are set in ψ, the initial KE is independent of F. The amplitude of the initial PV however varies with F and we do not initialize any noise in the perturbation A. The first two cases (SV, RV) are not exact stationary solutions to (2.4) in the hydrodynamic limit. However, their respective evolutions are stable enough when $M = 0$ to warrant a nice comparison with the presence of a magnetic field. In the third case, the TV is a stationary solution to the inviscid hydrodynamic problem. Dissipation and numerical noise could eventually allow this solution to become unstable, but this was not observed on the considered time-scale ($t < 300$) for our chosen parameters. The negative signs of the last two streamfunctions were picked to replicate the relative orientations (to the magnetic field) of the corresponding ICs in Weiss' work. However, since the domain is doubly-periodic, this is purely a cosmetic choice as we can shift our plotting domain by $L/2$ in any required direction to get the other sign. Clockwise motion is presented below in blue (negative q) and counter-clockwise motion in red (positive q).

3.1   Rigid Lid

We shall begin by considering the three different configurations of vortices in a rapidly rotating (f-plane) barotropic fluid with a rigid-lid. This is easily obtained by setting the rotational Froude number, $F = 0$, and is a subset of QG-MHD equivalent to the typical 2D-MHD model. In this section, we present plots of the PV (equal to the relative vorticity in this case) and A (magnetic potential) at different times and with different strengths of magnetism. We will touch on two phenomena from the established literature on MHD

vortices. The first is magnetic flux expulsion and this happens when the velocity of the vortex distorts the background magnetic field. The field lines are stretched on the periphery of the vortex until they reconnect and expel the field lines remaining in the core to the edges. Weiss was particularly interested in this behaviour and Moffatt and Kamkar 1983 [63] later found that flux expulsion has a time scale of $\tau_{fe} = R_m^{1/3} t_0$ where t_0 is a time-scale characterising the flow and R_m is the magnetic Reynolds number. Flux expulsion is a kinematic behaviour as opposed to a dynamic one since Weiss observed it without evolving the velocity field.

The stretching of the weak large-scale field generates a strong small-scale field, where the amplification factor was found to scale with $R_m^{1/2}$ [94]. Once the small scale field is large enough to be dynamically important, magnetic tension (the restoring force which straightens bent magnetic field lines) can influence the velocity field through the vorticity equation. This phenomenon is inherently dynamic and appears when vortices stretch out the uniform background field to form regions of concentrated current on their edges. The magnetic stresses associated with these current sheets are released once magnetic field lines reconnect. The process then leads to vortex disruption in shape and strength, and possibly even destruction. The vortex disruption regime is one where the curl of the Lorentz force competes with the advection of PV. Assuming that the length and velocity scales of the vortex in question are comparable to that of the mean flow, the scaling result for this regime is given by the criterion $M^2 R_m = \mathcal{O}(1)$, as derived by Mak et al. 2017 [57]. Armed with this theory, we now turn our attention to the numerical experiments.

3.1.1 Single Vortex

Snapshots of the PV for the SV case are provided in Figure 3.1, for selected times and strengths of the magnetic field. We see in the first row that without an active field ($M = 0$), the vortex core largely remains untouched by the final depicted time. Including the slightest influence of magnetism when $M = 10^{-3}$ on the next row, we develop a diamond pattern outside the periphery, where the vortex appears to interact with its mirror image across the doubly-period boundary (as also seen in the case of a Gaussian vortex [25]). The next step in magnetic strength ($M = 10^{-2}$) is far more interesting where the vortex core now generates filaments of PV in the periphery ($t = 100$) that become unstable and generate turbulent flow ($t = 200$)[1]. This flow is then advected azimuthally by the core and the resulting band grows radially to largely destroy the shape of the core by the final

---

[1]We have approximately 5 grid points across the width of these thin filaments with our considered resolution.

Figure 3.1: Snapshots of the PV for a single vortex (ψ_{SV}) in a rigid lid, for increasing $M = 0, 10^{-3}, 10^{-2}, 10^{-1}$ and at times $t = 20, 100, 200, 300$.

time ($t = 300$). The magnetic Reynolds number $R_m = 10^4$ and this relative strength in magnetism $M = 10^{-2}$ provide the relationship that $R_m M^2 = 1$, in perfect agreement with the vortex disruption criterion mentioned before.

Finally, when $M = 10^{-1}$, the magnetic field is strong and the dynamics are drastically different. First, the vortex core quickly separates into thick bands of PV intertwined with thinner filaments of the opposite parity ($t = 20$). These are stopped abruptly before $t = 100$ and are forced to uncoil in the opposite direction of the original vortex velocity. The strong effects of magnetic tension opposing the deformation of the magnetic field lines have made this flow somewhat elastic. At the next time, the uncoiled filaments of PV generate a new vortical structure directly on the boundary of the domain and the remaining dynamics present an oscillation about the two structures. Coiling motions are forced to uncoil and the main behaviour of the flow features oscillations. In a case not presented where $M = 1$, we find nonlinear Alfvén waves reminiscent of those seen in Magill et al. 2019 [55]. QG-MHD does not filter out Alfvén waves the same way QG filters out gravity waves. However, since we consider $M < 0.1$ in our simulations, the Alfvén wave speed (V_A) is smaller than the typical velocity by at least a factor of 10. The result is a different regime in which Alfvén waves are not very obvious in the evolution. Thus for a SV, we find that the dynamics shift with increasing magnetic field strength from a stable coherent structure, to the generation of small scale filaments of PV along the periphery which eventually disrupt the vortex core, and finally elastic and oscillatory behaviours.

For this case, we also include an analogous figure for the perturbation magnetic streamfunction, A in Figure 3.2. Notice in the first column that the early evolution of A is almost identical for all values of M. In the last column however, we can see strong evidence of the diamond pattern seen in the PV figure for the first two rows ($M = 0, 10^{-3}$). Since A looks the same in the hydrodynamic and weak field cases, but the diamond pattern only arises in the PV for the weak field case, it is possible that the diamond behaviour is a magnetic one. The magnetic streamfunction is passive in the hydrodynamic case and very weakly active when $M = 10^{-3}$ but the pattern reflected in the PV appears coupled to the shape of the perturbation A. This warrants further investigation not included in this thesis.

A closer investigation of the A field reveals that expulsion of magnetic flux occurs and is obvious for the hydrodynamic and weak field cases ($M = 0, 10^{-3}$) within the considered temporal range. In the hydrodynamic regime, where the Lorentz force is zero, A is passively advected by the flow, with no influence back onto the stable velocity. For the weak field when $M = 10^{-3}$, the velocity field is still largely stationary and also gives a good approximation to the kinetic treatment of the equations presented by Weiss. The fingerprint for flux expulsion can be seen in the absence of magnetic field lines or analogously in little to no amplitude of A left in the core of the vortices. Since we are plotting
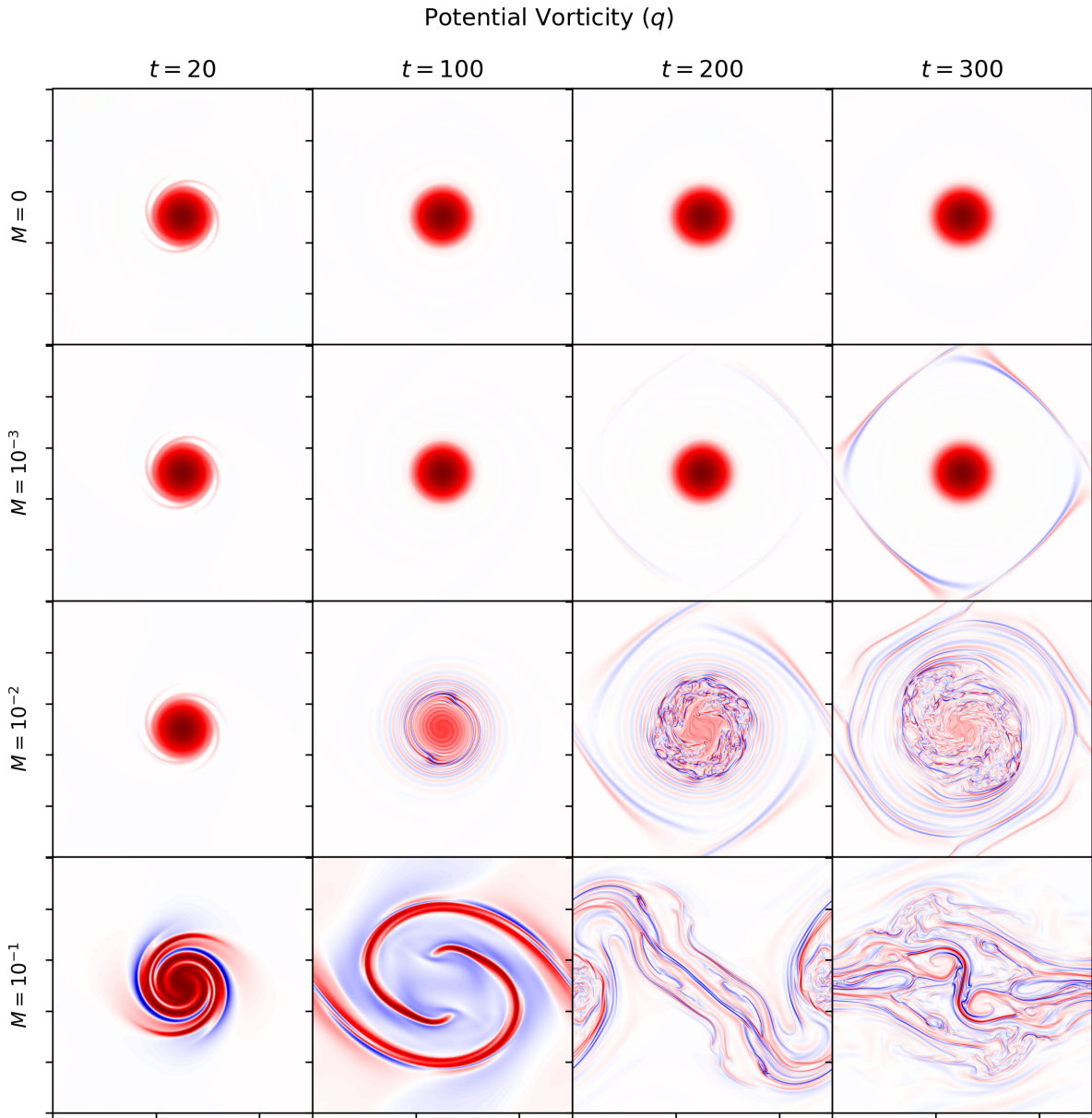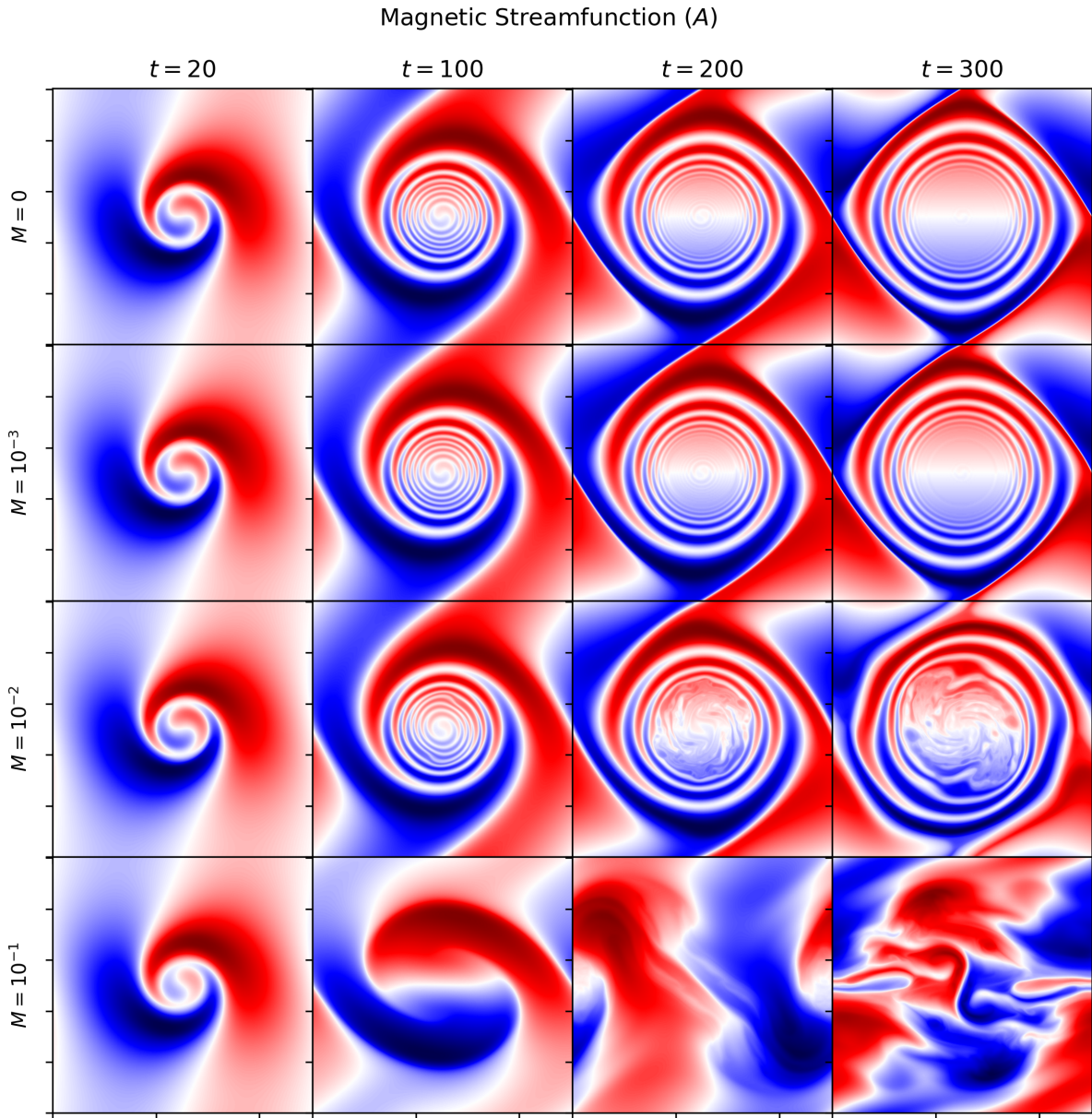
Figure 3.2: Snapshots of the magnetic streamfunction A for a single vortex (ψ_{SV}) in a rigid lid, for increasing $M = 0, 10^{-3}, 10^{-2}, 10^{-1}$ and at times $t = 20, 100, 200, 300$.

the perturbation A, the weak gradients remaining in the core are but the negative of the background magnetic streamfunction. For the intermediate strength of magnetism where $M = 10^{-2}$, we do see some evidence of flux expulsion in earlier times, but the behaviour is more difficult to diagnose later where the vortices are disrupted and borderline into turbulent flow. The strongest case of magnetism provides a flow with largely elastic properties (where PV tends to uncoil) and so the behaviour is difficult to see even at early times. These results are by no means inconsistent with the findings of Weiss. Since flux expulsion is a kinetic behaviour, it follows that we should observe it when the field has little to no effect onto the velocity. This is the case for both $M = 0, 10^{-3}$ at all depicted times and the early times of $M = 10^{-2}$ where the perturbation field is still small enough. We however see the clear transition from a kinetic to a dynamic regime where magnetic field strongly influences the velocity for large enough M and t.

3.1.2   Single Row of Vortices

Having seen what happens to a SV with increasing magnetic field strength, we venture to see what differs when we have multiple vortices next to each other in single-file. This is the (RV) case depicted in Figure 3.3, showing again the PV field for selected times and values of M. The hydrodynamic limit in the first row presents elliptical vortex cores surrounded by thin filaments of PV with the same parity of the core they stretch out of. These filaments originate from the initial transition of square to elliptical vortices and diffuse by the final time. With the mere presence of active magnetism in the next row ($M = 10^{-3}$), we see that these filaments of PV give rise to smaller scale features, such as vortical filaments with the opposite parity of the respective core ($t = 100$). The resulting evolution presents the cores largely untouched surrounded by a rather geometrically pleasing arrangement of PV filaments. This flow however is hardly a turbulent one and is still dominated by the original coherent shape of the ICs.

The instability of PV filaments is much more pronounced in the next row ($M = 10^{-2}$) where smaller vortices are generated through secondary instabilities along the periphery of the original vortices. These are ejected into plumes (or mushroom caps) above and below the faint remainder of the original cores ($t = 100$). The plumes retract towards the original cores presenting a saw-tooth shaped envelope, which encloses a turbulent and small-scale flow ($t = 200$). At the final time, the field and diffusive processes have smoothed out the flow, where the filaments of PV have slightly thickened in comparison to the two previous times. These appear bounded by a wide band envelope in the horizontal direction, replacing the saw-tooth pattern. Again, this value of M is the vortex disruption regime. The final case with largest magnetic influence ($M = 10^{-1}$) presents an evolution free of

Potential Vorticity (q)

Figure 3.3: Snapshots of the PV for a row of vortices (ψ_{RV}) in a rigid lid, for increasing $M = 0, 10^{-3}, 10^{-2}, 10^{-1}$ and at times $t = 20, 100, 200, 300$.

coherent vortices, where the PV is very quickly concentrated along the initial filaments which dominate the flow even at $t = 20$. Similar to the SV case, this flow is highly oscillatory and rather square in shape, where PV filaments are often parallel with one of the domain axes. This evolution shows a pulse travelling upwards and then downwards through the PV filaments, while widening the effective domain of the flow in the y-direction.

Thus, for a row of square vortices aligned with the magnetic field, increasing M moves the evolution from a regime of coherent elliptical vortices, to one with plumes of ejected PV between the cores, to again an abrupt disruption of the coherent structures and a resulting oscillatory behaviour. In terms of specific differences between this case and the SV, the total initial KE more than doubled (not shown here) and we have lost the previous symmetry in the x and y-directions. While the turbulence generated in the periphery of the $M = 10^{-2}$ SV case was still being advected azimuthally by the final time, the same case of M for a row lost all traces of the initial vortices. The vortex disruption regime was however consistent at this value of M in both sets of ICs. Finally for the strongest field, instead of an oscillation about two vortical structures as seen in the SV case, the combined effects of each vortex pair creates pulses across the collection of vortices in the positive and negative y-directions.

3.1.3   Two by Two Vortices

Finally, having seen what happens to a SV and a row of them, we would like to investigate a configuration with two by two vortices where the vortex cores are completely surrounded by identical copies of each other (with the opposite polarity). This is the case we have included in Figure 3.4. Compared to the RV, the case of $M = 0$ does not evolve, in agreement with our computation that this state is stationary in the hydrodynamic and inviscid limit. With the presence of weak active magnetism in the next row ($M = 10^{-3}$), we see that filaments of PV with the opposing parity form and surround the cores in a symmetrical fashion ($t = 100$). These start to deform by the final time but the outline of the ICs remains, though fainter since the filaments have a larger amplitude in comparison. In the next row ($M = 10^{-2}$), the filaments of PV have already become large in amplitude in the region between the square cores by $t = 20$. These give rise to smaller vortices of much higher strength than the ICs along the periphery ($t = 100$). The resulting turbulent flow is advected toward the center of the domain through the left and right (in between the respective cores) and the consequent convergence ejects the flow to the top and bottom boundaries. Eventually ($t > 200$) the coherent cores vanish and the motion is dominated by a turbulent flow. The case with largest magnetic influence ($M = 10^{-1}$) presents again thick bands of PV that wind and unwind in place of the ICs, generating smaller scale features
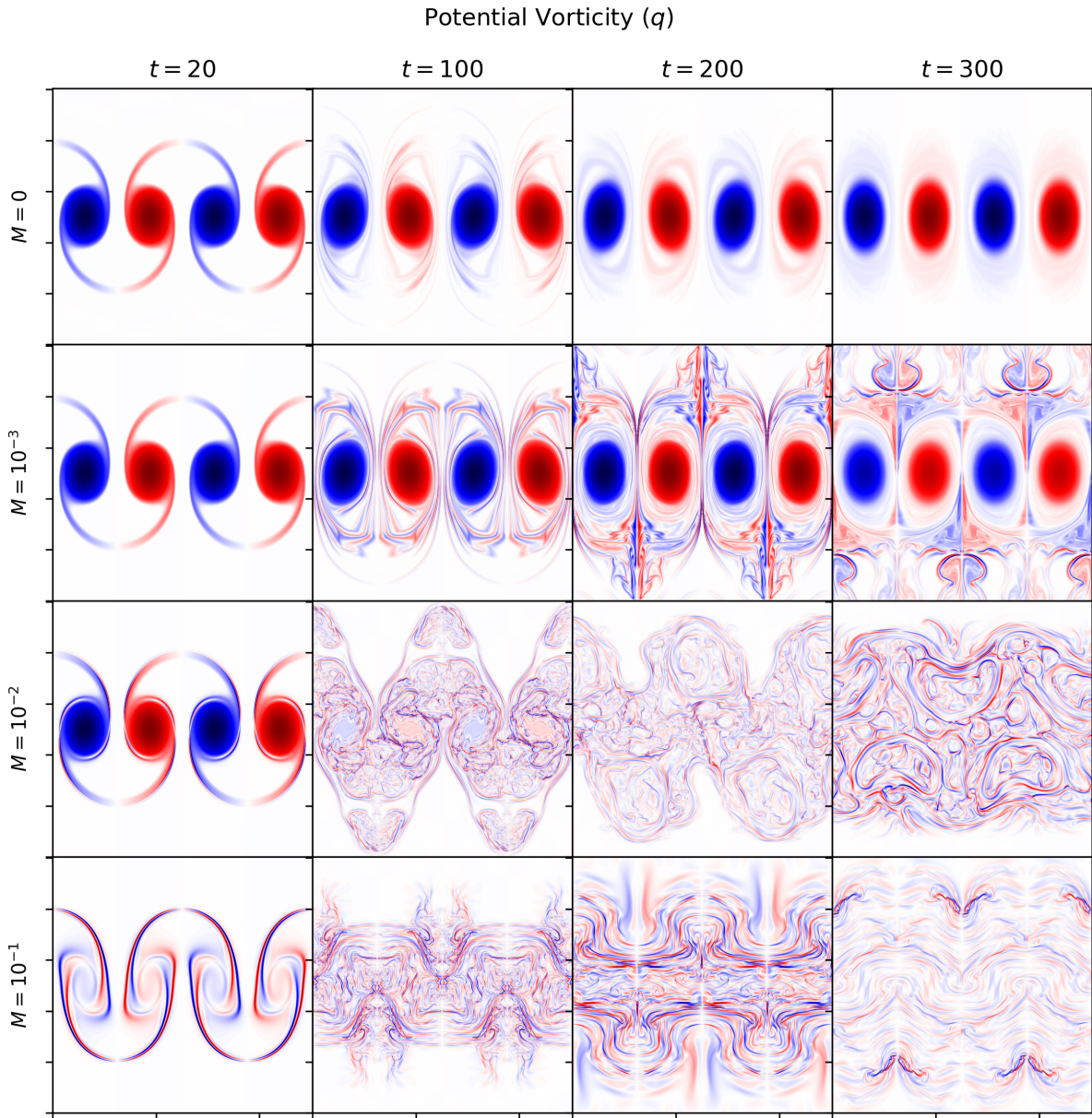
37
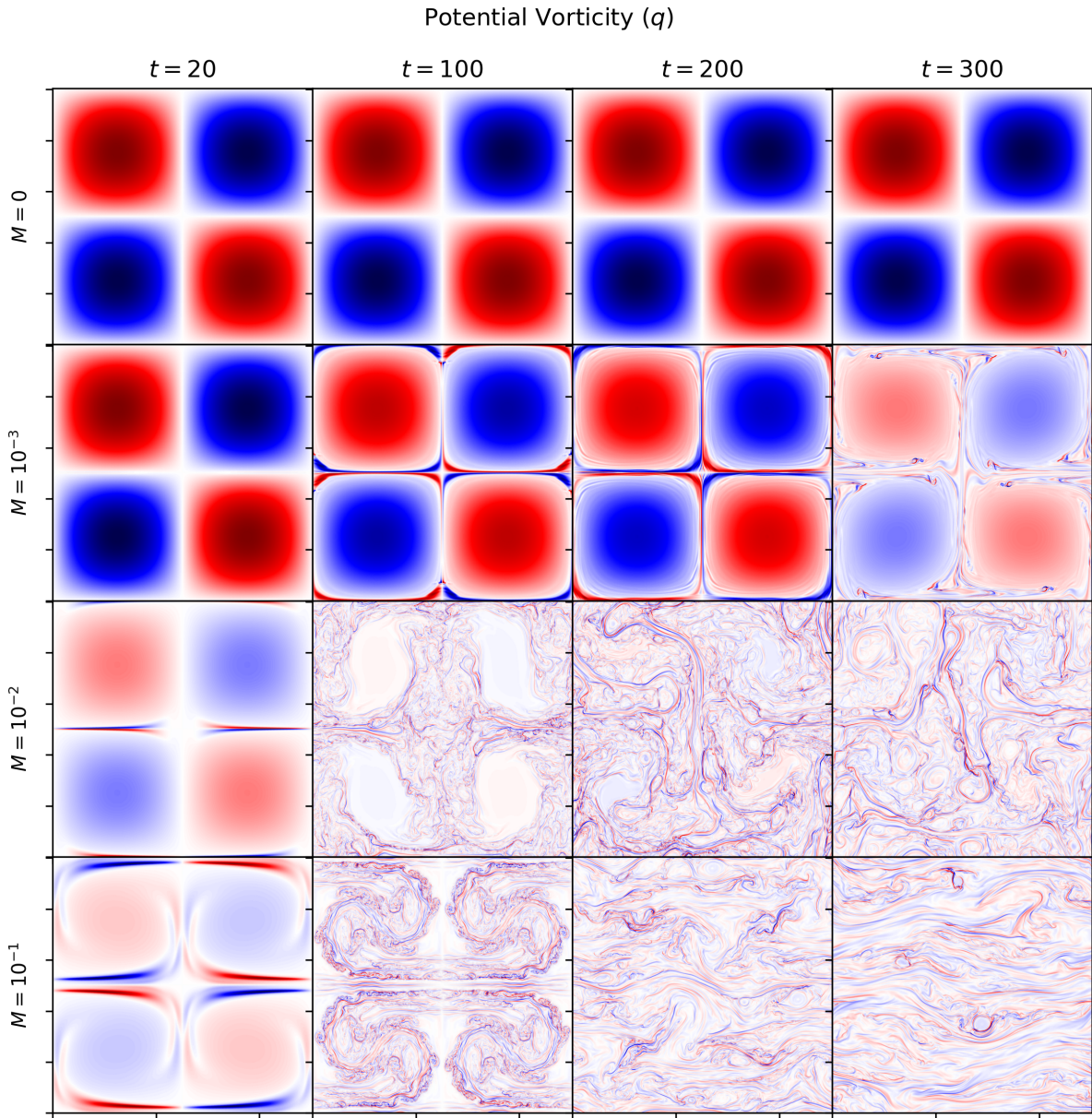
Figure 3.4: Snapshots of the PV for the two by two case (ψ_{TV}) in a rigid lid, for increasing $M = 0, 10^{-3}, 10^{-2}, 10^{-1}$ and at times $t = 20, 100, 200, 300$.

thereafter ($t = 100$). After some time ($t > 200$) PV filaments dominate the flow and tend to organise into horizontal bands, parallel with the field (reminiscent of the generation of zonal jets in a β-plane, [92]). This is clear evidence of the expected anisotropy due to the constant uniform field, where this rather turbulent flow was generated by a very coherent arrangement of large-scale vortices.

In comparison to the SV and the RV, this case presents vortices of larger length scale and a greater initial KE (approximately 3 times larger than the RV). The geometry of these ICs is also domain-filling and symmetric in all directions whereas the RV only filled the domain in the x-direction (with dead-space above and below) and the SV was rather isolated. Where the row case showed some evidence of flow alignment with the field for example when $M = 10^{-2}$, this two by two case presents a much clearer picture for the strongest $M = 10^{-1}$. Increasing the magnetic field strength in all cases considered so far have common features, including the generation of smaller scales PV filaments in the periphery of large scale vortices, the eventual disruption of vortices from the Lorentz force, the tendency of the flow to align with the field, and elastic-like properties in the fluid when M is large enough. Some differences arose as well, where for example the SV and RV have not reached a regime of near-total alignment in the x-direction compared to the TV.

3.2 Free-Surface

Now that we have seen what magnetism does to various arrangements of vortices, we can add the additional complexity of a weak free-surface by setting our rotational Froude number $F = 1$. This is QG-MHD and we leave the regime equivalent to 2D-MHD, where now both the effects of rotation and the free-surface are present. This implies a flow which has a tendency to generate a typical length scale equal to the external Rossby radius R_d in the hydrodynamic dimensional equations. To our knowledge, the problem of a weak free-surface has not yet been numerically investigated in the literature for QG-MHD and we are thus on exploratory ground. In this section, nonzero F provides the additional contributions from the surface in the definition of the PV, $q = \nabla^2\psi - F^2\psi$, compared to the PV in the previous section which only considered the relative vorticity.

3.2.1 A Single Vortex

The SV case when $F = 1$ is shown in Figure 3.5 to compare with Figure 3.1 (rigid lid). Even the weak magnetic field case of $M = 10^{-3}$ now remains stationary up to $t = 300$ and

Figure 3.5: Selected snapshots of the PV for a single vortex (ψ_{SV}) with a weak free-surface ($F = 1$) for increasing $M = 0, 10^{-3}, 10^{-2}, 10^{-1}$ and at times $t = 20, 100, 200, 300$.

the diamond pattern we had discussed before has vanished in all cases. The $M = 10^{-2}$ case (third row) shows that filaments of PV are still generated on the vortex periphery, but they are smaller in amplitude (relative to the ICs) compared to the rigid lid case and the original core is still largely coherent. The weak free-surface (F non-zero) has slowed the instability of the vortex periphery in the $M = 10^{-2}$ case, suggesting that a new criterion for vortex disruption may be needed to include the effects of a free-surface. Though the regime of vortex disruption was described by the competition between the advection of the PV and the Lorentz force, F now appears in the definition of the PV and can alter the balance.

The strongest case of $M = 10^{-1}$ is not so elastic anymore. Though the initial evolution is similar, where wide arms of PV unwind, the evolution at later times show a collection of smaller vortices being advected counterclockwise in the wake of the initial vortex. In a rigid lid, we saw an oscillation about two vortical structures for this M, one in the center of the domain and one directly on the boundary. We now see that the wide bands of PV (which cross the periodic boundary to connect the system to itself) are relatively stationary and feed the counter-clockwise motion inside the center. The rotational Froude number F has already been found to be stabilizing to jets in hydrodynamics [73] and as we will see in Chapter 5, it is still stabilizing to them in the presence of magnetic fields. The results of this section suggest that it has a similar effect on the stability of MHD vortices. Though a detailed study (through linear theory for example) of how F stabilizes these structures is not provided, we see that it has the same qualitative compacting effects consistent with the hydrodynamic theory [75].

To investigate further upon the loss of the diamond pattern, the perturbation A for $F = 1$ is provided in Figure 3.6 to compare with Figure 3.2 (in a rigid lid). Notice that the diamond pattern is absent and the bulk of A is compacted in the immediate periphery of the vortex, with the exception of the largest strength of magnetism. However, the inclusion of a weak free-surface does not seem to disrupt flux expulsion from the core in the first two cases and even the third, as it is still present. Again, since the velocity is largely stationary for weak magnetic fields, this is in good qualitative agreement with Weiss' results.

3.2.2   A Single Row of Vortices

Moving on to the row case when $F = 1$, the PV is shown in Figure 3.7 to compare with Figure 3.3 (rigid lid). Similar to the change we saw in the SV case, the weak field on the second row is essentially identical to the hydrodynamic limit above it. Both present slightly elliptical vortices which keep their shape and coherence by the final time. The

Magnetic Streamfunction (A)
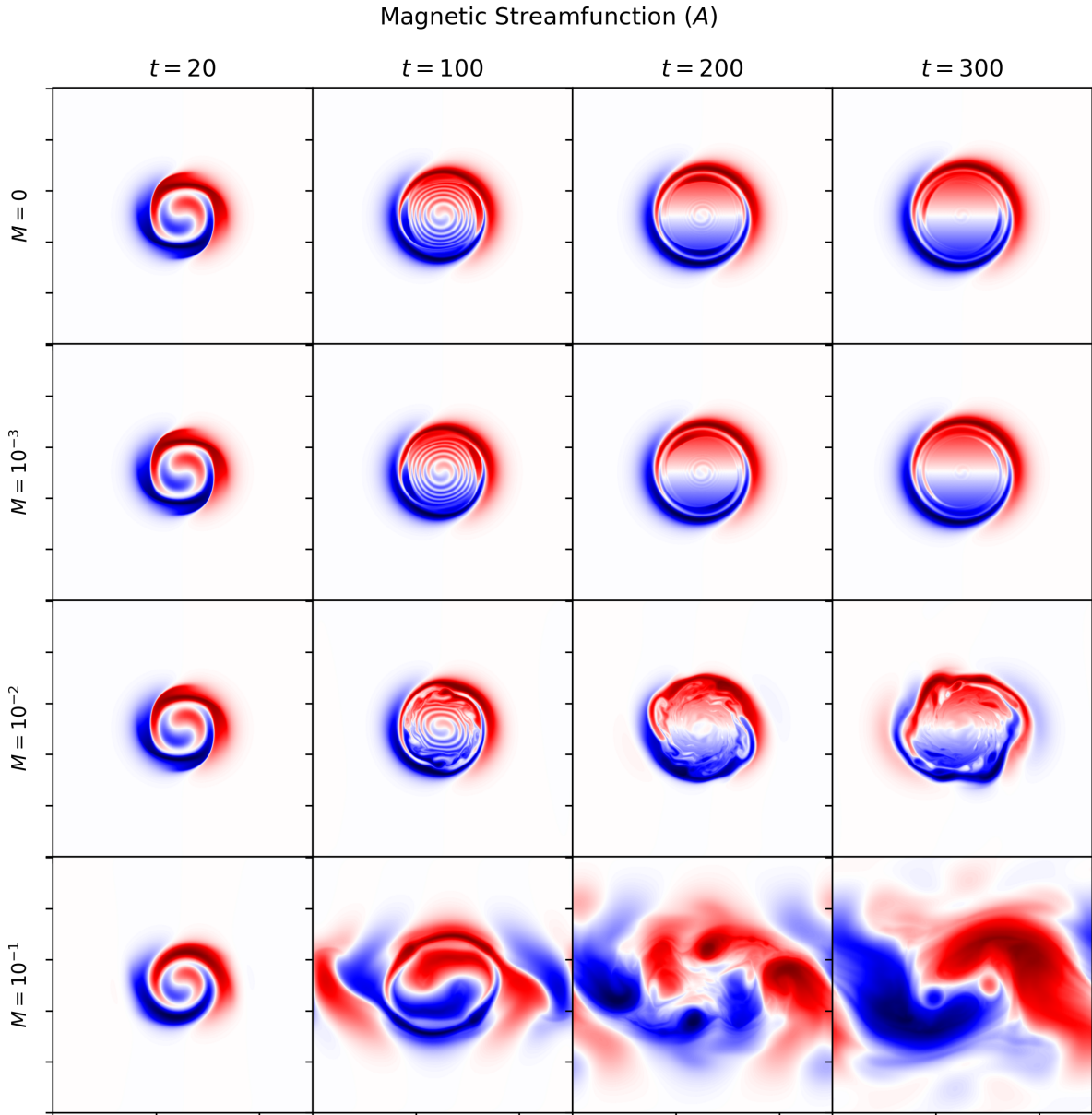
Figure 3.6: Snapshots of the magnetic streamfunction A for a single vortex (ψ_{SV}) with a weak free-surface ($F = 1$) for increasing $M = 0, 10^{-3}, 10^{-2}, 10^{-1}$ and at times $t = 20, 100, 200, 300$.

next row ($M = 10^{-2}$) is again much more interesting but dynamically tamed compared to the rigid lid analogue. We can still see traces of the ICs whereas with a rigid lid this flow became a thick band of turbulence. The evolution shows the generation of small scale PV filaments through the instability of the vortex periphery but their effect on the larger vortices appears suppressed once again, reinforcing the need for an adapted criterion of vortex disruption in a free-surface. For the strong field case, the early evolution shows the suppression of the elastic behaviour we saw with a rigid lid where the periphery of the smaller scale vortices are now the dominating features of the flow ($t = 100$). This is a similar behaviour as we saw for a SV with $F = 1$. The resulting organisation is not so much aligned with the field but rather a thick band of vortex filaments for which the envelope resembles a sine wave in x.

3.2.3   Two by Two Vortices

Finally, for the TV case when $F = 1$, the PV is shown in Figure 3.8 to compare with Figure 3.4 with a rigid lid. Again, the weak field case is very similar to the hydrodynamic case with the exception of very weak features being generated in the corners of the large vortices. The intermediate regime of $M = 10^{-2}$ still shows the generation of small scale features, advected towards the centre through the sides and expelled through the top and bottom, but their influence on the coherence of the ICs is again impeded. The strongest case shows slightly stronger filaments being generated but the faint traces of the ICs remain and the evolution at the final time is qualitatively similar to the row above it where we have lost the complete alignment with the field that we saw in the rigid lid case.

Given what we have seen in the qualitative behaviour of the various ICs, we suspect that the generation of small scale features in the flow and their consequent disruption of coherent vortices is affected by F, where the inclusion of a weak free-surface has stabilizing effects on the flow. This parameter has also prevented the TV case from reaching a flow almost completely aligned with the field, as seen in the rigid lid case. Further for the strongest field considered in the RV case, the sharp and square features of the flow in a rigid lid were replaced by a stream of PV filaments enclosed by a smooth sine-wave in the direction of the field. Thus, F does not only act on the generation of small scale features in the early evolution for increasing M, but also in the long-term sense with more tame and spatially compact evolutions. The interactions of M and F warrant a new formal investigation of the vortex disruption criterion and possibly flux expulsion in a free-surface.
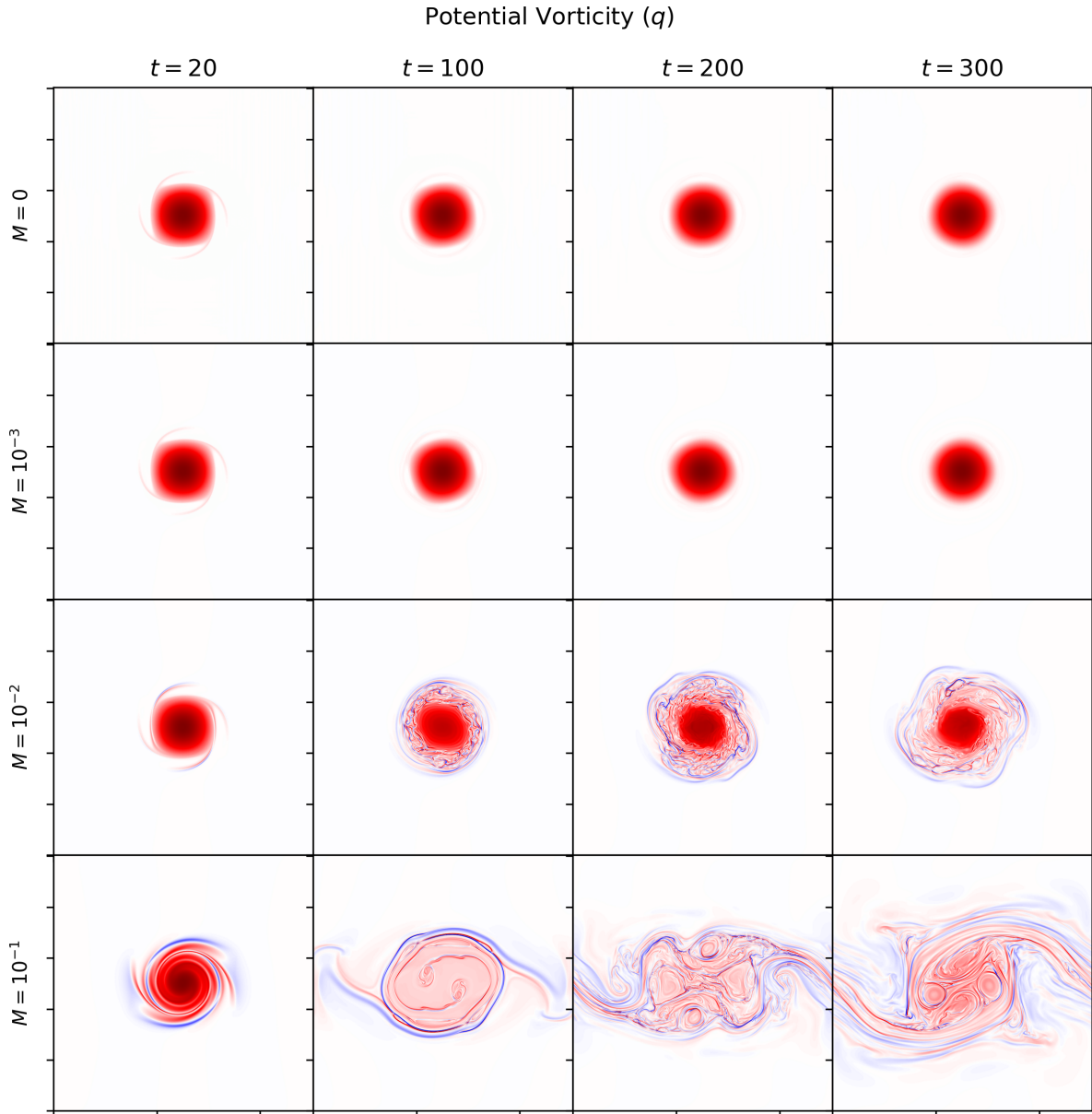
Potential Vorticity (q)

Figure 3.7: Selected snapshots of the PV for a row of vortices (ψ_{RV}) with a weak free-surface ($F = 1$) for increasing $M = 0, 10^{-3}, 10^{-2}, 10^{-1}$ and at times $t = 20, 100, 200, 300$.
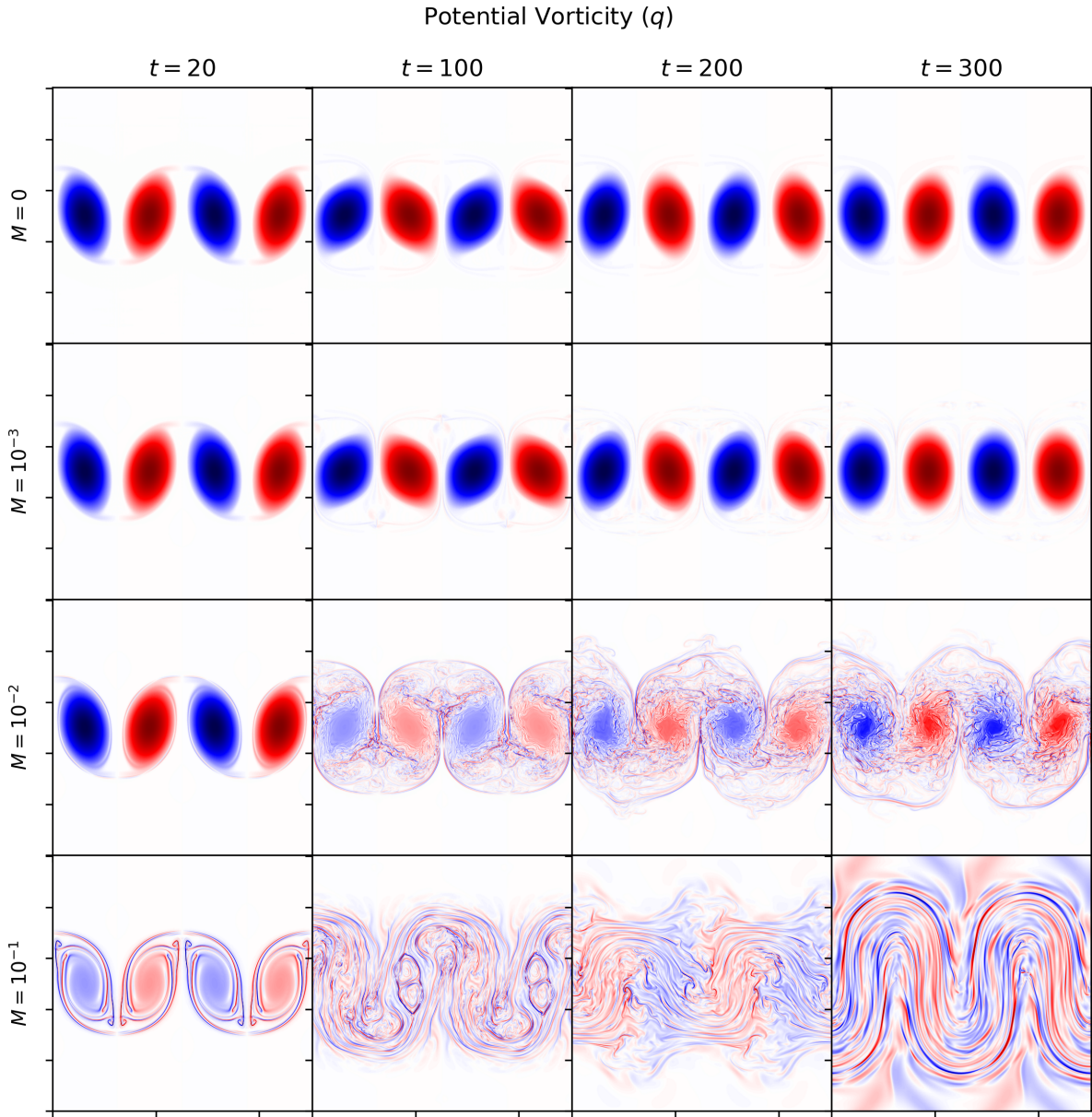
Potential Vorticity (q)
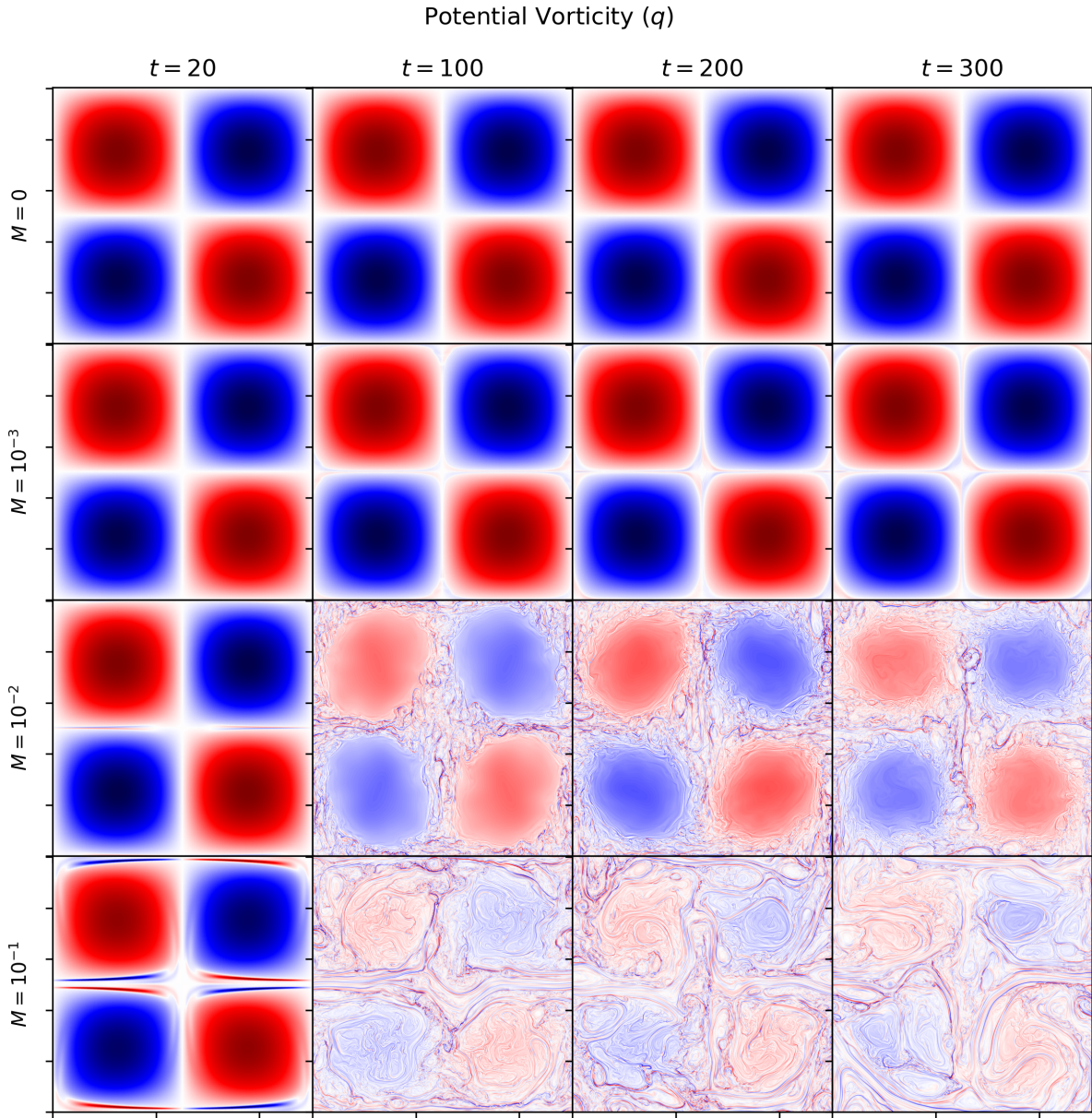
Figure 3.8: Selected snapshots of the PV for the two by two case (ψ_{TV}) with a weak free-surface ($F = 1$) for increasing $M = 0, 10^{-3}, 10^{-2}, 10^{-1}$ and at times $t = 20, 100, 200, 300$.

3.3 Length Scales and Anisotropy

We will close this chapter by introducing our first computations of the diagnostics presented in Chapter 2. This will provide a quantitative view of the results we have seen thus far and support for our observations on the effects of increasing magnetic field strength and a free-surface. Since including every quantity and related figure would be cumbersome in this chapter, we will assess the differences in the flow of the TV case when changing M and F. We focus on the TV case since the hydrodynamic evolution is stationary and the consequent inclusion of magnetic effects will provide simple and clear differences in the diagnostics.

Figure 3.9 shows the microscales of the TV case as defined in (2.77), which estimate the typical length scales of the KE and ME (the gradients of the respective streamfunctions) and not that of the streamfunctions themselves. Plotting the KE at $t = 0$ as a function of (x, y) for example would show that square regions of KE have a length scale closer to 3 and not 4π which would approximate the length scale of the streamfunction for the TV case (exactly half of the domain). The bottom boundary of all panels in this figure is chosen as the grid scale, for reference. The results show that the length scale of the KE of the hydrodynamic rigid lid case (top left panel, black curve) stays around $L_u \approx 3$ for the entire simulation which is consistent with the stationary evolution we observed in Figure 3.4. The very weak field case (dashed red) in the same panel shows little deviation form this trend, again consistent with the dominance of the larger vortices in the evolution.

The next two cases of magnetism show an early drop of about a decade in L_u and while the $M = 10^{-2}$ (dot-dashed green) case shows a consistent decay from 0.3 to 0.2 afterwards, the $M = 10^{-1}$ (dotted blue) case shows some oscillations near the same range. Moving to the panel below (bottom left) for $F = 1$, we see that L_u changes very little when $M = 0, 10^{-3}$ (black, dashed red) from the rigid lid case. One might expect F to alter the length scale of the KE in a turbulent flow and we will see that this is in fact the case in Chapter 4. However, our TV case is stationary or nearly so for weak fields (see Figure 3.8) which explains the lack in change. The more interesting behaviour occurs for the next two values of $M = 10^{-2}, 10^{-1}$ (dot-dashed green, dotted blue) in which L_u has levelled off (near 0.3 for $M = 10^{-2}$ and 0.1 for $M = 10^{-1}$) after the initial decrease (again by a decade or more). Increasing F from 0 to 1, and the consequent inclusion of a weak free-surface, has therefore suppressed the long-term temporal variation in the length scale of the KE. Where the rigid lid evolution did not clearly show the relationship between L_u and M, for the two strongest fields, the case of a free-surface has made made it clear that L_u decreases with M in this regime and varies very little over longer times.

Moving on to the typical scale of the ME in the next column for the rigid lid case (top

Figure 3.9: Kinetic (L_u, left) and magnetic (L_b, right) microscales (2.77) of the two by two case (ψ_{TV}) in a rigid lid (top row, $F = 0$) and with a weak free-surface (bottom row, $F = 1$). The four different values of M are shown as: 0 (solid black), 10^{-3} (dashed red), 10^{-2} (dot-dashed green) and 10^{-1} (dotted blue).
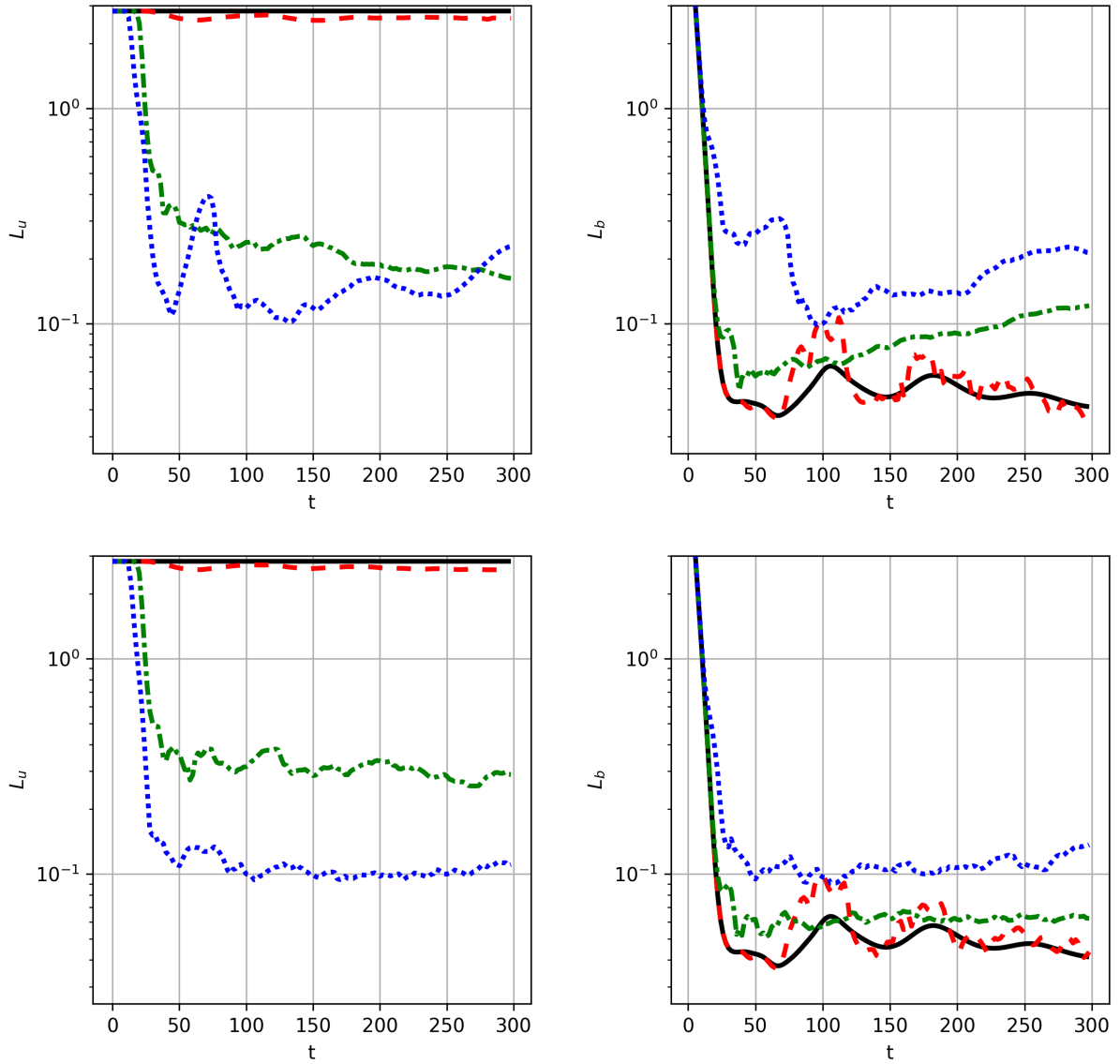
right, $F = 0$), we see a sharp decreasing initial adjustment at early times in L_b. This is unsurprising since the quantity tries to measure the length scale of the total ME, and the initial magnetic field was constant and uniform. We thus focus on the dynamics after this adjustment, where field lines are deformed by the flow ($t > 50$). For the hydrodynamic case, there is no physical ME and this curve is associated with A as a passive tracer. We include this for reference as the asymptotic behaviour of the very weak field case towards the absence of an active field. The definition of L_b is independent of M since it is a ratio of the ME to the current. While the $M = 0$, 10^{-3} (black, dashed red) cases hover near (but above) the grid scale, the $M = 10^{-2}$, 10^{-1} (dot-dashed green, dotted blue) curves tend to increase after the adjustment. Looking at the analogous snapshots of A (not included here) would show that the structure becomes more smooth with time at these values of M and so the associated gradients would be smoother, increasing the typical length scale of the ME. In the panel below with $F = 1$, we see the same behaviour observed in L_u where the $M = 10^{-2}$, 10^{-1} (dot-dashed green, dotted blue) curves have flattened. Thus, when magnetism is strong enough to disrupt a stable solution, the inclusion of a weak free-surface suppresses the long-term temporal variation in the typical length scale of both the KE and ME.

Next, the bulk anisotropy of the KE and ME (2.78) are plotted in Figure 3.10, following the same legend for the values of M from the previous figure. The KE (top left) is exactly isotropic when $M = 0$ and very nearly so when $M = 10^{-3}$, consistent with the symmetry of the TV case and its stationary (or nearly stable) evolution. While the $M = 10^{-2}$ (dot-dashed green) case shows weak oscillations about perfect isotropy, the 10^{-1} (dotted blue) case leaves almost 70% of the KE in the x-direction, consistent with our observation of the flow alignment in this direction for the bottom row of Figure 3.4. Moving to the lower panel when $F = 1$, we see that the KE is more isotropic than before for the $M = 10^{-2}$, 10^{-1} (dot-dashed green, dotted blue) cases while the other two remain virtually untouched. The background magnetic field (aligned in the x-direction) introduces anisotropy by aligning the flow parallel to it for large enough M and consequently for strong enough Lorentz force. However, it appears the weak free-surface works against this alignment and leaves the flow more isotropic in the same time scale.

For the anisotropy of the field itself in the rigid lid case (top right), we see that in all cases of M, the ME starts completely in the x-direction as we would expect from the initial uniform field. The resulting evolution of the ME shows many oscillations in all cases leaving most of the energy either highly concentrated in x, when $M = 0$, 10^{-1} (black, dotted blue), or nearly isotropic when $M = 10^{-3}$, 10^{-2} (dashed red, dot-dashed green). Increasing F to 1 in the bottom right panel, we find that the hydrodynamic case is identical, but while the $M = 10^{-2}$ case is still rather isotropic, the other three leave 60-80% of the ME in the
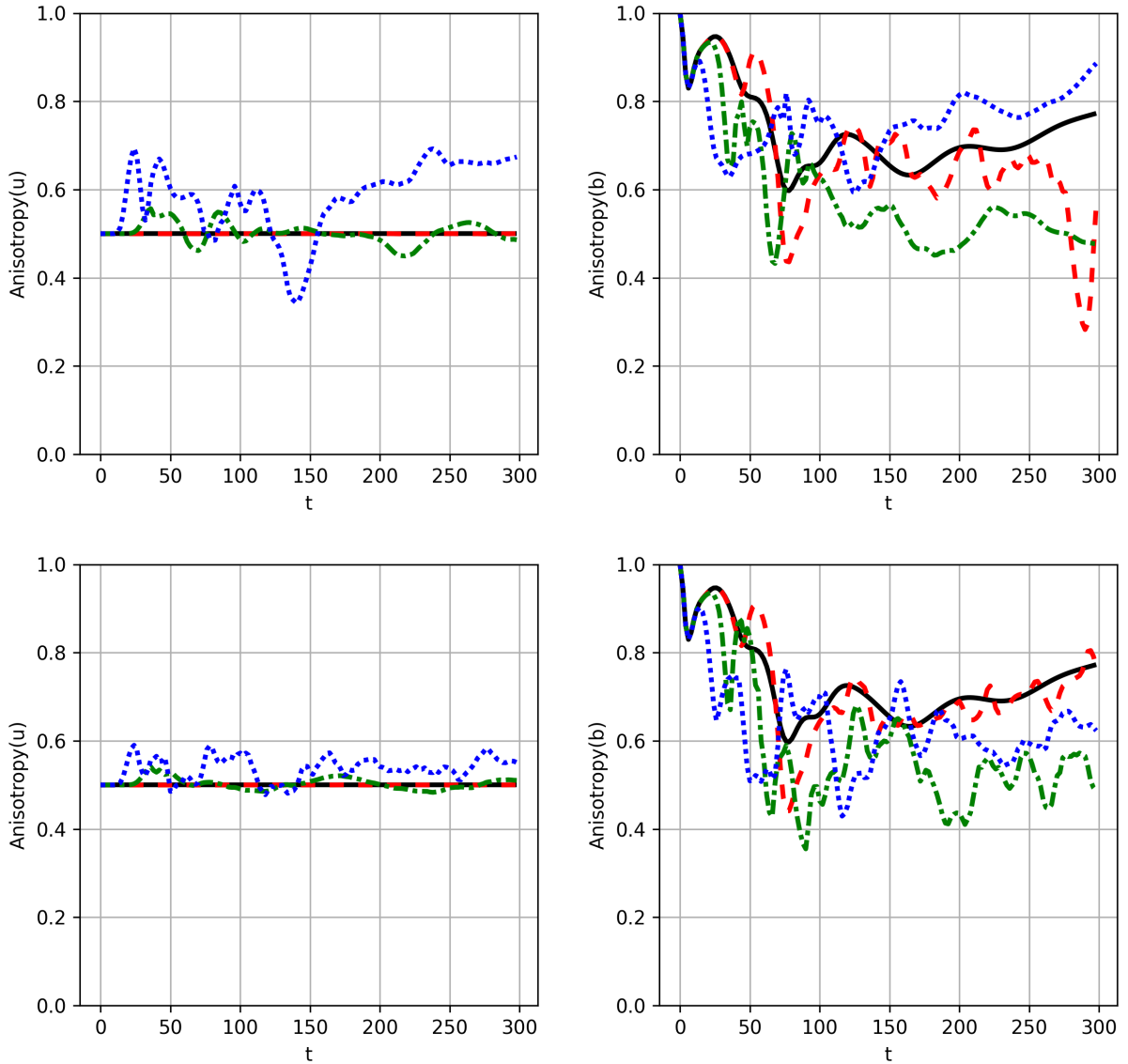
Figure 3.10: Anisotropy norms for the velocity (left) and magnetic field (right) (2.78) of the two by two case (ψ_{TV}) in a rigid lid (top row, $F = 0$) and with a weak free-surface (bottom row, $F = 1$). The four different values of M are shown as: 0 (solid black), 10^{-3} (dashed red), 10^{-2} (dot-dashed green) and 10^{-1} (dotted blue).

x-direction. It is not obvious from this plot that increasing F makes the magnetic field more isotropic but the amplitude of the temporal variation is definitely reduced. The KE is more clearly affected and the behaviours we describe quantitatively above for different F were also present in the SV case. However, these were not clear in the diagnostics of the RV case. We suspect that the anisotropy of those particular ICs are to blame.

Nevertheless, we have seen the effects of magnetism with and without a free-surface on simple configurations of vortices. For small M, the way in which vortices affect the field is clearly seen. Magnetic flux is expelled from the vortex cores and concentrated to the periphery for both a rigid lid and free-surface configuration. In a rigid lid, the Lorentz force induces the small scale filaments of PV along the periphery to amplify and become unstable for large enough M. Their resulting evolution destroys the coherence of the cores in strength and shape. The particular strength at which the field is strong enough to do so is in agreement with the vortex disruption criterion from Mak et al. 2017 [57] dependent on the product of $M^2 R_m = \mathcal{O}(1)$. The strongest magnetic field considered induces elastic and oscillatory behaviour in the flow where magnetic tension opposes the deformation of magnetic field lines. When including a weak free-surface with $F = 1$, we saw that the flow generally becomes more isotropic compared to a rigid lid evolution and the disruption of large vortices is delayed. The timeseries of the microscales also indicate that the free-surface suppresses temporal oscillations in the bulk of the flow and inhibits the alignment of the flow with the field. With this newfound wisdom, we venture into a more complicated picture, turbulence.

Chapter 4

Freely-Decaying MHD Turbulence

Having investigated the effects of a uniform field on the evolution of vortices and collections of vortices, we now shift to a more global focus in the study of freely-decaying 2D turbulence. By freely-decaying, we mean that the model is initialized with a random field in each streamfunction (ψ, A) and the solution is let to evolve without any forcing. Though the code allows for the study of forced turbulence, we leave this avenue of research as future work. The random fields in the kinetic and magnetic streamfunctions are generated using FFTs to transform a perturbed Gaussian function in wavenumber space into a random physical field at a particular range of length scales. In spectral space, the initial streamfunction is given by

$$\hat{\psi}_0(k_x, k_y) = \exp\left(i f_{\mathrm{rand}}(k_x, k_y) - \left(\frac{|\mathbf{k}| - k_t}{\sigma} \right)^2 \right) \tag{4.1}$$

for wave vector $\mathbf{k} = (k_x, k_y)$, spectral width σ, and typical wavenumber k_t. The definition contains a random phase coefficient $e^{i f_{rand}}$ where f_{rand} represents white uniform noise bounded between $[-1, 1]$. We compute $\psi_0(x, y)$ by taking the real part of the inverse FFT of $\hat{\psi}_0$ and then ensuring zero mean and normalizing to achieve a reasonable maximum speed of $\mathcal{O}(1)$. We generate both ψ_0 and A_0 at the same scales, but with different random seeds in f_{rand} so that $\psi_0 \neq A_0$. The typical wavenumber and spectral widths are chosen as $k_t = 0$ and $\sigma = 1$ for this chapter which provides an initial typical length scale of $L \approx 1$ according to the bulk measurement (2.77). Had we wanted to focus on the inverse energy cascade of hydrodynamic turbulence, we would initialize the following simulations with vortices of much smaller length scales ($k_t > 0$) to allow energy to move to larger scales. We would also require a forcing at a particular scale for the inverse cascade to be

applicable. In simulations not included in this thesis, we confirm that this is indeed the behaviour we observe. However, since we are interested in the magnetic behaviour where the energy is expected to cascade to smaller length scales, we pick initial vortices to be sufficiently large. The random seeds also determine the isotropy of the initial velocity (and magnetic field perturbation) and were picked to be isotropic within 1% using the bulk measurements (2.78). The initial magnetic field is almost entirely in the x-direction apart from the isotropic perturbation at 1% the amplitude of the background. Further, there is always more initial KE than there is ME, where even the largest value of $M = 10^{-1}$ still provides an initial ME 4 times smaller than the initial KE. We will first study the spatial structures for different M in a rigid lid and then with a free-surface. We will then compare the diagnostics in the following sections for the various combinations of M and F.

4.1 Rigid Lid

First, we plot the PV for increasing $M = 0, 10^{-3}, 10^{-2}, 10^{-1}$ and at selected times $t = 20, 100, 200, 300$ in Figure 4.1 in a rigid lid configuration with $F = 0$. While the previous chapter focused on coherent structures, this is 2D-MHD turbulence. There are coherent vortices in the flow but they are much more chaotic and arise from random initial conditions. Many vortices of different shapes and sizes are now evolved together to combine and interact. The initial vortices in the previous chapter had a single length scale associated with the size of the vortices, which were arranged in some square grid. Now the initial flow is random with a mean length scale of one in the KE. The first row ($M = 0$) of Figure 4.1 shows vortices that combine and move to larger scales. Given enough time, the merging process will lead a single dipole (two vortices of opposite parity) at largest scales [59]. The second row ($M = 10^{-3}$) shows the onset of magnetic effects for a very weak field where small scale filaments are starting to dominate the amplitude of the PV field. Increasing the field again to $M = 10^{-2}$ in the third row, PV filaments dominate the flow early on and have yet to align with the background field. Finally, in the last case with $M = 10^{-1}$, we see a familiar picture (as we saw for the strong field case in the two by two vortex) where the flow aligns significantly with the field. Further, investigating the plots of the other physical fields (not included here) has shown that the PV is increasingly slaved/correlated to the magnetic current, j for larger M. This relates to the cross-helicity dynamo behaviour mentioned by Yokoi (2013) [101] but a complete discussion on the matter is beyond the scope of this thesis.

Though the initial conditions considered in this chapter are much more complicated than the square vortices from before, much of the same dynamics still occur. This shows a

Potential Vorticity (q)
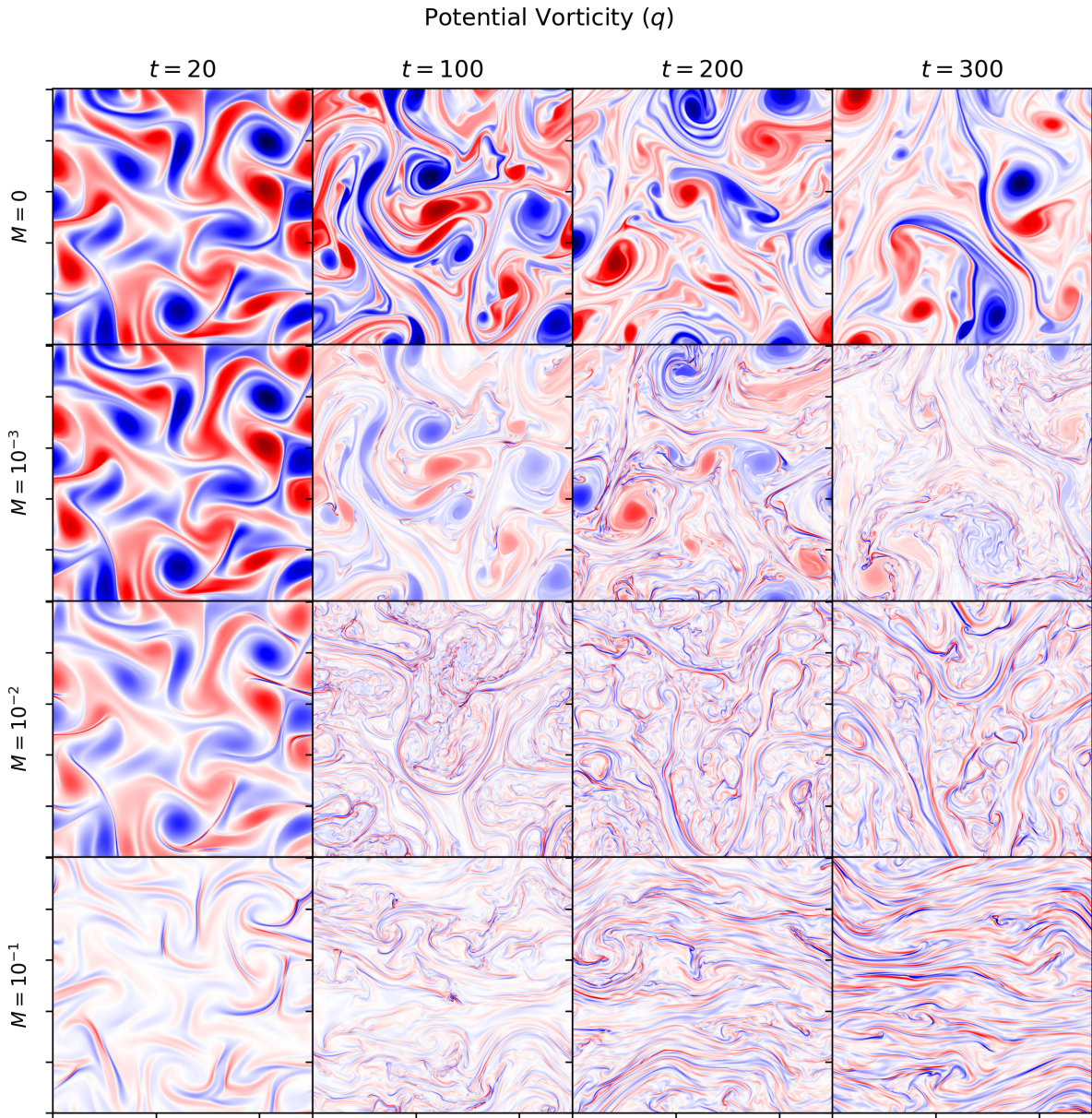
Figure 4.1: Snapshots of the PV for freely decaying turbulence in a rigid lid, for increasing $M = 0, 10^{-3}, 10^{-2}, 10^{-1}$ and at times $t = 20, 100, 200, 300$.

tendency in the evolution towards a similar regime regardless of the original configuration of the flow. These similarities include the generation of small scale filaments in the PV and their eventual alignment with the magnetic field for large enough M.

4.2   Free-Surface

Using the same initial streamfunctions, we now set $F = 1$ to move from a rigid lid regime to that of a weak free-surface in QG-MHD. The PV is shown in Figure 4.2 to compare with Figure 4.1 from the previous section. The same values of M and times are chosen. Recall that the presence of a free-surface inhibits the interaction of vortices at large scales and the dynamics become slower and more compact in space [72, 52, 98, 50, 75]. In our nondimensional model, using $F = L/R_d = 1$ suggests that motions at scales larger than 1 are inhibited. The consequent spatial compactness is evident in the first row of Figure 4.2 for the hydrodynamic regime and the vortices do not interact nor advect very much in the same time scale. Qualitatively, we see that increasing M from 0 to 10^{-3} provides similar behaviours as seen in the rigid lid case where small scale features are generated on the periphery of vortices. However, their relative amplitude is much smaller compared to the larger vortices in the flow. Increasing again to $M = 10^{-2}$ in the third row shows that PV filaments begin to dominate over the magnitude of the coherent cores. When $M = 10^{-1}$ in the last row, these filaments are long and rather smooth. However, in the last two rows, there is still evidence of rather large scale vortices left in the domain and we have yet to reach a full alignment of the flow with the field. The addition of the free-surface compared to the rigid lid has consequently inhibited the field-induced anisotropy, especially visible for $M = 10^{-1}$. For reference, these cases also have a large initial total PE of approximately 3 times its KE. This huge shift in the decomposition of the total energy makes it very easy to believe how different the flow now looks in comparison to the rigid lid (Figure 4.1).

4.3   Length Scales and Anisotropy

We will now compare the various diagnostics for the two sets of simulations above for different F. The microscales (2.77) of the flows considered above are shown in Figure 4.3. These try to approximate the length scales at which the bulk of the KE and ME are located. The left column depicts the microscale of the velocity as a function of time and the right column does the same for the ME. The top row corresponds to the case of a rigid lid and the bottom considers the free-surface evolution. The four different considered
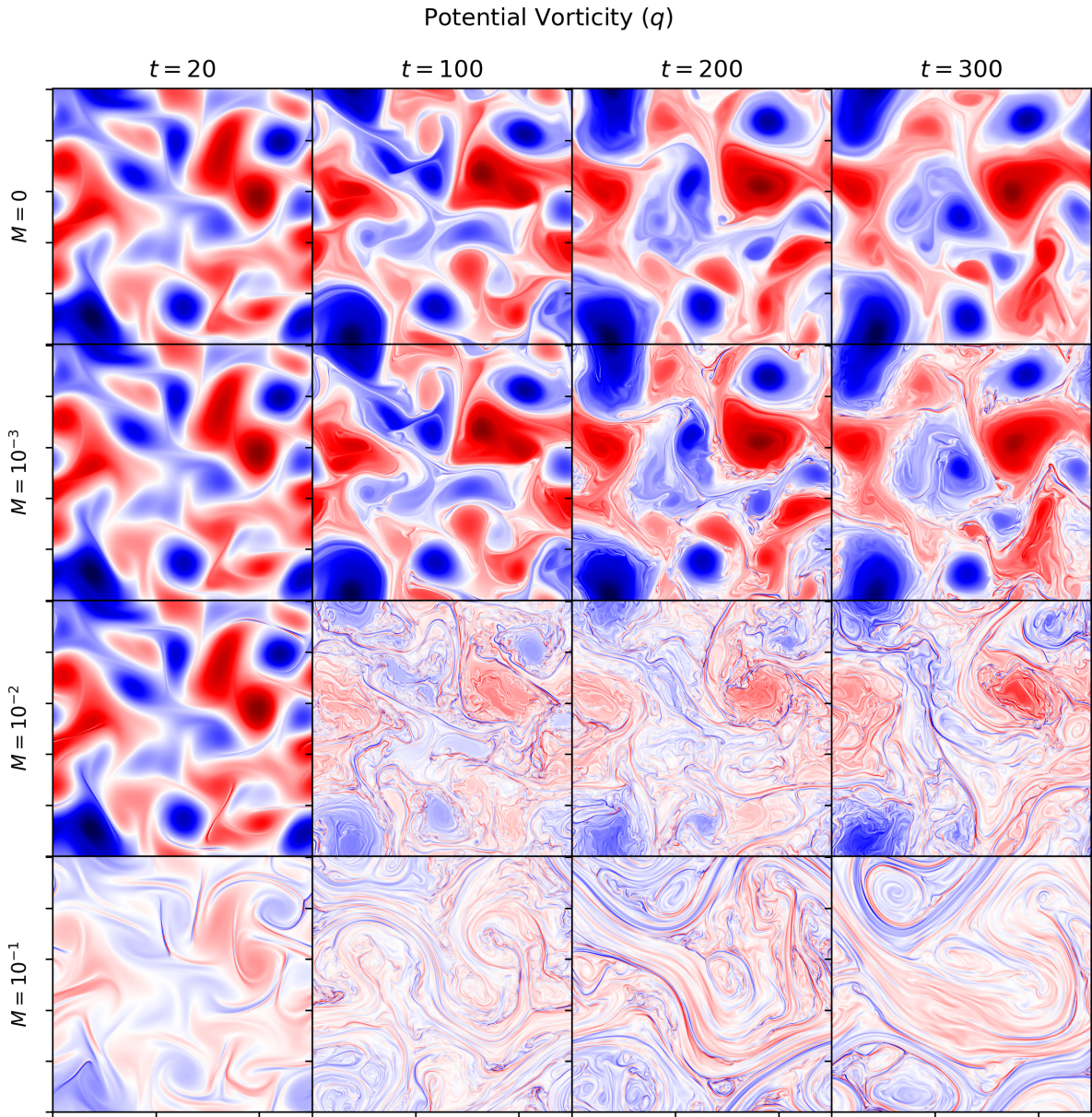
54

Figure 4.2: Snapshots of the PV for freely decaying turbulence with a free-surface ($F = 1$) for increasing $M = 0, 10^{-3}, 10^{-2}, 10^{-1}$ and at times $t = 20, 100, 200, 300$.

values of M are labelled as: 0 (solid black), 10^{-3} (dashed red), 10^{-2} (dot-dashed green) and 10^{-1} (dotted blue). In the top left, the black curve with $M = 0$ increases with time from $L_u \approx 1$ to 2 and the flow moves to larger length scales. In the same panel with $M = 10^{-3}$ (red dashed curve), this transition is halted and L_u starts to decrease with time after $t = 200$. A closer look at the top right panel shows that the microscales of the velocity and magnetic field depend on M in significantly ways, as we saw was the case in the last chapter. L_u moves to smaller scales for increasing M but the two strongest fields considered almost overlap each-other for all time. On the other hand, L_b (top-right panel) increases with M and time after the initial adjustment. Plotting L_u and L_b on the same y-axis allows us to observe that increasing M further correlates to a convergence of both L_u and L_b to very similar magnitudes near 0.3. Moving on to the next row when $F = 1$, we see that in the hydrodynamic case (black curve), the kinetic microscale L_u (top left panel) does increase but much less than in the rigid lid case. This is due to the influence of the free-surface which inhibits energy from moving to larger scales. The weak field case shows a decrease in the typical scale of the KE but the sharp transition seen in the rigid lid case is replaced by a smooth decay in scale. The general trend that L_u decreases with increasing M is retained. The analogous trend that L_b increases with M is also retained for $F = 1$. As was the case for the two by two vortex, the oscillations of these quantities over time are also suppressed.

A bulk measurement of the anisotropy is provided in Figure 4.4 for the norms described in (2.78). While the microscales showed at what scales most of the energy was located, these anisotropy norms show the direction in which these energies are most concentrated. The panels are arranged in the same way as in Figure 4.3 and correspond to the same simulations. With a rigid lid (top-right) we see that in the hydrodynamic case (black), the bulk velocity oscillates and ends up being more concentrated in the y-direction by the final time. The weak field case (dashed red) follows the same oscillation but ends up slightly more isotropic and the $M = 10^{-2}$ case (dot-dashed green) dampens the oscillation near $t = 150$. There is no consistent trend until we move to the $M = 10^{-1}$ curve (dotted blue) in which the flow steadily becomes more concentrated along the x-direction. This agrees with the alignment of the PV we saw in the bottom row of Figure 4.1. The alignment is also reflected in the magnetic field (top right panel) for the strongest case, but the other three curves of the magnetic field anisotropy overlap and decay to about 40% of the ME left in the x-direction. For these cases of turbulent ICs, the $M = 10^{-1}$ is an outlier in the anisotropy diagnostic where the flow clearly aligns with the field and more so over time. Possibly the most striking difference between the rigid lid (top) and free-surface (bottom) evolution appears in these anisotropy norms. When $F = 0$, we find that these norms vary significantly with different M and that for the strongest considered field, both the KE and
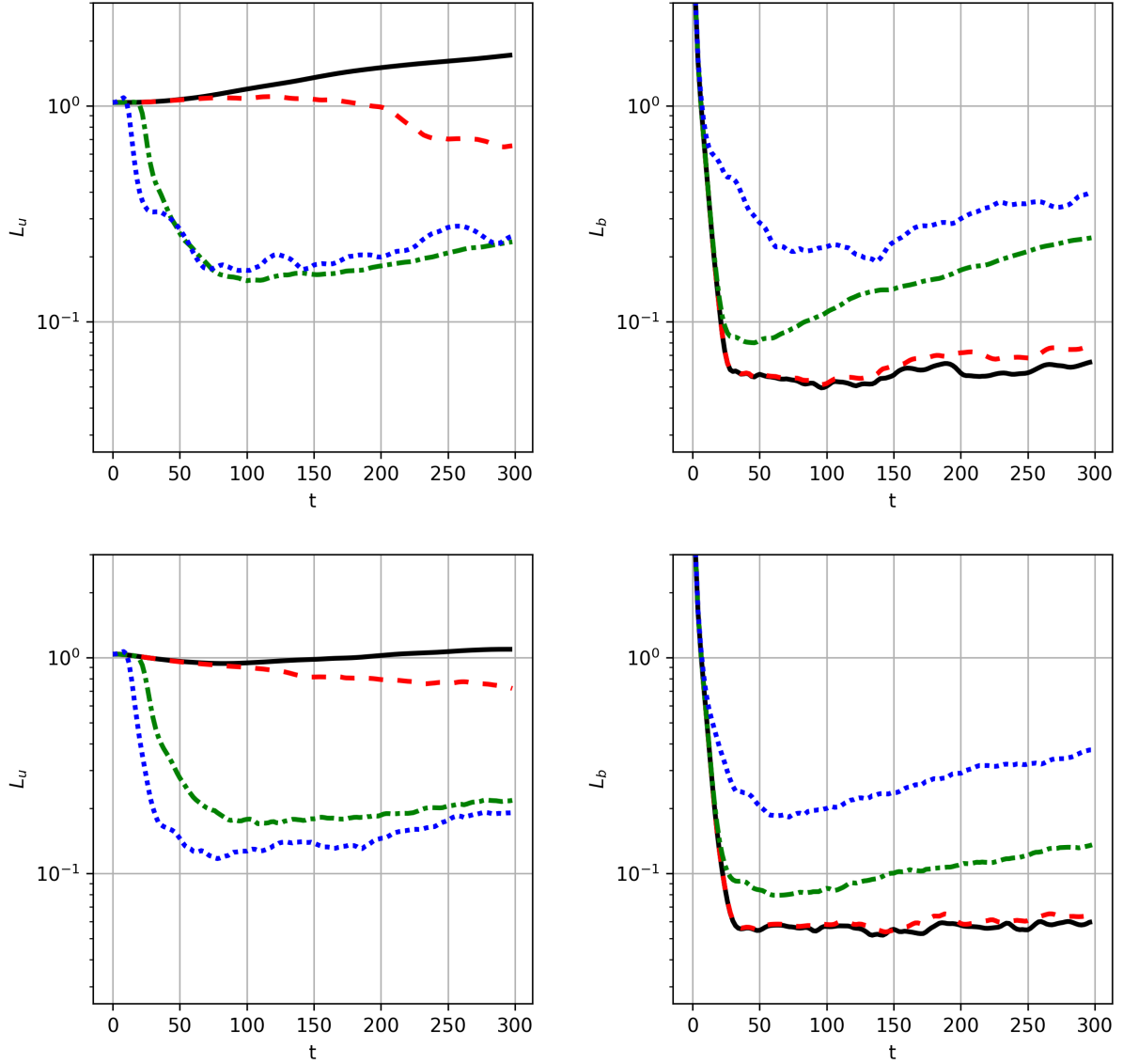
Figure 4.3: Kinetic (L_u, left) and magnetic (L_b, right) microscales (2.77) for decaying turbulence as a function of time, for four different values of M: 0 (solid black), 10^{-3} (dashed red), 10^{-2} (dot-dashed green) and 10^{-1} (dotted blue). The top row shows the rigid lid evolution with $F = 0$ while the bottom row shows the influence of a weak free-surface $F = 1$.

57

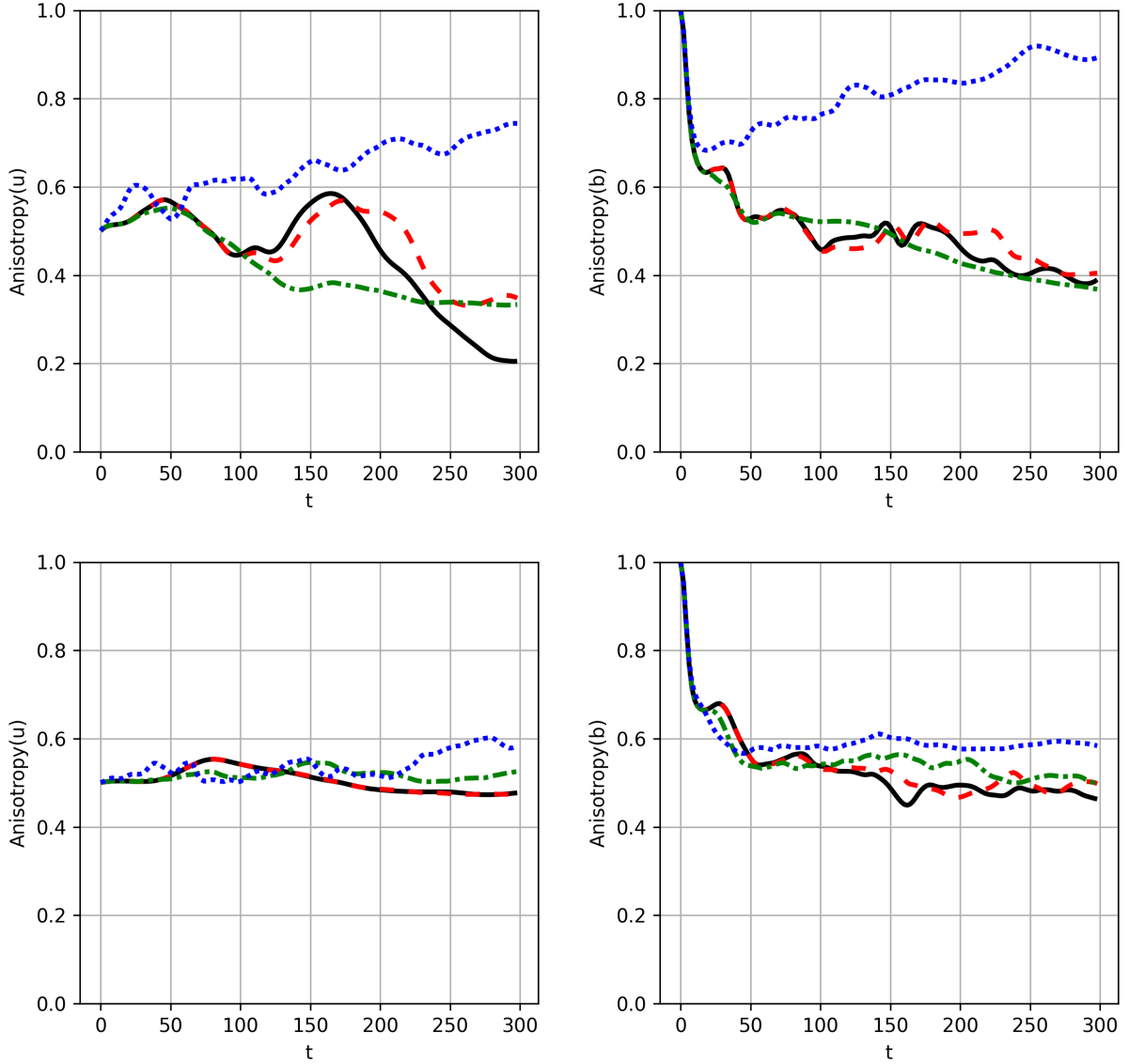Figure 4.4: Anisotropy norms for the velocity (left) and magnetic field (right) (2.78) for decaying turbulence as a function of time, for four different values of M: 0 (solid black), 10^{-3} (dashed red), 10^{-2} (dot-dashed green) and 10^{-1} (dotted blue). The top row shows the rigid lid evolution with $F = 0$ while the bottom row shows the influence of a weak free-surface $F = 1$.

ME were more concentrated along the direction of the background field. Now, with the influence of a free-surface, both the magnetic field and the velocity are very isotropic in the mean (within approximately 5%) apart from the strong field cases where the kinetic and magnetic energies are 60% in the x-direction.

4.4 Energy Spectra

In the study of turbulence, the literature often relies on the shape of the energy spectrum to quantify its dynamics. Thus, the azimuthally integrated kinetic (left) and magnetic (right) spectral energy densities are provided in Figure 4.5 as a function of the wavenumber in the same panel configuration and labelling as before. These are temporally averaged in $120 < t < 150$, corresponding to a time range between the center two columns of Figure 4.1. Our 2D turbulent simulations are decaying and no statistical equilibrium can be found without forcing at a particular scale. We thus chose a temporal range beyond the adjustment of the initial conditions and before the hydrodynamic spectrum became too steep. The associated spectral slopes are computed in the range of $6 < k < 10$. In the rigid lid configuration, the kinetic spectral energy density of the hydrodynamic case (black curve, top left) shows a slope of -3.5 slightly steeper than the -3 expected from the forward enstrophy cascade (the slightly steeper slope is unsurprising for numerical models). For increasing M, and even just with $M = 10^{-3}$, we see that the spectrum shallows indicating that more energy is contained at smaller length scales. This is very apparent form the rise of the tail in the spectrum near high wavenumbers for increasing M. The $M = 10^{-2}$ curve appears somewhat as an outlier though, where the computed slope is more shallow than the strongest case. We suspect this is due to the resulting evolution of the flow when $M = 10^{-1}$ which is hardly turbulent and dominated by bands of vorticity advected parallel to the field. The magnetic spectral energy density in the hydrodynamic case (black curve, top-right) is again associated with A being a passive scalar and really shows the spectrum scaled using a value of $M = 10^{-3}$ to compare with the weak field case[1]. It is clear that the ME spectrum changes very little from the hydrodynamic equivalent to the weak field case over all k and is mostly flat in the low to mid-wavenumbers. The stronger cases (green, blue) of $M = 10^{-2}, 10^{-1}$ for the magnetic spectral energy density show steeper and very similar spectra to each other with steeper slopes around -2. However, these curves are rather convex. They also differ in the small wavenumbers where the stronger field shows more magnetic spectral energy density at larger length scales.

---

[1]This spectrum is then that of the gradient of the passive scalar.
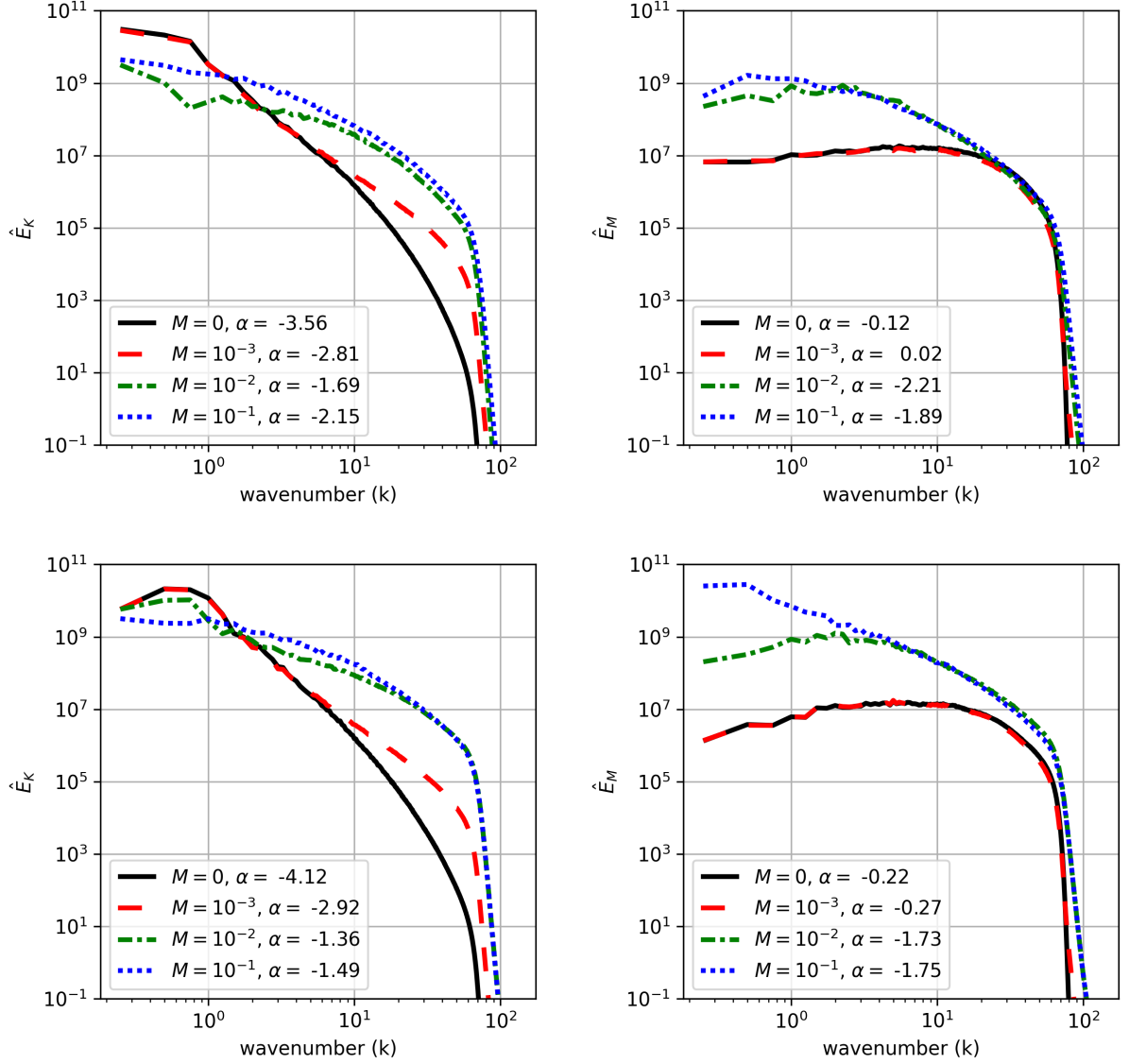
Figure 4.5: KE ($\hat{E}_V$, right) and ME ($\hat{E}_M$, left) spectra for decaying turbulence as a function of the wavenumber, for 4 different values of M: 0 (solid black), 10^{-3} (dashed red), 10^{-2} (dot-dashed green) and 10^{-1} (dotted blue). The top row shows the rigid lid evolution with $F = 0$ while the bottom row shows the influence of a weak free-surface $F = 1$. Spectral slopes α (for $E_{V,M} \sim k^{\alpha}$) are computed in the range $6 < k < 10$ and the spectra are temporally averaged in $120 < t < 150$.

60

The imposition of a free-surface in the bottom row of the same figure ($F = 1$) shows a mix of common features and differences with the top row. First, the kinetic spectral energy density of the hydrodynamic case (black curve, bottom left) shows a steeper range in the mid-wavenumbers where the slope is now closer to -4, but there is an additional accumulation of KE near $0.5 < k < 0.8$, in a rounded peak. The weak field case in the same panel retains this peak but otherwise looks similar in shape and slope to the rigid lid case. The two larger cases of M have smoother spectra and slightly shallower slopes still indicating more KE at smaller scales compared to the hydrodynamic evolution. Then, for the ME spectra (bottom right) the hydrodynamic and weak field cases are again virtually identical but now more convex, while the stronger cases show shallower slopes compared to a rigid lid. Again, the stronger field shows more ME in general and at larger length scales.

The Iroshnikov-Kraichnan phenomenology of MHD turbulence expects a -3/2 slope in the total energy spectrum. The argument for this slope is as follows: In the presence of large scale magnetic structures with field scale B (units of velocity), small scale fluctuations in the field behave like Alfvén waves. The interaction time between two counter-propagating waves (of mean wavenumber k) is then $\tau_B \sim (Bk)^{-1}$. The rate at which energy is transferred in the inertial range (equal to the energy dissipation rate ϵ in stationary turbulence) is proportional to τ and the proportionality factor is assumed to be only dependent on $\hat{E} = \hat{E}_K + \hat{E}_M$ and k (assuming a local cascade). Through dimensional analysis, we obtain [9]

$$\epsilon \propto \tau_B \hat{E}^2 k^4 \implies \hat{E} \propto (\epsilon B)^{1/2} k^{-3/2}. \tag{4.2}$$

However, this theory assumes equipartition of KE and ME in stationary and isotropic MHD turbulence (also with $M = 1$). Instead, we study the transition from a hydrodynamic regime (a slope in the KE close to -3) into a magnetic one, where the field has a background uniform component in one direction and the initial ME is always inferior to the initial KE. The slopes computed and discussed above are thus not a contradiction to the theory, but rather a depiction of how 2D hydrodynamics transition to a magnetic regime described by the Iroshnikov-Kraichnan phenomenology. We have considered an initial configuration of a random and isotropic magnetic field with this code in decaying MHD turbulence. We there readily confirmed the -3/2 law of the total energy but we do not include these results in this thesis.

4.5 Spectral Transfers

We now introduce the computation of the spectral energy transfers (2.62) and their respective fluxes. We opt to show the fluxes $\Pi_{q,L,A}$ instead of the transfers because $T_{q,L,A}$ are highly oscillatory and their integrals provide a clearer picture. We attempted the computation of the spectral energy transfers and fluxes in the same way that we did the energy spectra (in azimuthally integrating on the annulus of area $\pi(k^2 - (k + dk)^2)$ using the mean of the field on that annulus times the area). We found that doing so invalidated the conservative property of $T(k)$, where the total energy flux $\Pi(k)$ did not vanish at large k. To correct this, we resulted to summing the individual components on this annulus in lieu of our integration method[2]. In the absence of dissipation, energy conservation in spectral space requires that the double sum $\sum_{k_x} \sum_{k_y} T(k_x, k_y)$ vanishes, or equivalently that T is conservative. What we opted for here, is to simply sum the components of $T(k_x, k_y)$ which appear on the annulus of area $\pi(k^2 - (k + dk)^2)$ as the value of $T(k)$ to preserve energy conservation[3]. We confirmed that computing the energy spectra using either method gives the same answer and energy dissipation also does not change very much. These quantities however are of one sign (the spectra are positive and energy dissipation is purely negative). The main difference between the two methods occurs in $T(k)$, where its combination of sharp changes in sign at small k combined with very large amplitudes must be to blame.

Regardless, while the energy spectra (Figure 4.5) show the distribution of energy over a range of length scales, the spectral energy fluxes show how energy moves between length scales. We plot in Figure 4.6 the total spectral flux $\Pi(k)$ in the left column and the component due to the advection of the PV $\Pi_q(k)$ in the right column for the rigid lid case in the top row and for a free-surface in the bottom row. A negative value for a spectral flux corresponds to an upscale transfer of energy (to larger length scales) and a positive value shows a downscale transfer (to smaller length scales). In a rigid lid, the total flux Π (top-left panel) for the hydrodynamic case (black curve) shows a transfer of energy towards larger length scales (for $k < 1$). When $M = 0$, $\Pi = \Pi_q$ and so black curves on a same row are identical. When we increase $M = 10^{-3}$ (red-curve) however, we generate a downscale transfer in the mid-scales while also retaining the upscale transfer from the hydrodynamic case. The two larger values of $M = 10^{-2}, 10^{-1}$ show that the effects of magnetism dominate over the upscale transfer and Π becomes essentially positive, where the net energy transfer

---

[2]We confirmed that summing gave consistent results with the theory using a hydrodynamic turbulence case in which T_q, D_H are the only relevant quantities.

[3]The number of points on the annuli, $N_\circ(k)$ increases with k, and is computationally confirmed to be approximately $N_\circ(k) = Lk$, where L is the domain scale. This effective extra factor of k takes the placeholder of the polar Jabocian if we integrated azimuthally.
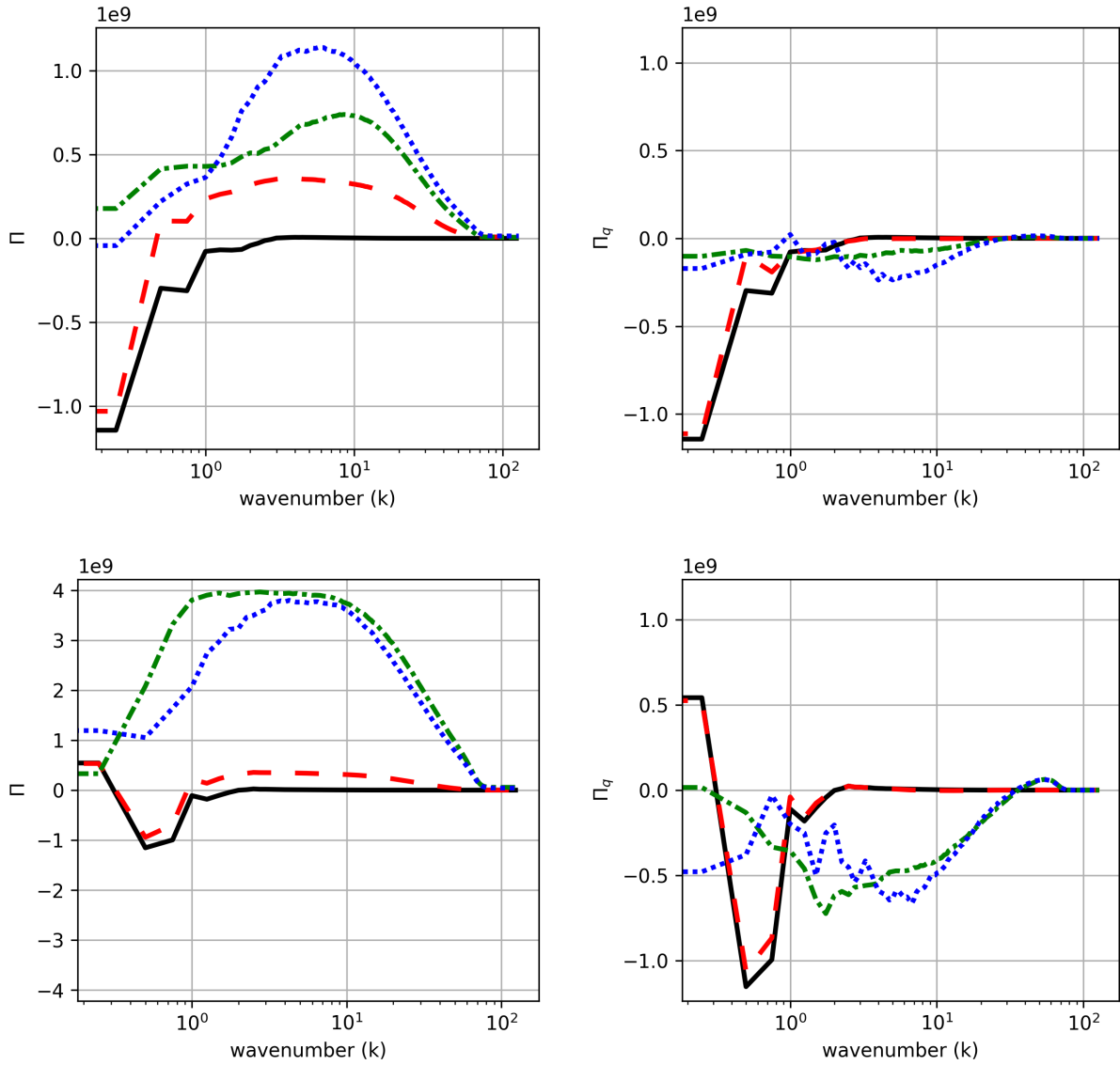
Figure 4.6: Total Spectral Energy Flux (Π, left) and only the PV advection component (Π_q, right) for decaying turbulence as a function of the wavenumber, for 4 different values of M: 0 (solid black), 10^{-3} (dashed red), 10^{-2} (dot-dashed green) and 10^{-1} (dotted blue). The top row shows the rigid lid evolution with $F = 0$ while the bottom row shows the influence of a weak free-surface $F = 1$. All quantities are temporally averaged in $120 < t < 150$.

63

is to smaller scales. The top-right panel shows that for increasing M, the contribution from the advection of the PV on the energy flux is decreasing in magnitude. For the two larger values of $M = 10^{-2}, 10^{-1}$, Π_q shows a region of weak upscale transfer in the low to mid-scales not previously seen in the hydrodynamic case (black curve). Since Π_q also vanishes at large k for all M, T_q appears to be individually conservative as well.

In the next row, we include the influence of a free-surface ($F = 1$). In the hydrodynamic case, we see the same upscale transfer from the row above in the larger scales ($0.3 < k < 1$) but now accompanied by a new region of downscale energy transfer at even smaller k towards $k \approx 0.3$ consistent with the idea that the free-surface inhibit vortex-interaction at larger scales. Such a zero in the plot of Π displays a convergence of energy flux towards this particular value of k from larger and smaller scales. The inclusion of a weak field ($M = 10^{-3}$) in the same panel displays again a downscale transfer in the mid-scales, but the larger values of M have amplified $\Pi(k)$ by a factor of about 4 (compared to the rigid lid) and has flattened it over a larger range in the mid-scales (especially when $M = 10^{-2}$, green curve). For Π_q in the bottom right panel with a free-surface, we see clear evidence of the downscale transfer at largest scales from the free-surface when $M = 0, 10^{-3}$. The upscale transfer in the mid-scales when $M = 10^{-2}, 10^{-1}$ is larger in amplitude compared to the rigid lid case and we developed a weak downscale transfer at very small scales for the same two values of M.

Figure 4.7 shows the components of the spectral flux due to the Lorentz force (left) and the advection of A (right) in a similar way. The black curves are associated with A being a passive tracer and do not contribute to Π in the previous plot since there is no ME when $M = 0$. These are included to compare with the weak field case (dashed red). In a rigid lid (top), Π_L shows that the Lorentz force induces a net downscale transfer of energy on the flow apart from the largest value of $M = 10^{-1}$ where a region of upscale transfer pushes energy towards $k \approx 20$ from either end. This suggests that magnetism has a preferred scale, dependent on M, reminiscient of the effects of a free-surface in a hydrodynamic evolution. We saw further evidence of this in the plotting of the microscales in the previous section. The contribution to the energy flux from the advection of the magnetic potential A generally compensates for that of the Lorentz force to provide an energy transfer in the opposite direction both in a rigid lid and in a free-surface. Since Π and Π_q in the previous figure vanish at large k for all considered M and F, it follows that the sum $\Pi_L + \Pi_A = \Pi - \Pi_q$ do as well. This effective cancellation is consistent with (2.19), where the Lorentz force and the advection of A cancelled exactly in the evolution of the total energy.

Finally, energy dissipation from viscosity D_H, and diffusion D_H (which are more coherent and less oscillatory than $T_{q,L,A}$) are shown in Figure 4.8. To be clear, these are
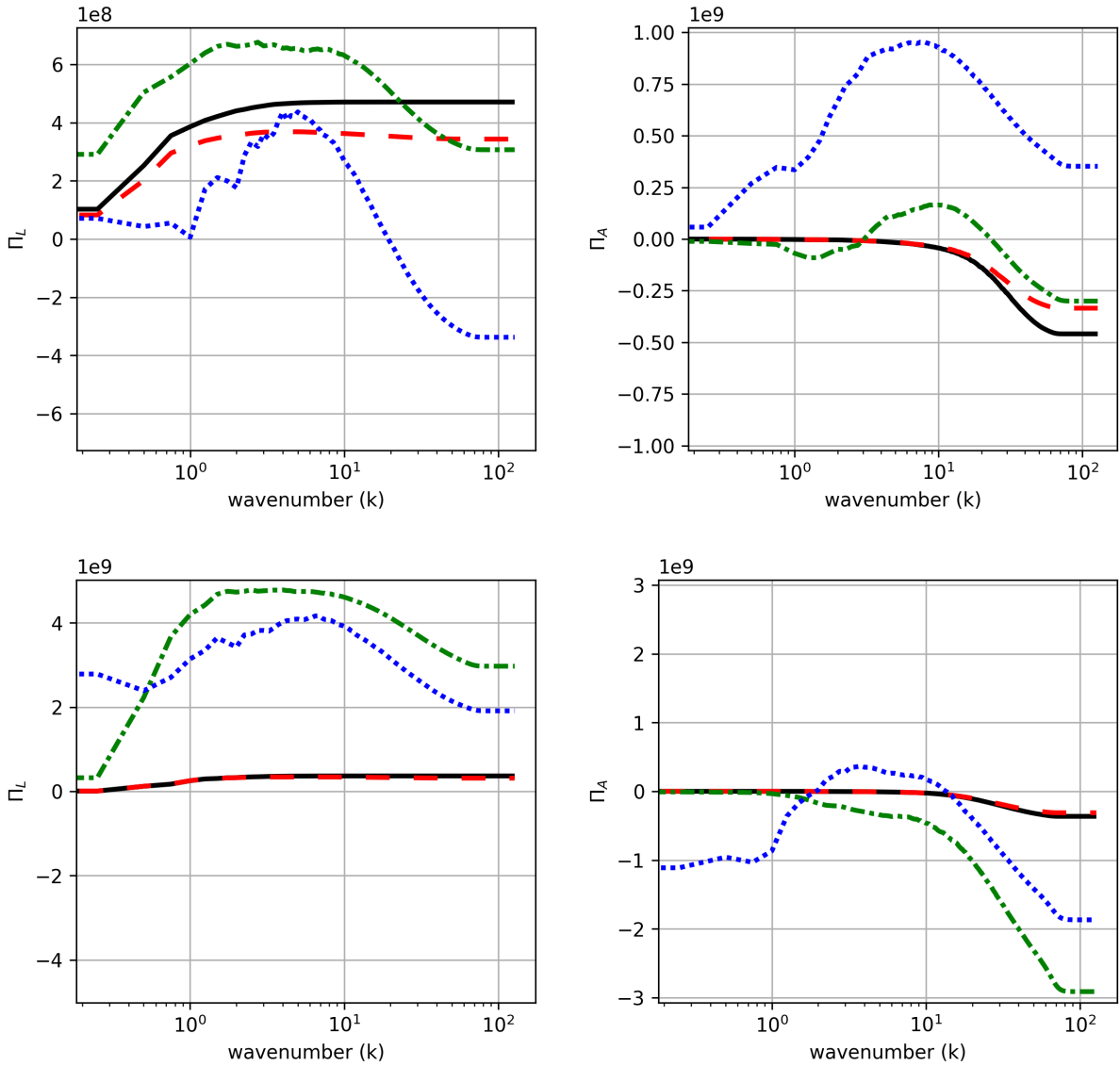
Figure 4.7: Spectral Energy Flux due to the Lorentz force (Π_L, left) and only due to the advection of A (Π_A, right) for decaying turbulence as a function of the wavenumber and for 4 different values of M: 0 (solid black), 10^{-3} (dashed red), 10^{-2} (dot-dashed green) and 10^{-1} (dotted blue). The top row shows the rigid lid evolution with $F = 0$ while the bottom row shows the influence of a weak free-surface $F = 1$. All quantities are temporally averaged in $120 < t < 150$.

65

not the viscous/diffusive equivalent of Π but rather those of T, which appear directly in (2.56) and (2.57). A positive transfer displays energy injection while a negative transfer corresponds to energy loss. Unsurprisingly, all curves in this figure are purely negative and take energy away from the system, as they should. They show an interesting transition between regimes, one of which we will refer to as hydrodynamic and the other a magnetic regime, for our four cases of M. The black and red curves (hydrodynamic and weak field cases) show that viscosity (top-right) dissipates energy the most near $0.5 < k < 0.8$ and diffusion (top-left) acts near $20 < k < 30$. This gap, slightly larger than a decade, is consistent with the same behaviour observed in the typical scales of the KE and ME in Figure 4.3. When M reaches 10^{-2} however in the green curves, the wavenumber where viscosity is most active jumps to near 10 (to smaller length scales) and the corresponding wavenumber for diffusion decreases towards the same value (to larger length scales). This convergence was also observed in L_u and L_b. This jump in scales is accompanied by a decrease in the amplitude of viscous dissipation and an increase in the amplitude of diffusion, consistent with the idea that we have more ME to deal with for larger M. We mentioned above a transition between a hydrodynamic and a magnetic regime since intermediate values of M for the rigid lid evolution (in particular $M = 3 \times 10^{-3}$, not depicted here) show that the way in which the red curve moves to the green curve ($M = 10^{-3}$ to 10^{-2}) in the plot of viscosity, is not by smoothly travelling to larger k (as diffusion seems to be doing) but rather a competition between two discrete ranges of k. We will see this competition explicitly with a weak free-surface. Again, the black curves in the D_M plots are associated with A a passive tracer.

Moving to the flow with $F = 1$ in the bottom row of Figure 4.8, the hydrodynamic and weak field cases of energy dissipation due to viscosity (black and red curves, bottom-right), have a slightly sharper peak still in the same range covering $0.5 < k < 0.8$. The next step in magnetism shows a slightly smaller peak in the same range but also the beginning of the transition from a hydrodynamic regime to a magnetic one, which had already complete in the rigid lid case for this value of M. In this case (green curve, bottom-left), the magnetic regime (the range of larger k and so smaller scales where energy is dissipated from the effects of magnetism) has approximately 15% the amplitude of the analogous peak in the hydrodynamic regime (at smaller k), in the same curve. This delay in transition shows that increasing F slows the dominance of the magnetic regime (where energy is dissipated at smaller length scales) over the hydrodynamic one. The strongest case (blue) shows a very wide tail in the small wavenumbers where there is significant loss of energy at all length scales smaller than $2\pi/10$ (for the peak at $k = 10$). In comparison, diffusion (right panel) is more similar to its rigid lid counterpart but the two stronger field cases have more than doubled in amplitude and the strongest case was a wider tail at small k.
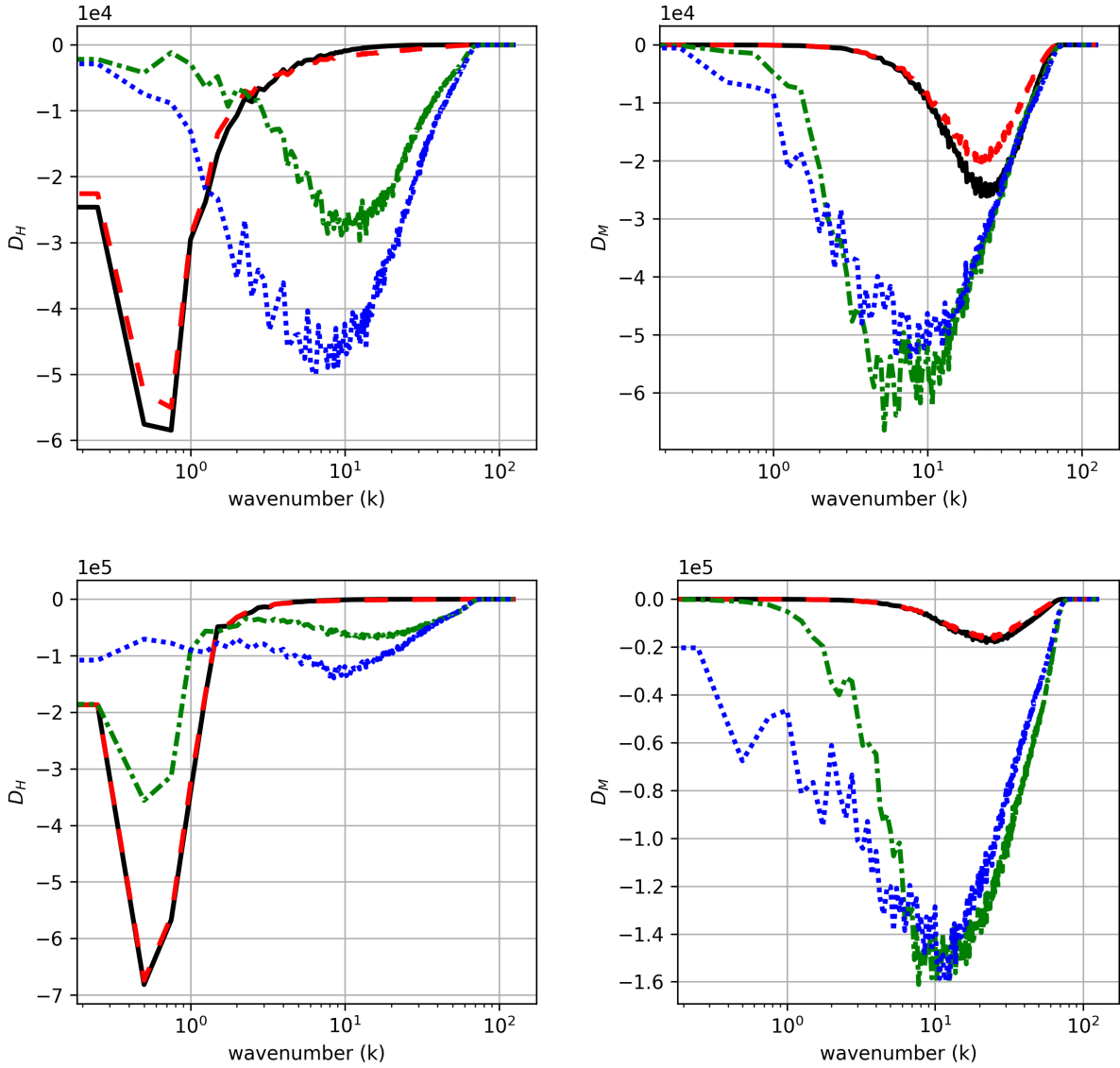
Figure 4.8: Energy dissipation from viscosity (D_H, left), and diffusion (D_M, right) for decaying turbulence as a function of the wavenumber for 4 different values of M: 0 (solid black), 10^{-3} (dashed red), 10^{-2} (dot-dashed green) and 10^{-1} (dotted blue). The top row shows the rigid lid evolution with $F = 0$ while the bottom row shows the influence of a weak free-surface $F = 1$. All quantities are temporally averaged in $120 < t < 150$.

Finally, let us summarize the main findings in the study of decaying 2D-MHD turbulence. As was expected from the theory of 2D-MHD, we found that increasing the magnetic field strength through M pushed more energy (and in particular more KE) at smaller length scales. This manifested in a consistent way throughout L_u, the energy spectrum, the spectral fluxes and energy dissipation. Our inclusion of the uniform background magnetic field pointing in the x-direction also introduced an anisotropy in the flow that was most visible in the strongest case of M considered. Including the effects of a weak free-surface, we confirmed that in the hydrodynamic case, the interaction between large scale vortices is inhibited when choosing F non-zero and the typical scale of the KE remained near one. We also found that the free-surface made the flow more isotropic in the mean, as it did with the vortex cases in the previous chapter. Increasing F further flattened the microscales in terms of suppressing the long-time oscillations in L_u, L_b and this was also apparent in the snapshots of the evolution, where vortices were more stationary and compact. For the energy fluxes, the weak field case showed that magnetic effects manifest by introducing a clear downscale transfer over a wide range in the mid-scales, which amplifies and dominates for the two largest values of M considered. Including a free-surface with magnetism showed the same behaviour but over a wider range of scales. For the two strongest cases of magnetism, the downscale transfer of energy from magnetic effects dominated over that of the free-surface. While the advection of the PV has very little downscale effects, the Lorentz force and the advection of A push energy to smaller scales while their combined effects $T_L + T_A$ remain conservative on the total energy, reminiscent of the cancellation of their respective terms in the derivation of the total energy evolution (2.26). For viscosity and diffusion, nonzero F delayed the switch from a hydrodynamic regime to a magnetic one, where the length scale at which energy is most dissipated due to viscosity moves to smaller scales, by a decade.

Chapter 5

The Stability of a MHD Bickley Jet

After having investigated MHD turbulence and in particular how energy is transferred between scales, we turn our attention to the study of shear instabilities. Specifically, we investigate the linear stability and nonlinear evolution of an unstable Bickley jet in the context of QG-MHD and compare the effects of a free-surface with that of a rigid lid for the same four values of the effective magnetic field strength, M. In this chapter, we restrict ourselves to $F = 1/2$ instead of the larger $F = 1$ (discussed in the previous chapters) when considering the effects of a weak free-surface in the nonlinear evolution. The parameter is found to be stabilizing enough that $F = 1$ decreases the growth rate approximately five-fold compared to the $F = 0$ case in the hydrodynamic limit. Our choice of $F = 1/2$ in this chapter is sufficiently large to demonstrate the nonlinear effects of a free-surface without sacrificing computing time. The MHD jet we focus on is a stationary solution to the system (2.4) and is defined as (in the formalism of 2.66)

$$U(y) = \mathrm{sech}^2(y - L_y/2), \quad \Psi(y) = -\tanh(y - L_y/2), \quad B(y) = 1, \quad \bar{A} = -y \qquad (5.1)$$

The associated PV field is computed via: $\bar{Q}(y) = \partial_{yy}\Psi - F\Psi$. We shall first present the results of the LSA and then study the nonlinear evolution in a similar fashion to what was done for freely-decaying turbulence.

5.1   Linear Stability Analysis

We solve system (2.74) for the unstable MHD Bickley jet in a parallel background magnetic field (5.1). We show in Figure 5.1 the individual contributions of the nondimensional
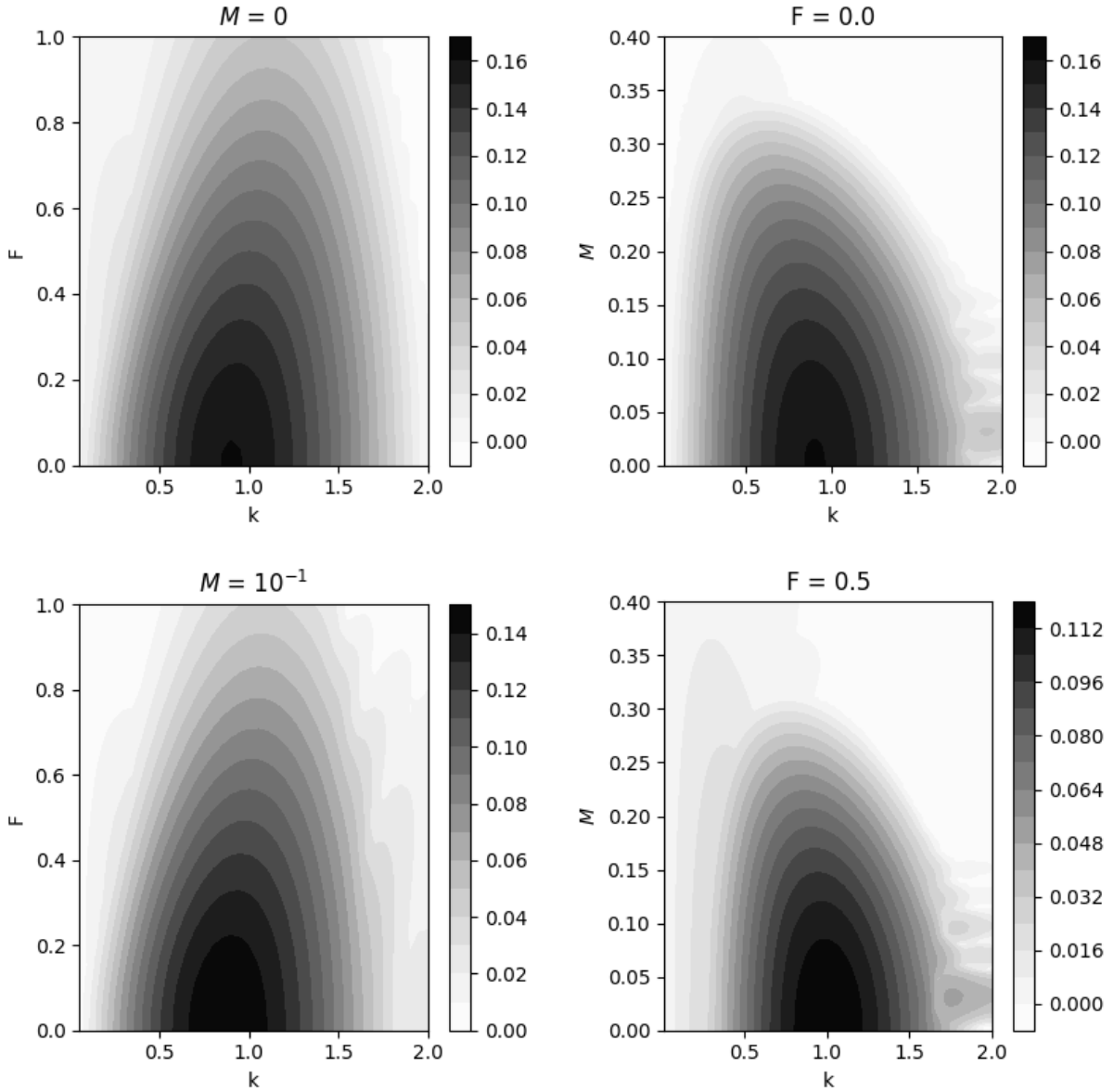
Figure 5.1: Contour plots of the growth rate of the largest growing mode for the unstable Bickley jet as a function of the wavenumber k and of F, with M fixed at 0 (top-left) and 0.1 (bottom-left), and as a function of the wavenumber k and M with F fixed at 0 (top-right) and 1/2 (bottom-right) respectively. Both parameters are stabilizing.

quantities, F and M, on the stability of the jet by depicting the maximum growth rate over a range of wavenumbers. Recall these parameters respectively control the influence of the free-surface and the relative strength of the background magnetic field. The growth rates determine how fast the perturbation grows exponentially in time. The system (2.74) is solved for a fixed vector of wavenumbers $k \in [0, 2]$ and for $F \in [0, 1]$, with M fixed at (top-left) 0 and (bottom-left) 0.1, and again as a function of the wavenumber k and now $M \in [0, 0.4]$ with F fixed at (top-right) 0 and (bottom-right) 1/2 respectively. Recall that the effective magnetic field strength M and the rotational Froude number F are individually (with the other parameter held at zero) stabilizing to jets [73, 56]. Figure 5.1 confirms this to be the case where the growth rate of the most unstable mode decreases with both M and F in the first row. The same plots also show that both parameters are stabilizing in different ways as the most unstable mode transitions to different length scales. For the case of no magnetism and increasing influence from the free-surface (top-left), the largest growing mode is moving to larger k (or smaller length scales in the x-direction). In contrast, for the case of a rigid lid and increasing influence from the background magnetic field (top-right), the largest growing mode moves to larger length scales in the x-direction. The bottom row shows that with non-zero values of the other parameter, the behaviour is the same and the nondimensional parameters are still stabilizing in the presence of the other. The maximum growth rate in the bottom row (non-zero value of the other parameter) is smaller than in the top row, indicating that the effective stabilization of both M and F compound on the evolution of the jet. We suspect the sharper features in the bottom-right corners of the right column panels are due to numerical error.

We chose to keep the same domain size $L_y = L_x = 8\pi$ as the previous chapters for all considered values of F and M in the nonlinear simulations. Of course, this means that the largest growing mode from the theory may not fit an integer number times in the domain length (the x-direction). To provide a fair comparison between the theory and the nonlinear simulations, we used the predicted growth rate of the mode fitting exactly three periods in the domain. This is the mode that was shown to grow the fastest in the nonlinear simulations (a posteriori). This mode corresponds to wavenumber $k = 3/4$ in system (2.74), close to the most unstable wavenumber at or just below $k = 1$ from Figure 5.1. A modal wavenumber of 1/4 would fit one period, wavenumber 1/2 would fit two and so on, given our domain length. We further include a depiction of the spatial structure of the most unstable modes for selected $F = 0, 0.5, 1$, and $M = 0, 0.1, 0.2$ at $k = 3/4$ in Figure 5.2. The PV is plotted on the same domain as the nonlinear simulations for comparison and the growth rates ω_I and phase speeds ω_R are also included in each panel for reference. In the first row for the hydrodynamic limit, the inclusion of the free-surface and the increase in F has a subtle effect on the PV where it tends to sharpen the features on the flanks of
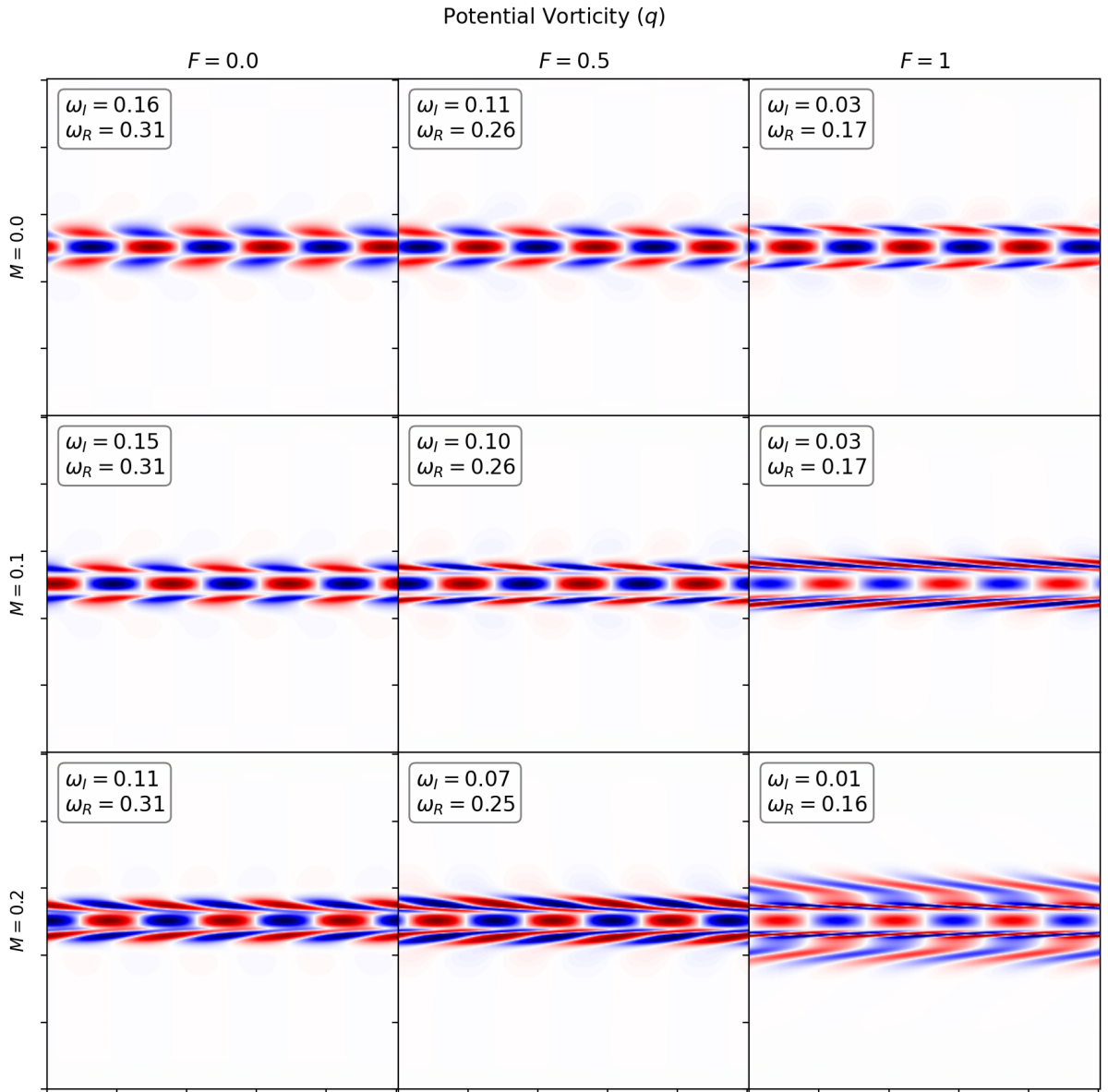
Potential Vorticity (q)

Figure 5.2: Spatial structure of the PV for the largest growing mode of the unstable Bickley jet when $F = 0, 0.5, 1$, and $M = 0, 0.1, 0.2$. The growth rate is given by ω_I and ω_R is the phase speed.

the jet, while having little effect along its axis. Given the spatial structure and what we know from the established literature, we can refer to this mode as a sinuous one where the streamfunction is even about the jet axis. Unstable modes with odd streamfunctions on the other hand are called varicose modes [61]. With $M = 0.1$ in the next row, the PV for the rigid lid case ($F = 0$) has changed slightly from the case above it, where the features on the flanks are subtly compressed and elongated in the x-direction. With this $M = 0.1$, the next column when $F = 0.5$ (center panel) shows a more pronounced sharpening, but finally when $F = 1$ the flanks are very long and thin. In the next row, for a higher value of $M = 0.2$, we still see a pronounced stretching of PV on either flank and increasing F up to one now actually created features further away from the flanks while leaving strong and thin PV filaments close to the axis. The bottom row and right column showcase some extreme cases of high F and M and their effect on the jet. However, since sufficiently different dynamics occur for $F = 0, 0.5$ and $M < 0.1$ in the nonlinear evolution, we omit these extreme cases there.

The growth rates from the nonlinear simulations were computed using the 2-norm of the perturbation streamfunction, $||\psi'|| = ||\psi - \Psi||$, which appears directly in the linear stability problem (2.74). Recall the modal decomposition (2.72) where $\psi' = \hat{\psi} \exp(ikx) \exp(-i\omega t))$. The growth rate is the imaginary part of ω, ω_I and determines how fast the solution grows exponentially in time, $||\psi'|| \propto \exp(\Im(\omega)t)$. Regions of exponential growth (and therefore temporal ranges in which the linear stability theory applies) are easily picked out as linear segments on a log-scaled graph of $||q'||$. For the considered parameters, this temporal range typically included $20 < t < 40$. In such a plot, the line of best fit can be computed over a small range of times (4 time units in our case) where its slope corresponds to the growth rate of the instability, since $\ln(||q'||) \propto \omega_I t$. Individual data points were considered to compare linear theory with nonlinear evolution. We used 4 cases shown in the top-left of Figure 5.2, namely the combinations of $M = 0, 0.1$ with $F = 0, 1/2$ and found that the computed growth rates differ from those predicted by linear theory (at $k = 3/4$) at most by approximately 7 % (relative error). The associated spatial structures of the modes also agreed very well. We have good agreement between theory and numerical simulation where we expect the remaining discrepancy to be due to numerical error. We now move to the nonlinear regime in studying the effects of magnetism and non-zero F.

5.2 Rigid Lid Simulations

We begin our nonlinear study of MHD Bickley jets by isolating the effects of magnetism in a rigid lid framework ($F = 0$) and we again plot the PV field, q. We use the same

random field generator from our study of turbulence to create the perturbation velocity and magnetic fields at 1% of the amplitude of the background quantities. The spectral width and typical wavenumber for the perturbation are $\sigma = 2$, and $k_t = 0$. Snapshots of the perturbation PV field are provided in Figure 5.3 for $M = 0, 10^{-3}, 10^{-2}, 10^{-1}$ and at times $t = 20, 50, 100, 150$. In the first column at $t = 20$, we observe the structure of the unstable mode, well in agreement with what is predicted by linear theory in Figure 5.2. The first three cases of $M = 0, 10^{-3}, 10^{-2}$ show very little change and approximately three periods of the mode in the x-domain. For the largest M however (bottom left), we see that the structure has changed. The bulk of the mode is similar (near the axis) but the vortical features on either flank of the jet have been stretched out and thinned in the x-direction.

In the next column ($t = 50$), we have left the linear regime and again the first three rows are rather similar, where the unstable mode has given rise to vortices. Since we plotted the perturbation PV, we see the negative imprint of the background q where the jet used to be. In these cases, the amplitude of q' and $\bar{Q}$ are similar given the color-scale, and $q' \sim \bar{Q} \sim \mathcal{O}(1)$. The strongest case in the second column (bottom row) shows that a stronger magnetic field generates large amplitude filaments of PV (with $q' \sim \mathcal{O}(10)$), that dominate the field in comparison to the vortices seen in the three cases above it. This behaviour reminds us of the early-time evolution for a row of vortices from Chapter 3 in Figure 3.3. At the next time ($t = 100$), only the first two rows are similar and the presence of magnetism has been felt in the third row for $M = 10^{-2}$. Recall that this is the case of magnetism satisfying the vortex disruption criterion and so this behaviour is expected. Secondary instabilities of smaller length scales are generated on the periphery of the vortices. The resulting filaments have started to dominate the evolution and to destroy the coherence of the remaining cores. For $M = 10^{-1}$, this time shows very little evidence that coherent vortices remain and the bulk of the PV amplitude is concentrated along thin filaments located near the jet axis. A brief outline of vortical features protruding away from the jet axis (above and below) however show the remainder of the vortices generated by the instability. Finally at the last time $t = 150$, we start seeing the difference between the hydrodynamic and very weak field ($M = 10^{-3}$) evolution in the first two rows, where filaments of PV surrounding coherent cores begin to amplify. The $M = 10^{-2}$ case now shows an aesthetically pleasing array of rather turbulent (small scale) features and the amplitude of q' has decreased from the previous time. The $M = 10^{-1}$ case on the other hand has organized the filaments of PV in the x-direction due to the strong effects of magnetism.

Mak et al. 2017 [57] considered a 2D-MHD Bickley jet in their investigation of the vortex disruption criterion. They however considered a smaller $R_e = 500$ and $R_m \in [50, 1000]$ along with a range of $M \in [0.005, 0.05]$. In comparison, recall we have $R_e = R_m = 10^4$

Potential Vorticity (q)

$t = 20$ $t = 50$ $t = 100$ $t = 150$

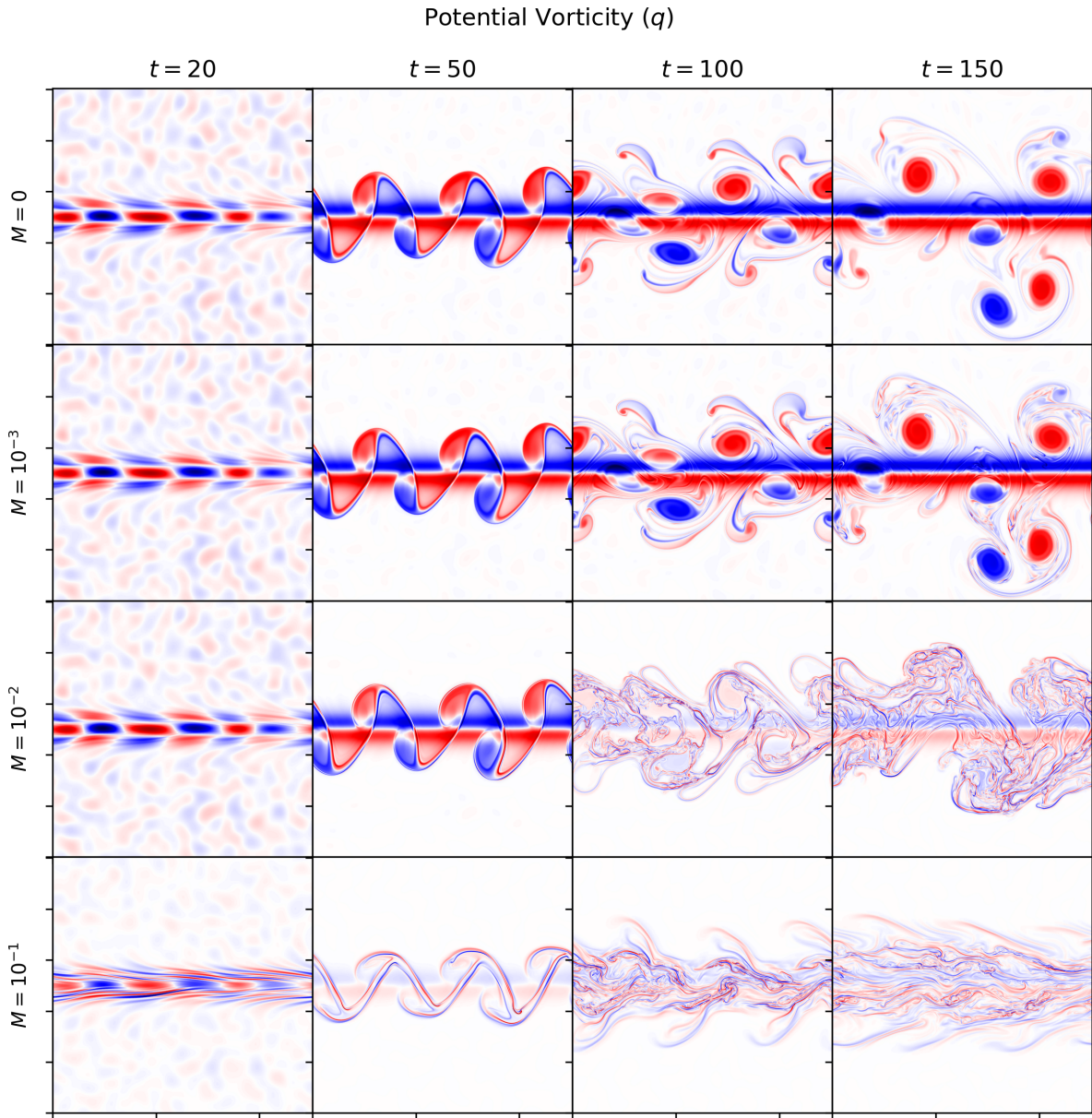$M = 0$ $M = 10^{-3}$ $M = 10^{-2}$ $M = 10^{-1}$

Figure 5.3: Snapshots of the perturbation PV for the (rigid lid) unstable Bickley jet for increasing $M = 0, 10^{-3}, 10^{-2}, 10^{-1}$ and at times $t = 20, 50, 100, 200$.

and $M \in [0, 0.1]$. Our higher choice of Reynolds numbers generates smaller scale features in comparison and our wider range of M also includes a stronger field regime and new resulting dynamics. Given our four points in M and the selected times, Figure 5.3 can be summarized by the following observations: i) The structure of the most unstable mode is similar for $M = 0 - 10^{-2}$ but small scale filaments of PV arise on the jet flanks when $M = 10^{-1}$. ii) Immediately beyond the temporal range where linear theory still applies, the filaments of PV when $M = 10^{-1}$ dominate the evolution whereas the other cases are similar to a hydrodynamic evolution. iii) Far into the nonlinear regime, vortex disruption occurs when $M = 10^{-2}$, well in agreement with the vortex disruption criterion $R_m M^2 \sim \mathcal{O}(1)$ [57]. iv) Magnetic effects start to manifest only after very long time for a weak field of $M = 10^{-3}$. v) The strong field case displays organisation of vortical filaments in the same direction as the field. Thus, we see many parallels in the evolution of the jet when compared to the evolution of vortices considered in Chapter 3 and the turbulence in Chapter 4. These include the consistent vortex disruption regime, small scale filaments of the PV, and the eventual alignment of the flow with the field.

5.3   Free-Surface Simulations

After seeing the qualitative behaviours of the rigid lid case for increasing magnetism, we now move on to non-zero contributions from the rotational Froude number in a QG-MHD regime. Recall we pick $F = 1/2$ in this section and consider then same values of M considered above. Poulin & Flierl 2003 [73] found that F is stabilizing on shallow jets with compacting effects on the instability. Flierl et al. 1987 [30] found that a barotropic beta plane is also stabilizing, with similar compacting of the jet towards its axis. This behaviour is quite clearly shown in the PV plotted in Figure 5.4. The first row is hydrodynamic and the instability gives rise to vortices that remain in close proximity to the jet flanks even after long time, in agreement with the expected compacting effects of F. The inclusion of the weak magnetic field ($M = 10^{-3}$) in the next row shows very little change for the entire simulation. For $M = 10^{-2}$ in the third row, the early evolution is similar to the hydrodynamic and weak field cases. However when $t = 100$, the periphery of the generated vortices yield thin and large amplitude filaments of PV. These become unstable and give rise to secondary instabilities which begin to dominate the field by the final time. Notice that even with the small scale features generated from magnetism, the extend of the motion in the y-direction is more localized near the jet axis compared to the rigid lid evolution. Finally, for the largest case of magnetism ($M = 10^{-1}$) in the last row, the early evolution shows the same thin filaments around the most unstable mode. However, this evolution is
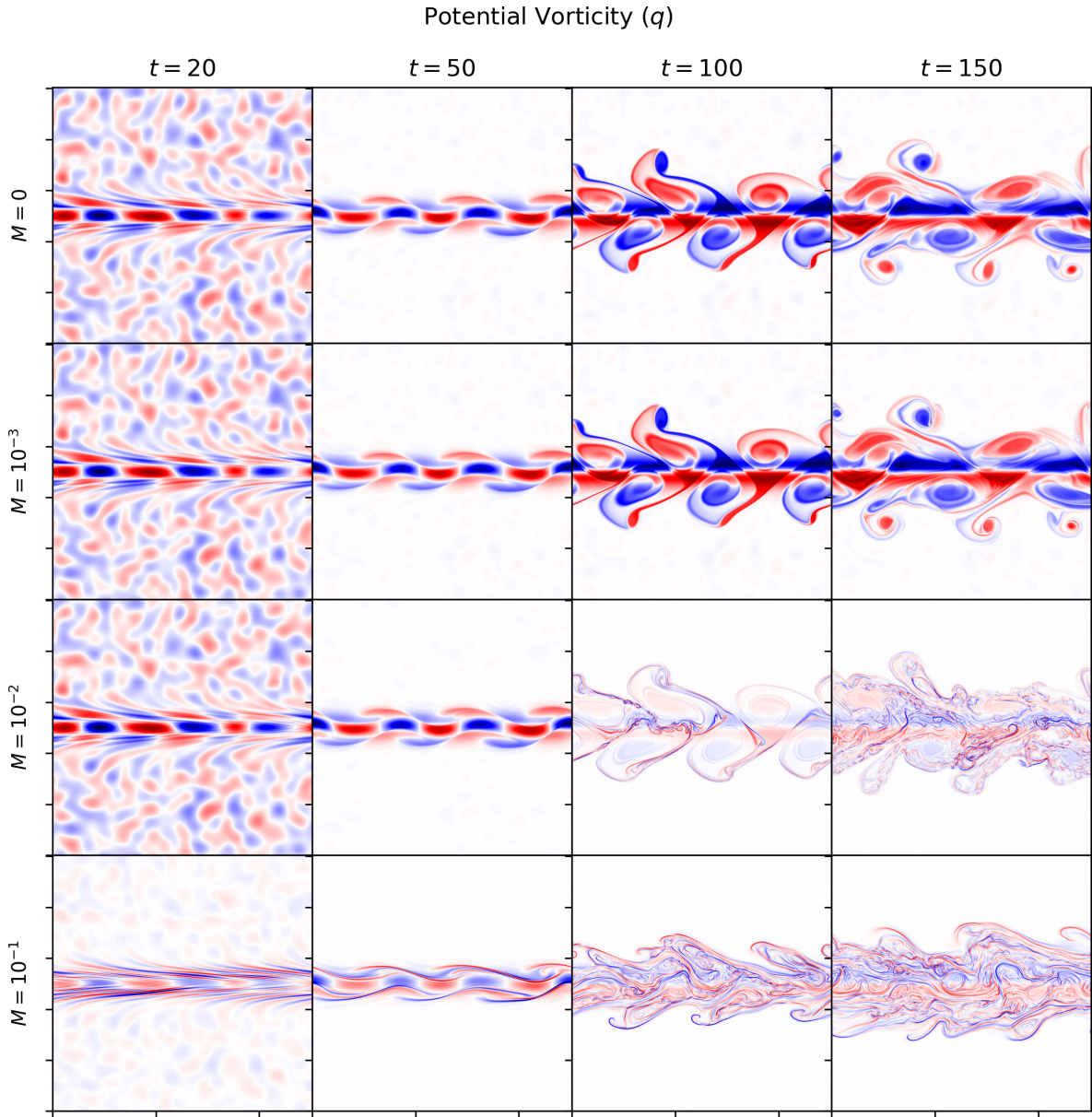
Potential Vorticity (q)

Figure 5.4: Snapshots of the perturbation PV for the unstable Bickley jet in a weak free-surface ($F = 1/2$) for increasing $M = 0, 10^{-3}, 10^{-2}, 10^{-1}$ and at times $t = 20, 50, 100, 200$.

more similar to the $M = 10^{-2}$ rigid lid case (third row), providing PV filaments which are not aligning with the field as quickly as before. These figures provide further evidence that the effects of a free-surface and those of magnetism qualitatively combine, where the surface has a spatially compacting effect on the flow (as seen in hydrodynamics) and magnetism generates small scale features with a tendency to align the flow with a strong field. The aforementioned figures give us a nice depiction of the evolution and we now move on to the relevant diagnostics to provide quantitative support in our observations.

5.4   Length Scales and Anisotropy

In this section we present the typical length scales (2.77), and anisotropy norms (2.78) for the velocity and magnetic field. The scales are included in Figure 5.5 and are computed using the full field (including both the background and perturbation components). Keeping the same theme from the previous chapters, the different values of M are shown as 0 (solid black), 10^{-3} (dashed red), 10^{-2} (dot-dashed green) and 10^{-1} (dotted blue). The plots have been cropped to the same vertical bounds allowing for a better comparison between the kinetic and magnetic counterparts. The top bound is still picked to contain the largest value of L_u while the bottom bound is the grid-scale.

Starting in the top left with L_u in a rigid lid, the initial value is approximately 1 and displays the length scale of the jet. The black (hydrodynamic) and red ($M = 10^{-3}$) curves are essentially superimposed for the displayed temporal range and show an increase (though slight) in the typical length scale of the velocity. This is consistent with our results of hydrodynamic turbulence, where the vortices generated by the instability interact and combine. The weakest strength of $M = 10^{-3}$ has yet to disrupt this increase but the length scale is slightly smaller than the hydrodynamic case. For the other two curves, we see significant drops in L_u (by almost an order of magnitude). The highest strength of magnetism ($M = 10^{-1}$, dotted blue) shows this dip first near $t = 30$ and the $M = 10^{-2}$ (dot-dashed green) case shows this to start happening near $t = 60$. After $t = 100$ however, these two stronger cases show very similar length scales and the green curve is more consistently increasing while the blue shows some oscillatory behaviour thereafter. An increase in M therefore correlates with a decrease in L_u and the strongest field shows this sharp transition to occur at earlier times. While both the stronger cases of magnetism ($M = 10^{-2}, 10^{-1}$) leave the linear regime of evolution at similar t, the time needed for the Lorentz force to act on the generated vortices is shortened for the stronger field and smaller scale features are more quickly created.

Now for the magnetic analogue in the top right corner of the same Figure 5.5, of course
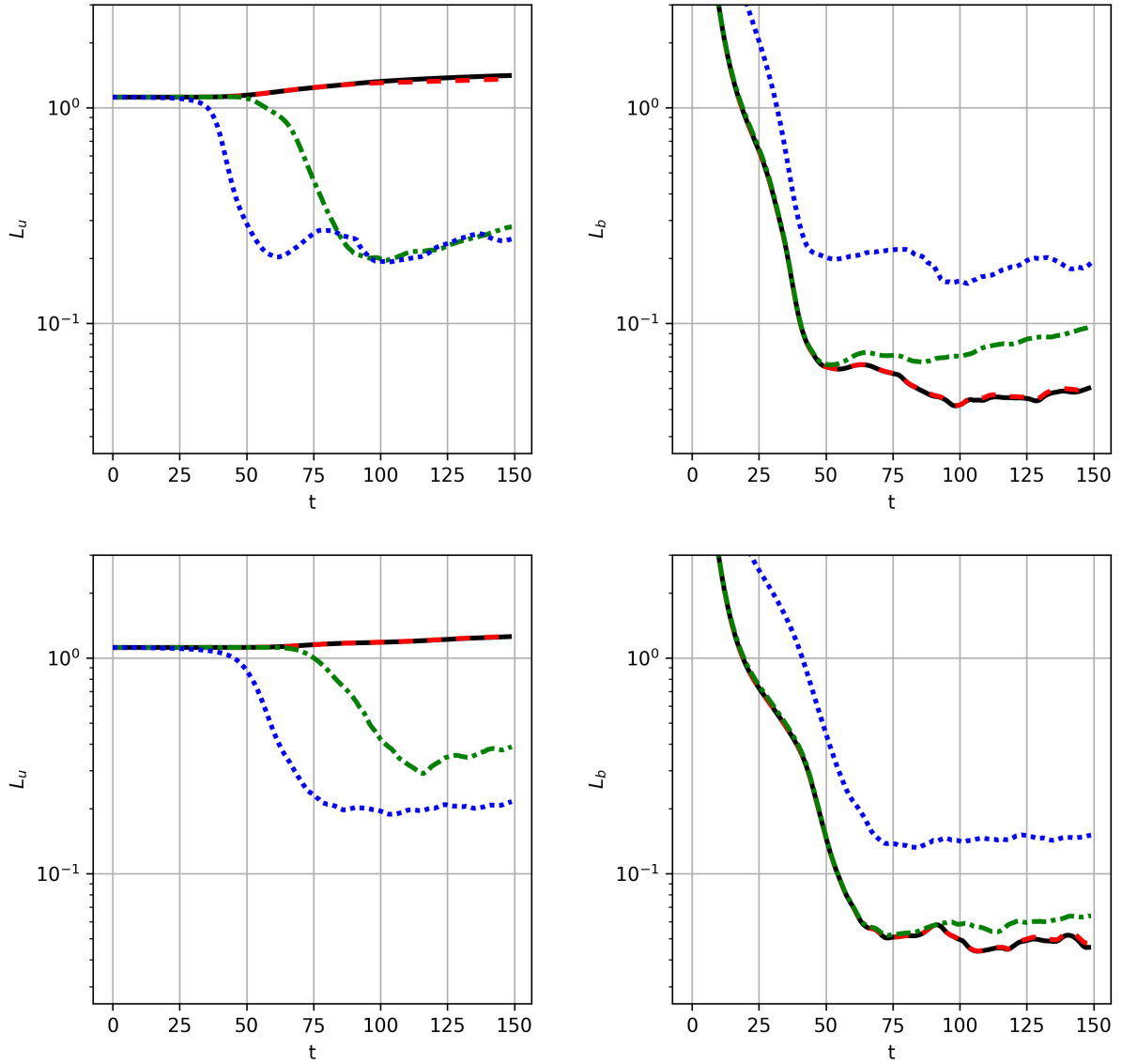
Figure 5.5: Kinetic (L_u, left) and magnetic (L_b, right) microscales (2.77) for the rigid lid (top) and free-surface (bottom) Bickley jet as a function of time for four different values of M: 0 (solid black), 10^{-3} (dashed red), 10^{-2} (dot-dashed green) and 10^{-1} (dotted blue).

the initial scale L_b is large in all cases given that the field is initially uniform. It is evident however that L_u and L_b are still affected in different ways in varying M given that L_b tends to increase with increasing M. After the initial adjustment near $t = 50$, the hydrodynamic and weak field cases lead L_b closer to the grid scale while the $M = 10^{-2}$ (dot-dashed green) case rises to larger length scales. The strong field case is isolated further away at larger scales still and displays some oscillations rather than a consistent rise. These oscillations roughly match up with the respective ones seen in L_u. Having plotted L_u and L_b on the same vertical scale is useful for comparing their respective amplitudes. While L_u typically decreases and L_b increases for increasing M, our largest $M = 10^{-1}$ field case seems to have let both converge to the similar value, where L_u L_b. This shows that for strong enough magnetic field, the length scales of $\mathbf{u}$ and $\mathbf{b}$ can become similar.

For the bottom row of the same figure with a free-surface, the hydrodynamic increase in the typical length scale of the velocity (black curve, bottom left) is very slightly dampened compared to the rigid lid analogue. The other two values of M show a consistent decrease of L_u and there is greater separation between the green and blue curves. The plots of L_b in the bottom right panel show similar qualitative features to the rigid lid case where there is an initial drop in the length scale, but this adjustment now take $20 - 25$ time units longer to settle down. The resulting evolution is relatively free of oscillations, especially in the strong field case. In comparison to the turbulent length scales from the previous chapter, most of the variation we see in L_u happens after the jet has become unstable and has left its stationary evolution. The general behaviour however is the same, where L_u decreases with M, L_b increases with M (after the initial adjustment) and F dampens energy transfer to large scales and long time oscillations in the microscales.

The norm of the anisotropy in the velocity and the magnetic field are shown in Figure 5.6, for the case of a rigid lid on top and the case of a free-surface on the bottom. Since both the initial $\mathbf{u}$ and $\mathbf{b}$ are in the x-direction given (5.1), both norms display values of 1 at $t = 0$, reflecting that the KE and the ME are aligned with the x-axis. The qualitative behaviour in both top panels is similar, where the hydrodynamic and weak field cases reach a regime of bulk isotropy by the final time (a value close to $1/2$) after some oscillations. For the other two stronger cases of magnetism, the velocity and field become more concentrated in x, in agreement with the established literature that a horizontal magnetic field introduces such anisotropy. Including a free-surface in the bottom row, the qualitative behaviour from the analogous snapshots of the PV is confirmed where the flow remains much more concentrated along the x-direction and closer to the jet axis. The oscillations in the anisotropy norms are slower and the KE appears better aligned with the x-axis than the ME for all values of M. Unsurprisingly, these anisotropy norms look different than the turbulent analogues in terms of where they start. In turbulence, we picked the initial KE to be isotropic and here
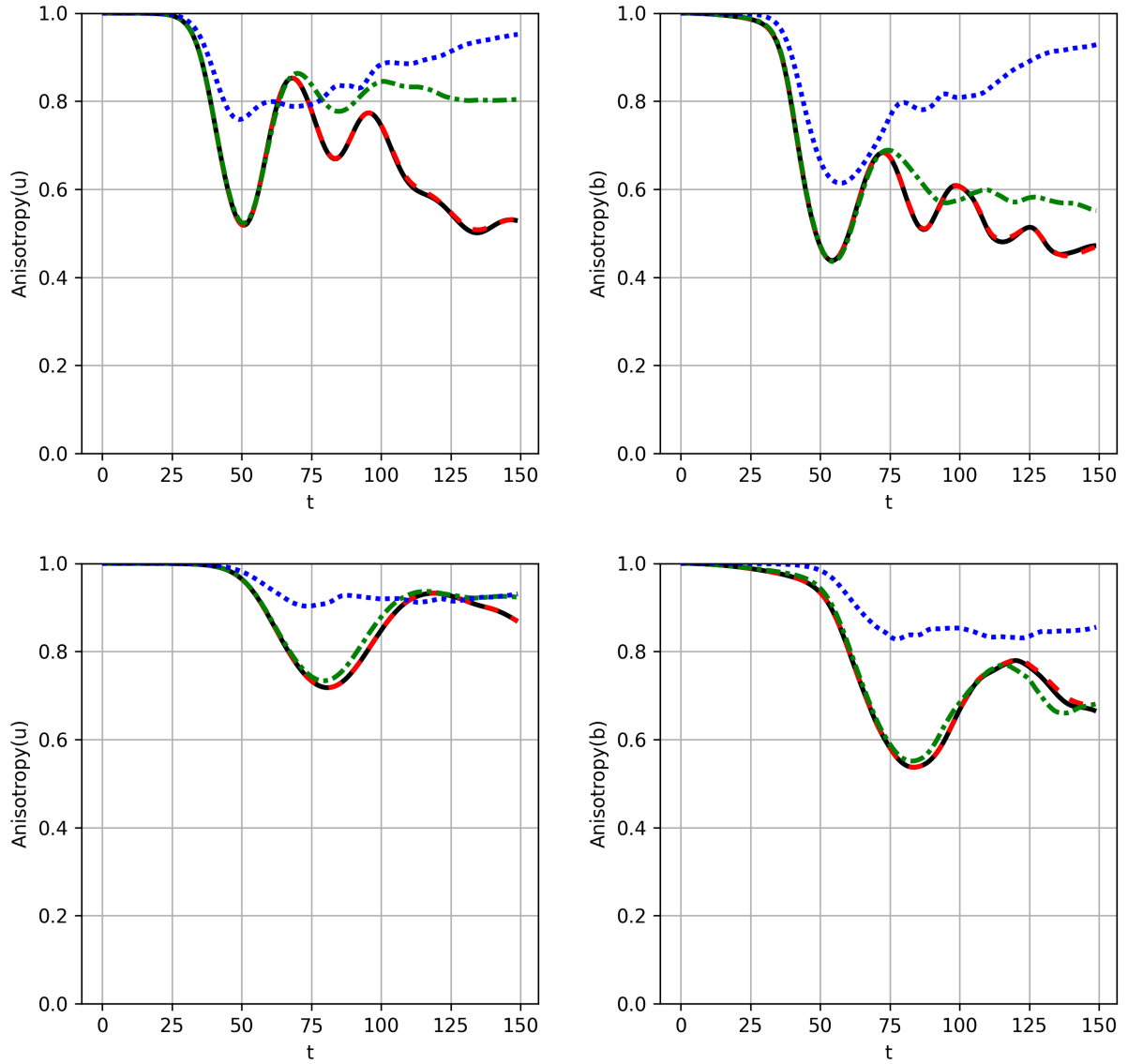
Figure 5.6: Anisotropy norms for the velocity (left) and magnetic field (right) (2.78) for the rigid lid (top) and free-surface (bottom) Bickley jet as a function of time for four different values of M: 0 (solid black), 10^{-3} (dashed red), 10^{-2} (dot-dashed green) and 10^{-1} (dotted blue).

81

it clearly is not. However, the general alignment of the flow with the magnetic field for increasing M remains, especially in a rigid lid configuration. While the turbulence cases showed largely isotropic flows in the presence of a free-surface, we certainly cannot expect that to be the case for the jet, where the flow was initialized in the x-direction.

5.5 Energy Spectra and Spectral Transfers

We consider the energy spectra and energy dissipation from (2.56) and (2.57). We however omit the dynamic components of the spectral fluxes that we saw in the turbulence chapter. The reason is that in the case of a Bickley jet, the background streamfunction $\bar{\Psi}$ is a hyperbolic tangent, which is not periodic across the boundary and does not allow us to cleverly transform the equations for the perturbation KE into the total KE in our calculations of the budgets. The computational consequences of plotting the same fluxes for the perturbation KE shows a $\Pi(k)$ that does not vanish at large k. Since KE is taken from the background jet to feed the perturbations, there is no reason $T(k)$ should be conservative in this regime[1]. However, the dissipative effects of viscosity and diffusion indicate at what length scales energy is lost. This is a decent comparison to make with the turbulence results, which only had a random component to the KE.

First, the spectral slopes are included in Figure 5.7, in the same arrangement considered in our study of turbulence (Figure 4.5). We take the same temporal averaging in $120 < t < 150$ and the slopes are computed again in $6 < k < 10$. We find that the slopes of the perturbation KE are very similar to the turbulence cases in the top-left panel, again where increasing M pushes more KE to smaller scales and generally shallows the spectral slope. This suggest that the perturbations on the jet are turbulent-like. The $M = 10^{-2}$ curve appears as an outlier once again, where the slope is shallower than the strongest case. This is believable since the evolution of the jet in $M = 10^{-1}$ is hardly turbulent and rather displays the advection of vorticity filaments, aligning with the field. For the weak values of M, the ME spectrum (top-right) is still very flat until $M = 10^{-2}$, where the two stronger fields show a peak of ME in the mid-scales.

For the case of a free-surface in the next row, the hydrodynamic case is still somewhat steeper and the qualitative behaviour is similar to the above where more KE is contained at smaller scales for increasing M. For the ME, the free-surface provides spectra that are more convex (as opposed to flat) in the mid-wavenumbers and there is greater scale separation in the very small k for the two strongest values of the field. The various similarities

---

[1] A cosine transform would avoid the computational constraints of general background streamfunctions.
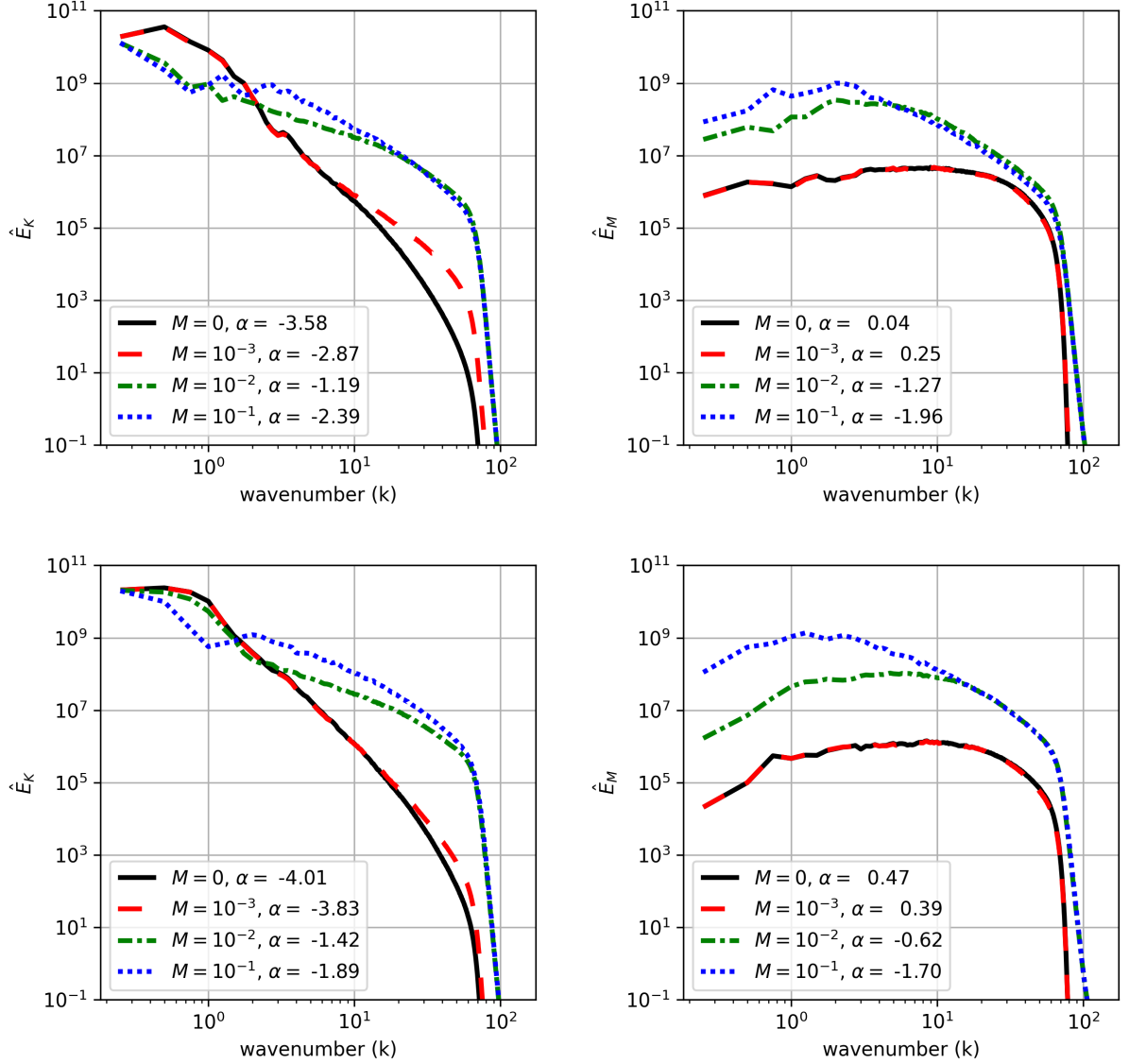
Figure 5.7: KE ($\hat{E}_V$, right) and ME ($\hat{E}_M$, left) spectra for the rigid lid (top) and free-surface (bottom) Bickley jet as a function of the wavenumber for four different values of M: 0 (solid black), 10^{-3} (dashed red), 10^{-2} (dot-dashed green) and 10^{-1} (dotted blue). Spectral slopes α (for $E_{V,M} \sim k^{\alpha}$) are computed in the range $6 < k < 10$ and all quantities are temporally averaged in $120 < t < 150$.

between these slopes and those of the turbulent cases indicate that the long-term evolution of the unstable Bickley jet does give rise to a turbulent-like flow in the perturbations. Of course, the same exception from Chapter 4 occurs, where the strongest case of magnetism induces dynamics that are highly anisotropic, and so the 1D spectra are not the best tool of diagnosis for this particular case.

The viscous and diffusive components D_H, D_M of energy dissipation are plotted in Figure 5.8, temporally averaged in $120 < t < 150$ and shown as a function of k. Recall in Chapter 4 we discussed two particular regimes for these quantities, a hydrodynamic one, where energy was most dissipated at large scales due to viscosity, and then a magnetic regime where energy was mostly lost at smaller length scales. In rigid lid turbulence, the transition between both regimes was made sharply from $M = 10^{-3}$ to $M = 10^{-2}$. Instead, our rigid lid jet evolution (top-left) shows a similar story to that of free-surface turbulence, where the competition of both regimes is seen for $M = 10^{-2}$. The amplitudes of viscous dissipation in either regime for this strength of M differ by about a factor of 3. For the largest case of magnetism however, see still see the hydrodynamic regime peaking near $k = 2$ and it appears to remain dominant over the magnetic one. The dissipation of energy due to diffusion is very similar to the turbulence cases where the wavenumber at which energy is most dissipated moves to larger scales for increasing M. Now, the $M = 10^{-2}$ case shows a larger magnitude of diffusion near $k = 10$ compared to the strongest field but the latter is more uniformly active over the mid-wavenumbers.

For the free-surface evolution in the next row, viscosity in the hydrodynamic case is reduced in amplitude and show two local minima near $k = 0.5 - 0.8$ and $k = 2$. The weak field case is essentially the same supported by the virtually identical evolution shown in the snapshots of the PV. For $M = 10^{-2}$ and $M = 10^{-1}$, we see similar viscous dissipation as in the rigid lid case, where the two regimes in D_H compete and are still dominated by the hydrodynamic regime (in amplitude). The increase of M for diffusion still increases the scale at which energy is dissipated, in agreement with the plots of L_b which indicated that the typical scale of the ME also increased with M.
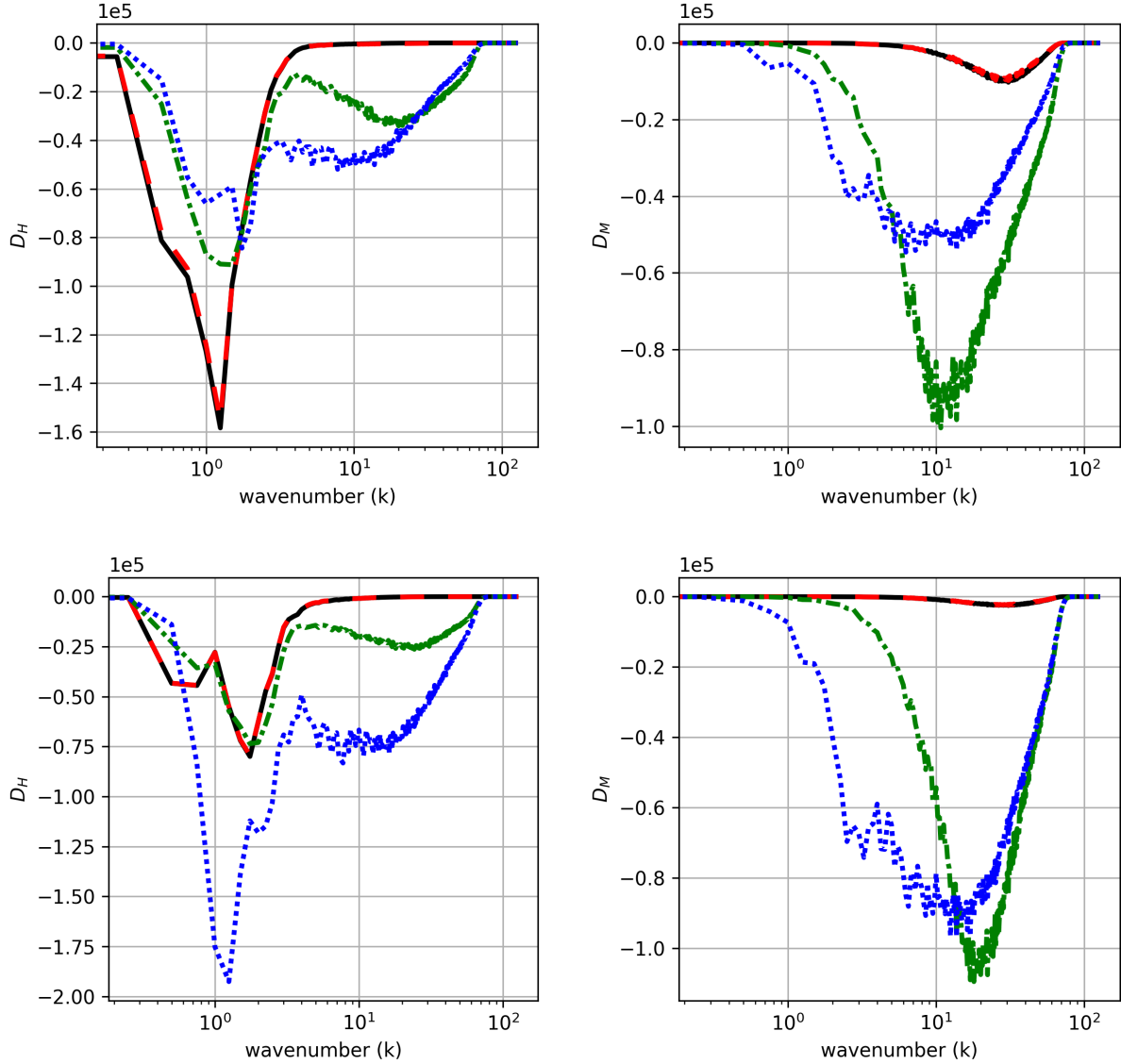
Figure 5.8: Energy dissipation from viscosity (D_H, left), and diffusion (D_M, right) for the rigid lid (top) and free-surface (bottom) unstable Bickley jet as a function of the wavenumber for 4 different values of M: 0 (solid black), 10^{-3} (dashed red), 10^{-2} (dot-dashed green) and 10^{-1} (dotted blue). All quantities are temporally averaged in $120 < t < 150$.

Chapter 6

Conclusion

In this thesis, we covered in detail the nonlinear evolution of jets, vortices and turbulence for finite and discrete ranges of the nondimensional parameters. We derived evolution equations for the conserved quantities of the system, including an adjusted definition for the cross-helicity which accounts for the influence of the free-surface in QG-MHD. Inspired by Weiss' classical vortex problems, we considered various arrangements of vortices in an attempt to better understand their core dynamics with a magnetic field beyond a kinetic context. We saw clear evidence of magnetic flux expulsion for the weaker values of $M = 0, 10^{-3}$ (weaker Lorentz force) and vortex disruption for a sufficiently strong magnetic field, with $M = 10^{-2}$ (stronger Lorentz force). For large enough M, thin filaments of PV were found to amplify on the periphery of the vortices until they dominated the flow. The strongest considered field introduced different dynamics, inducing elastic properties in the fluid and a resulting oscillatory behaviour. The presence of a magnetic field encourages KE to be moved to smaller length scales, and more so with increasing M. After vortices have distorted magnetic field lines, the ME does the opposite and increases in length scale for increasing M. The free-surface in the context of rotating hydrodynamics has a compacting effect on the flow where the interaction between large scale vortices is inhibited. For MHD vortices, the free-surface has the same consequence with a stabilizing effect on their evolution. The surface tended to inhibit the alignment of the flow with the field compared to the rigid lid cases and of course, the magnetic field prevented a flow from remaining at larger length scales. The consequent combination and interaction between the free-surface and the field is complicated and warrants further investigation.

Using our newfound wisdom on vortex-field interactions, we moved to a more global description of freely-decaying turbulence. Various features remained from the study of vortices, where the field introduced anisotropy and generated smaller scale features in

the PV. The typical length scale of the KE decreased for increasing M whereas we saw an increase in that of the ME. The presence of the free-surface with $F = 1$ has again suppressed temporal oscillations in the relevant quantities and inhibited the eventual alignment of the flow with the field. We found in studying the kinetic $(\hat{E}_K)$ and magnetic $(\hat{E}_M)$ energy spectra that the shape of $\hat{E}_K$ tended to shallow with increasing M, while $\hat{E}_M$ tended to steepen and accumulate energy at larger length scales. These behaviours were still present and obvious with a weak free-surface. In our study of decaying turbulence, we developed tools to understand the direction of the energy cascade. The derivation and computation of the spectral energy transfers $T_{q,L,A}(k)$ and respective fluxes $\Pi_{q,L,A}(k)$ provided formalism to understand to what extent the particular terms in the equations were moving energy to smaller or larger length scales. The numerical tools to compute them can be upgraded to do so for any flow, regardless of the shape of both the kinetic and magnetic streamfunctions, using more sophisticated transforms.

In our computation of $T_{q,L,A}(k)$ and $\Pi_{q,L,A}(k)$, we confirmed that the total energy is indeed conserved in the absence of viscosity and diffusion, where $T = T_q + T_L + T_A$ is conservative. We further found numerical evidence to suggest that T_q (PV advection) alone is conservative since Π_q vanishes at large wavenumbers for all considered values of M. While the Lorentz force showed a net downscale transfer of energy on the system, the advection of the magnetic potential compensated to make $T_L + T_A$ appear conservative as well. The inclusion of a free-surface amplified the magnitude of $\Pi = \Pi_q + \Pi_L + \Pi_A$ for larger M and introduced a region of downscale transfer near larger scales. This hydrodynamic downscale transfer was manifested in the flux component due to the advection of the PV, Π_q for the hydrodynamic and weak field $(M = 10^{-3})$ cases. Energy dissipation due to viscosity D_H showed a competition of two regimes in the spectral budget. Energy is found to be lost to viscous effects in two distinct ranges of k, at large (hydrodynamic, $k < 1$) and small (magnetic, $k \approx 10$) length scales, separated by approximately a decade. The diffusion of ME is localized at small scales ($k \approx 30$) for small M, and moves to larger length scales for increasing M, converging on the same range with $k \approx 10$. This same convergence was observed in the typical scales of the motion, L_u, L_b.

For the unstable MHD Bickley jet, we computed the linear stability of the system to confirm that F and M were both individually stabilizing to the jet, providing smaller growth rates. We further found that their combined effects are also stabilizing on the jet in the linear regime. Increasing F tended to push the largest growing mode to smaller length scales in the x-direction, while increasing M did exactly the opposite. In the nonlinear simulations, we showed how the system evolves past the linear regime, where the most unstable mode grows exponentially in time. The instability generated vortices that are disrupted for large enough M, creating small scale features and a resulting turbulent-

like flow. The expected spatial compactness introduced by the weak free-surface was still present and the created vortices remained closer to the jet axis compared to the rigid-lid evolution. The typical scales of motion showed a similar behaviour to the turbulence cases, with a decrease in L_u and increase in L_b for increasing M. The inclusion of the free-surface again suppressed temporal variations in the diagnostics. The spectral slopes are similar to the turbulence cases considered and still display the consistent behaviour of KE moving to smaller scales and ME moving to larger scales. The viscous D_H and diffusive D_M terms of the spectral budget also display a similar competition of the hydrodynamic and magnetic regimes, though both regimes are significant for $M = 10^{-2}, 10^{-1}$ in the jet, whereas the turbulence cases for the same M shifted entirely to a magnetic regime.

In this endeavour, we thus answered how the evolution of a shallow conducting fluid differs, for increasingly strong magnetic fields, in the cases of a rigid lid and a free-surface configuration. Then, we found how the stability of a MHD Bickley jet is affected by an increasingly strong field with and without a free-surface. In doing so, we described the transition from a hydrodynamic flow to one dominated by magnetic effects in a simple model of the solar tachocline and the Earth's molten core. We found that the magnetic field generates smaller scale features in the PV. Flux expulsion was observed for weaker fields and vortex disruption was evident for stronger ones. The weak free-surface makes the flow more compact and inhibits the anisotropy induced by the field. KE is sent to smaller length scales while ME moves to larger scales for increasing field strength. In the mid to small scales, the downscale transfer of energy is due to the Lorentz force, and the free-surface adds an additional downscale transfer at larger scales. Finally, the field and free-surface are confirmed to be individually stabilizing to the MHD Bickley jet and the combined effects are also stabilizing. Using the tools that we developed, one can readily extend this research to forced QG-MHD turbulence, other parallel shear flows, and extended ranges of the effective magnetic field strength M and the rotational Froude number F. Further, one could investigate the effects of a not so small free-surface in shallow MHD without invoking the QG approximation.

References

[1] ALFVÉN, H. Existence of electromagnetic-hydrodynamic waves. *Nature 150*, 3805 (1942), 405–406.

[2] ALFVÉN, H. A new type of wave motion and its importance in solar physics. *Acta Radiologica os-27*, 3-4 (1946), 228–242.

[3] AURNOU, J., AND KING, E. The cross-over to magnetostrophic convection in planetary dynamo systems. *Proceedings of the Royal Society A: Mathematical, Physical and Engineering Sciences 473*, 2199 (2017), 20160731.

[4] BALK, A. M. Large-scale quasi-geostrophic magnetohydrodynamics. *The Astrophysical Journal 796*, 2 (2014), 143.

[5] BATCHELOR, G. K. Computation of the energy spectrum in homogeneous two-dimensional turbulence. *The Physics of Fluids 12*, 12 (1969), II–233–II–239.

[6] BICKLEY, W. LXXIII. The plane jet. *The London, Edinburgh, and Dublin Philosophical Magazine and Journal of Science 23*, 156 (1937), 727–731.

[7] BISKAMP, D., AND MÜLLER, W.-C. Scaling properties of three-dimensional isotropic magnetohydrodynamic turbulence. *Physics of Plasmas 7*, 12 (2000), 4889–4900.

[8] BISKAMP, D., SCHWARZ, E., AND ZEILER, A. Instability of a magnetized plasma jet. *Physics of Plasmas 5*, 7 (1998), 2485–2488.

[9] BISKAMP, D., AND WELTER, H. Dynamics of decaying two-dimensional magnetohydrodynamic turbulence. *Physics of Fluids B: Plasma Physics 1*, 10 (1989), 1964–1979.

[10] Braginsky, S. I. Magnetic Rossby waves in the stratified ocean of the core, and topographic core-mantle coupling. *Earth, Planets and Space 50* (Aug. 1998), 641–649.

[11] Braginsky, S. I. Formation of the stratified ocean of the core. *Earth and Planetary Science Letters 243*, 3-4 (2006), 650–656.

[12] Calkins, M. A., Julien, K., Tobias, S. M., and Aurnou, J. M. A multiscale dynamo model driven by quasi-geostrophic convection. *Journal of Fluid Mechanics 780* (2015), 143–166.

[13] Canet, E., Finlay, C. C., and Fournier, A. Hydromagnetic quasi-geostrophic modes in rapidly rotating planetary cores. *Physics of the Earth and Planetary Interiors 229* (2014), 1–15.

[14] Cattaneo, F., and Vainshtein, S. I. Suppression of turbulent transport by a weak magnetic field. *Astrophysical Journal 376* (July 1991), L21.

[15] Chandrasekhar, S. Hydrodynamic and hydromagnetic stability. *International Series of Monographs on Physics* (1961).

[16] Charbonneau, P., Christensen-Dalsgaard, J., Henning, R., Larsen, R. M., Schou, J., Thompson, M. J., and Tomczyk, S. Helioseismic constraints on the structure of the solar tachocline. *Astrophysical Journal 527*, 1 (1999), 445–460.

[17] Charney, J. G. Geostrophic turbulence. *Journal of the Atmospheric Sciences 28*, 6 (1971), 1087–1095.

[18] Council, N. R. *The Effects of Solar Variability on Earth's Climate: A Workshop Report*. The National Academies Press, Washington, DC, 2012.

[19] Cowling, T. G. The magnetic field of sunspots. *Monthly Notices of the Royal Astronomical Society 94* (Nov. 1933), 39–48.

[20] De Sterck, H. Hyperbolic theory of the "shallow water" magnetohydrodynamics equations. *Physics of Plasmas 8*, 7 (2001), 3293–3304.

[21] Dellar, P. J. Hamiltonian and symmetric hyperbolic structures of shallow water magnetohydrodynamics. *Physics of Plasmas 9*, 4 (2002), 1130–1136.

[22] DIAMOND, P. H., ITOH, S., ITOH, K., AND HAHM, T. Zonal flows in plasma—a review. *Plasma Physics and Controlled Fusion 47*, 5 (2005), R35.

[23] DIAMOND, P. H., ITOH, S.-I., ITOH, K., AND SILVERS, L. J. β-plane MHD turbulence and dissipation in the solar tachocline. *The solar tachocline* (2007), 211–239.

[24] DRAZIN, P. G., AND REID, W. H. *Hydrodynamic stability*. Cambridge university press, 1981.

[25] DRITSCHEL, D. G., DIAMOND, P., AND TOBIAS, S. Circulation conservation and vortex breakup in magnetohydrodynamics at low magnetic Prandtl number. *Journal of Fluid Mechanics 857* (2018), 38–60.

[26] DRITSCHEL, D. G., AND TOBIAS, S. M. Two-dimensional magnetohydrodynamic turbulence in the small magnetic Prandtl number limit. *Journal of Fluid Mechanics 703* (2012), 85–98.

[27] ELSASSER, W. M. Induction effects in terrestrial magnetism Part I. Theory. *Physical Review 69*, 3-4 (1946), 106.

[28] ELSASSER, W. M. The earth's interior and geomagnetism. *Rev. Mod. Phys. 22* (Jan 1950), 1–35.

[29] ELSASSER, W. M. The hydromagnetic equations. *Phys. Rev. 79* (Jul 1950), 183–183.

[30] FLIERL, G. R., MALANOTTE-RIZZOLI, P., AND ZABUSKY, N. J. Nonlinear waves and coherent vortex structures in barotropic beta-plane jets. *Journal of Physical Oceanography 17*, 9 (1987), 1408 – 1438.

[31] FRASER, A. E., CRESSWELL, I. G., AND GARAUD, P. Resistive instabilities in sinusoidal shear flows with a streamwise magnetic field. *arXiv preprint arXiv:2204.10875* (2022).

[32] FRIGO, M., AND JOHNSON, S. G. The design and implementation of FFTW3. *Proceedings of the IEEE 93*, 2 (2005), 216–231. Special issue on "Program Generation, Optimization, and Platform Adaptation".

[33] FYFE, D., AND MONTGOMERY, D. High-beta turbulence in two-dimensional magnetohydrodynamics. *Journal of Plasma Physics 16*, 2 (1976), 181–191.

[34] GILMAN, P., AND DIKPATI, M. Baroclinic instability in the solar tachocline. *The Astrophysical Journal 787*, 1 (2014), 60.

[35] GILMAN, P. A. Magnetohydrodynamic shallow water equations for the solar tachocline. *The Astrophysical Journal 544*, 1 (nov 2000), L79–L82.

[36] GODON, P., AND SHAVIV, G. A two-dimensional time dependent Chebyshev method of collocation for the study of astrophysical flows. *Computer Methods in Applied Mechanics and Engineering 110*, 1 (1993), 171–194.

[37] GOUGH, D., HUGHES, D., ROSNER, R., AND WEISS, N. An introduction to the solar tachocline. *The solar tachocline* (2007), 3–30.

[38] GRUZINOV, A. V., AND DIAMOND, P. H. Self-consistent theory of mean-field electrodynamics. *Phys. Rev. Lett. 72* (Mar 1994), 1651–1653.

[39] GUERVILLY, C., HUGHES, D. W., AND JONES, C. A. Generation of magnetic fields by large-scale vortices in rotating convection. *Phys. Rev. E 91* (Apr 2015), 041001.

[40] HOWARD, L. N. Note on a paper of John W. Miles. *Journal of Fluid Mechanics 10*, 4 (1961), 509–512.

[41] HUGHES, D., AND TOBIAS, S. On the instability of magnetohydrodynamic shear flows. *Proceedings of The Royal Society A: Mathematical, Physical and Engineering Sciences 457* (06 2001), 1365–1384.

[42] HUGHES, D. W., ROSNER, R., AND WEISS, N. *The Solar Tachocline.* Cambridge University Press, 2007.

[43] HUNT, J. C. R. On the stability of parallel flows with parallel magnetic fields. *Proceedings of the Royal Society of London. Series A. Mathematical and Physical Sciences 293*, 1434 (1966), 342–358.

[44] IROSHNIKOV, P. S. Turbulence of a conducting fluid in a strong magnetic field. *Astron. Zh. 40* (Jan. 1963), 742.

[45] KAPPENMAN, J. G. Geomagnetic storms and their impact on power systems. *IEEE Power Engineering Review 16*, 5 (5 1996).

[46] KEATING, S. R., SILVERS, L. J., AND DIAMOND, P. H. On cross-phase and the quenching of the turbulent diffusion of magnetic fields in two dimensions. *The Astrophysical Journal 678*, 2 (apr 2008), L137–L140.

[47] KONDIĆ, T., HUGHES, D. W., AND TOBIAS, S. M. The decay of a weak large-scale magnetic field in two-dimensional turbulence. *The Astrophysical Journal 823*, 2 (2016), 111.

[48] KRAICHNAN, R. H. Inertial-range spectrum of hydromagnetic turbulence. *Phys. Fluids 8* (1965), 1385.

[49] KRAICHNAN, R. H. Inertial ranges in two-dimensional turbulence. *Physics of Fluids 10*, 7 (July 1967), 1417–1423.

[50] KUKHARKIN, N., ORSZAG, S. A., AND YAKHOT, V. Quasicrystallization of vortices in drift-wave turbulence. *Phys. Rev. Lett. 75* (Sep 1995), 2486–2489.

[51] KULSRUD, R. M., AND ANDERSON, S. W. The spectrum of random magnetic fields in the mean field dynamo theory of the galactic magnetic field. *Astrophysical Journal 396* (Sept. 1992), 606.

[52] LARICHEV, V. D., AND MCWILLIAMS, J. C. Weakly decaying turbulence in an equivalent-barotropic fluid. *Physics of Fluids A: Fluid Dynamics 3*, 5 (1991), 938–950.

[53] LARMOR, S. How could a rotating body such as the sun become a rotating magnet? *Rep. Britt. Assoc. Adv. Sci* (1919).

[54] LECOANET, D., ZWEIBEL, E. G., TOWNSEND, R. H., AND HUANG, Y.-M. Violation of Richardson's criterion via introduction of a magnetic field. *The Astrophysical Journal 712*, 2 (2010), 1116.

[55] MAGILL, M., COUTINO, A., STORER, B. A., STASTNA, M., AND POULIN, F. J. Dynamics of nonlinear alfvén waves in the shallow water magnetohydrodynamic equations. *Phys. Rev. Fluids 4* (May 2019), 053701.

[56] MAK, J., GRIFFITHS, S. D., AND HUGHES, D. W. Shear flow instabilities in shallow-water magnetohydrodynamics. *Journal of Fluid Mechanics 788* (Feb 2016), 767–796.

[57] MAK, J., GRIFFITHS, S. D., AND HUGHES, D. W. Vortex disruption by magnetohydrodynamic feedback. *Physical Review Fluids 2*, 11 (2017), 113701.

[58] Matthaeus, W., Pouquet, A., Mininni, P. D., Dmitruk, P., and Breech, B. Rapid alignment of velocity and magnetic field in magnetohydrodynamic turbulence. *Physical review letters 100*, 8 (2008), 085003.

[59] Matthaeus, W., Stribling, W., Martinez, D., Oughton, S., and Montgomery, D. Decaying, two-dimensional, Navier-Stokes turbulence at very long times. *Physica D: Nonlinear Phenomena 51*, 1-3 (1991), 531–538.

[60] Matthaeus, W. H., Ghosh, S., Oughton, S., and Roberts, D. A. Anisotropic three-dimensional MHD turbulence. *Journal of Geophysical Research: Space Physics 101*, A4 (1996), 7619–7629.

[61] McWilliams, J. C. *Fundamentals of geophysical fluid dynamics*. Cambridge University Press, 2006.

[62] Miles, J. W. On the stability of heterogeneous shear flows. *Journal of Fluid Mechanics 10*, 4 (1961), 496–508.

[63] Moffatt, H., and Kamkar, H. The time-scale associated with flux expulsion. *Stellar and Planetary Magnetism* (1983), 91.

[64] Mortensen, M. Shenfun - automating the spectral Galerkin method. In *MekIT'17 - Ninth national conference on Computational Mechanics* (2017), B. H. Skallerud and H. I. Andersson, Eds., International Center for Numerical Methods in Engineering (CIMNE), pp. 273–298.

[65] Mortensen, M. Shenfun: High performance spectral Galerkin computing platform. *Journal of Open Source Software 3*, 31 (2018), 1071.

[66] Müller, W.-C., and Biskamp, D. Scaling properties of three-dimensional magnetohydrodynamic turbulence. *Physical Review Letters 84*, 3 (2000), 475.

[67] Orszag, S. A. On the elimination of aliasing in finite-difference schemes by filtering high-wavenumber components. *Journal of Atmospheric Sciences 28*, 6 (Sept. 1971), 1074–1074.

[68] Orszag, S. A., and Tang, C.-M. Small-scale structure of two-dimensional magnetohydrodynamic turbulence. *Journal of Fluid Mechanics 90*, 1 (1979), 129–143.

[69] Oughton, S., Priest, E. R., and Matthaeus, W. H. The influence of a mean magnetic field on three-dimensional magnetohydrodynamic turbulence. *Journal of Fluid Mechanics 280* (1994), 95–117.

[70] PARKER, E. N. Hydromagnetic dynamo models. *The Astrophysical Journal 122* (1955), 293.

[71] PEDLOSKY, J., ET AL. *Geophysical fluid dynamics*, vol. 710. Springer, 1987.

[72] POLVANI, L. M., ZABUSKY, N., AND FLIERL, G. Two-layer geostrophic vortex dynamics. Part 1. Upper-layer V-states and merger. *Journal of Fluid Mechanics 205* (1989), 215–242.

[73] POULIN, F. J., AND FLIERL, G. R. The nonlinear evolution of barotropically unstable jets. *Journal of physical oceanography 33*, 10 (2003), 2173–2192.

[74] POUQUET, A. On two-dimensional magnetohydrodynamic turbulence. *Journal of Fluid Mechanics 88*, 1 (1978), 1–16.

[75] PROVENZALE, A. Transport by coherent barotropic vortices. *Annual review of fluid mechanics 31*, 1 (1999), 55–93.

[76] RAYLEIGH, L. On the stability, or instability, of certain fluid motions. *Proceedings of the London Mathematical Society 1*, 1 (1879), 57–72.

[77] RHINES, P. B. Waves and turbulence on a beta-plane. *Journal of Fluid Mechanics 69*, 3 (1975), 417–443.

[78] RHINES, P. B. Geostrophic turbulence. *Annual Review of Fluid Mechanics 11*, 1 (1979), 401–441.

[79] SALMON, R. Two-layer quasi-geostrophic turbulence in a simple special case. *Geophysical & Astrophysical Fluid Dynamics 10*, 1 (1978), 25–52.

[80] SALMON, R. Baroclinic instability and geostrophic turbulence. *Geophysical & Astrophysical Fluid Dynamics 15*, 1 (1980), 167–211.

[81] SCHECTER, D. A., BOYD, J. F., AND GILMAN, P. A. "Shallow-water" magneto-hydrodynamic waves in the solar tachocline. *The Astrophysical Journal 551*, 2 (Apr. 2001), L185–L188.

[82] SCHWAIGER, T., GASTINE, T., AND AUBERT, J. Force balance in numerical geodynamo simulations: a systematic study. *Geophysical Journal International 219* (04 2019), S101–S114.

[83] SHEBALIN, J. V., MATTHAEUS, W. H., AND MONTGOMERY, D. Anisotropy in MHD turbulence due to a mean magnetic field. *Journal of Plasma Physics 29*, 3 (1983), 525–547.

[84] SQUIRE, H. B. On the stability for three-dimensional disturbances of viscous fluid flow between parallel walls. *Proceedings of the Royal Society of London. Series A, Containing Papers of a Mathematical and Physical Character 142*, 847 (1933), 621–628.

[85] STRAUSS, H. R. Nonlinear, three-dimensional magnetohydrodynamics of noncircular tokamaks. *The Physics of Fluids 19*, 1 (1976), 134–140.

[86] SUBICH, C. Simulation of the Navier-Stokes equations in three dimensions with a spectral collocation method. *UWSpace* (2011).

[87] SWATERS, G. E. *Introduction to Hamiltonian Fluid Dynamics and Stability Theory*, vol. 102. CRC Press, 1999.

[88] TATSUNO, T., AND DORLAND, W. Magneto-flow instability in symmetric field profiles. *Physics of plasmas 13*, 9 (2006), 092107.

[89] TESSIER, J., CASTRO-FOLKER, N., POULIN, F., AND STASTNA, M. Anisotropy in Faraday instabilities of a shallow conducting fluid. *EPL (Europhysics Letters) 135*, 3 (2021), 34001.

[90] TESSIER, J., AND POULIN, F. Quasi-Geostrophic Magnetohydrodynamics - (Python code, powered by Shenfun). https://github.com/jonathan-tessier/qgmhd, 2022.

[91] TOBIAS, S. M., AND CATTANEO, F. Dynamo action in complex flows: the quick and the fast. *Journal of Fluid Mechanics 601* (2008), 101–122.

[92] TOBIAS, S. M., DIAMOND, P. H., AND HUGHES, D. W. β-plane magnetohydrodynamic turbulence in the solar tachocline. *The Astrophysical Journal Letters 667*, 1 (2007), L113.

[93] TREFETHEN, L. N. *Spectral Methods in MATLAB*. SIAM, 2000.

[94] VAINSHTEIN, S. I., AND ROSNER, R. On turbulent diffusion of magnetic fields and the loss of magnetic flux from stars. *Astrophysical Journal 376* (July 1991), 199.

[95] VALLIS, G. K. *Atmospheric and Oceanic Fluid Dynamics: Fundamentals and Large-Scale Circulation*, 2 ed. Cambridge University Press, 2017.

[96] Virtanen, P., Gommers, R., Oliphant, T. E., Haberland, M., Reddy, T., Cournapeau, D., Burovski, E., Peterson, P., Weckesser, W., Bright, J., van der Walt, S. J., Brett, M., Wilson, J., Millman, K. J., Mayorov, N., Nelson, A. R. J., Jones, E., Kern, R., Larson, E., Carey, C. J., Polat, İ., Feng, Y., Moore, E. W., VanderPlas, J., Laxalde, D., Perktold, J., Cimrman, R., Henriksen, I., Quintero, E. A., Harris, C. R., Archibald, A. M., Ribeiro, A. H., Pedregosa, F., van Mulbregt, P., and SciPy 1.0 Contributors. SciPy 1.0: Fundamental algorithms for scientific computing in python. *Nature Methods 17* (2020), 261–272.

[97] Waite, M. L. Turbulence and stability, Course notes for AMATH 863, Department of Applied Mathematics, University of Waterloo, April 2021.

[98] Waugh, D. W. The efficiency of symmetric vortex merger. *Physics of Fluids A: Fluid Dynamics 4*, 8 (1992), 1745–1758.

[99] Weiss, N. O. The expulsion of magnetic flux by eddies. *Proceedings of the Royal Society of London. Series A. Mathematical and Physical Sciences 293*, 1434 (1966), 310–328.

[100] Yadav, R. K., Gastine, T., Christensen, U. R., Wolk, S. J., and Poppenhaeger, K. Approaching a realistic force balance in geodynamo simulations. *Proceedings of the National Academy of Sciences 113*, 43 (2016), 12065–12070.

[101] Yokoi, N. Cross helicity and related dynamo. *Geophysical & Astrophysical Fluid Dynamics 107*, 1-2 (2013), 114–184.

[102] Zeitlin, V. On the structure of phase-space, Hamiltonian variables and statistical approach to the description of two-dimensional hydrodynamics and magnetohydrodynamics. *Journal of Physics A: Mathematical and General 25*, 4 (1992), L171.

[103] Zeitlin, V. Remarks on rotating shallow-water magnetohydrodynamics. *Nonlinear Processes in Geophysics 20*, 5 (2013), 893–898.

[104] Zeitlin, V., and Kambe, T. Two-dimensional ideal magnetohydrodynamics and differential geometry. *Journal of Physics A: Mathematical and General 26*, 19 (1993), 5025.